APPENDIX E

DEVELOPMENT OF FLAW EVALUATION CRITERIA FOR CLASS 2, 3, AND BALANCE OF PLANT PIPING

The existing flaw evaluation criteria embodied in Section XI of the ASME Boiler and Pressure Vessel Code are for Class 1 high energy piping systems. Currently, no such criteria exist for Class 2, 3, and Balance of Plant (BOP) piping, even though some of these systems are being inspected more frequently due to increased inspection requirements in the ASME Code. It is also important to note that some of these Class 2 and Class 3 piping systems are more important relative to plant risk from a core damage perspective than some Class 1 piping systems. As such, criteria to evaluate flaws found during these inspections are needed.

The main technical differences between Class 1 piping and Class 2, 3, and BOP piping are that (1) the Class 2, 3, and BOP piping may operate at lower operating pressures, and thus may be fabricated from thinner pipe with higher R/t ratios, and (2) they may also operate at lower temperatures than Class 1 piping.

E.1 Effect of Pipe R/t Ratio on Pipe Fracture

As mentioned above, Class 2, 3, and BOP piping systems typically operate at lower pressures and thus are fabricated from thinner pipe, i.e., pipe with higher R/t ratios. The higher R/t ratios can influence the pipe fracture behavior under LEFM, EPFM, and limit-load conditions. As part of this effort, the effect of R/t ratio on all three potential failure modes was to be investigated.

E.1.1 Effect of Pipe R/t Ratio on the Elastic F-Functions (LEFM)

The crack driving force under linear-elastic fracture mechanics (LEFM) conditions is typically expressed in terms of the stress intensity factor K. The expression for K is:

$$K = F\sigma\sqrt{\pi a} \qquad \text{(E.1)}$$

where,

K = stress intensity factor,

F = Elastic F-function,

F = remote applied stress, and

a = crack size.

Currently, for Class 1 piping, Section XI limits the applicability of the F-functions they report to pipes with R/t ratios of less than 15. While this limitation is acceptable for Class 1 piping, it is too restrictive for Class 2, 3, and BOP piping which typically are fabricated from pipes with much larger R/t ratios. In order to address this limitation, researchers working for The Materials Property Council (MPC) in this country (Ref. E.1) and researchers at CEA in France (Ref. E.2) have developed an extensive database of numerical solutions for F using the finite element method for a variety of pipe and flaw geometries (flaw depth (a/t) and flaw length [c/a or **2**/**B**]), pipe R/t ratios, and crack location and loading conditions (i.e., internal flaw loaded in tension, internal flaw loaded in bending, external flaw loaded in tension, and external flaw loaded in bending). The flaws in each case were oriented in the circumferential direction. As part of this effort in the BINP program, these tabulated numerical results were curve fit to a series of mathematical expressions, with the goal of including these mathematical expressions into a code type document.

For the case of an internal surface crack loaded in tension, the equation for F (FT) at the deepest point along the crack was found to be:

$$F\left(\frac{R}{t},\frac{a}{t},\frac{\theta}{\pi}\right)=\left[S_3\left(\frac{a}{t}\right)^3+S_2\left(\frac{a}{t}\right)^2+S_1\left(\frac{a}{t}\right)\ln\frac{R}{t}+S_2\right]\left[\ln\frac{R}{t}+\ln\frac{\theta}{\pi}-\ln\frac{a}{t}+\ln\pi\right]+S_4 \qquad \text{(E.2)}$$

For the case of an internal surface crack loaded in bending, the F function (FB) at the deepest point along the crack was:

$$F\left(\frac{R}{t},\frac{a}{t},\frac{\theta}{\pi}\right)=S_1\ln\frac{R}{t}+\left[\left(S_3\left(\frac{a}{t}\right)^3+S_1\left(\frac{a}{t}\right)+S_2\left(\frac{a}{t}\right)^2\right)\ln\frac{R}{t}+S_2\right]\left[\ln\frac{R}{t}+\ln\frac{\theta}{\pi}-\ln\frac{a}{t}+\ln\pi\right]+S_4 \qquad \text{(E.3)}$$

For the case of an external surface crack loaded in tension, the F function (FT) at the deepest point along the crack was:

$$F\left(\frac{R}{t},\frac{a}{t},\frac{\theta}{\pi}\right)=\left[S_3\left(\frac{a}{t}\right)^2+\left(S_1\ln\frac{R}{t}+S_2\right)\left(\frac{a}{t}\right)+S_2\right]\left[\ln\frac{R}{t}+\ln\frac{\theta}{\pi}-\ln\frac{a}{t}+\ln\pi\right]+S_4 \qquad \text{(E.4)}$$

Finally, for the case of an external surface crack loaded in bending, the F function (FB) at the deepest point along the crack is:

$$F\left(\frac{R}{t},\frac{a}{t},\frac{\theta}{\pi}\right)=\left[S_3\left(\frac{a}{t}\right)^3+S_2\left(\frac{a}{t}\right)^2+S_1\left(\frac{a}{t}\right)\ln\frac{R}{t}+S_2\right]\left(\ln\frac{R}{t}+\ln\frac{\theta}{\pi}-\ln\frac{a}{t}+\ln\pi\right)+S_4 \qquad \text{(E.5)}$$

The above expressions are valid for:

$$5\le\frac{R}{t}\le 100,$$

$$0<\frac{a}{t}\le 0.8,$$

$$0\le\frac{c}{a}\le 16$$

where, the crack length expression (c/a) can be expressed in terms of (**2**/**B**) using the relationship:

$$\left(\frac{\theta}{\pi}\right)=\left(\pi\frac{R}{t}\right)^{-1}\left(\frac{a}{t}\right)\left(\frac{c}{a}\right) \qquad \text{(E.6)}$$

As part of this effort, the curve fitting coefficients S1, S2, S3, and S4 were developed for each flaw location and each loading condition. Coefficients were developed for a best-fit through the data as well as developing a set of coefficients that would result in a 15 percent conservative assessment with respect to the tabular data from the finite element analyses. Table E.1 provides both the best-fit and 15 percent conservative values for these curve fitting coefficients.

Figures E.1 through E.3 illustrate how the best fit curve fitting equations compare with the numerical results developed at CEA (Ref. E.2). Each of these figures is for the case of an internal circumferential surface crack loaded in bending. Figure E.1 compares the best-fit curve fit F-function expression with the CEA tabulated data as a function of the R/t ratio for various crack lengths (c/a values) for a constant flaw depth of a/t = 0.4. Figure E.2 compares the best-fit expressions with the tabulated data as a function of crack length (c/a) for various R/t ratios for a constant flaw depth of a/t = 0.4. Figure E.3 compares the best-fit expressions with the tabulated data as a function of crack depth (a/t) for various crack lengths (c/a values) for a constant R/t value of 20. In each case, one can see that the agreement between the best-fit expressions and the tabulated data from the finite element

Table E.1 Best-fit curve fitting coefficients and 15 percent conservative curve fitting coefficients for various crack locations and loading conditions

	Best-fit coefficients	15 percent conservative coefficients
Internal Flaw Loaded in Tension (F^T)		
S_1	0.0919	0.1057
S_2	0.1517	0.1744
S_3	0.4057	0.4665
S_4	0.7066	0.8125
Internal Flaw Loaded in Bending (F^B)		
S_1	0.0328	0.0377
S_2	0.1645	0.1891
S_3	0.0292	0.0336
S_4	0.5529	0.6358
External Flaw Loaded in Tension (F^T)		
S_1	0.0286	0.0329
S_2	0.1529	0.1759
S_3	0.8527	0.9806
S_4	0.6847	0.7874
External Flaw Loaded in Bending (F^B)		
S_1	0.0864	0.0993
S_2	0.1781	0.2048
S_3	0.6988	0.8036
S_4	0.6670	0.7670

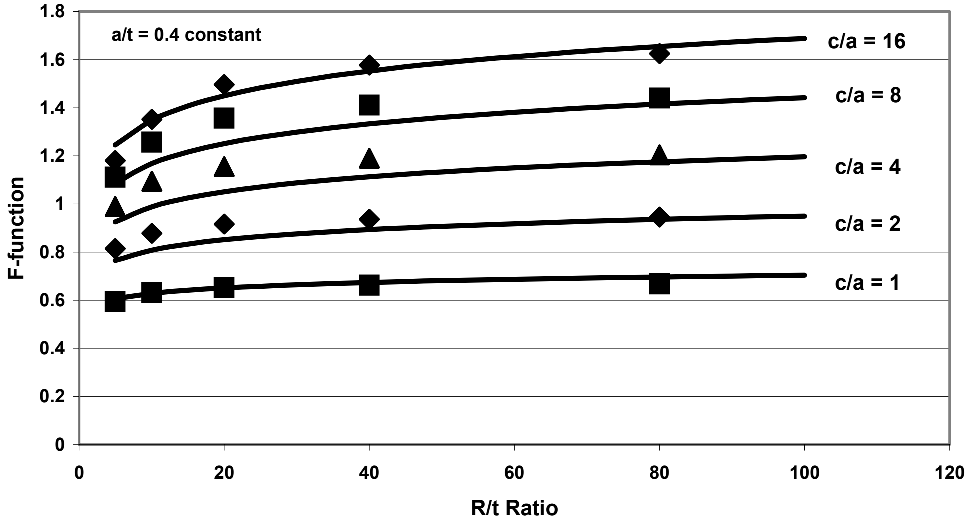

Figure E.1 Comparison of best-fit curve-fit expressions for F with numerical results from finite element analyses as a function of R/t ratio for various crack lengths for a constant crack depth of a/t = 0.4

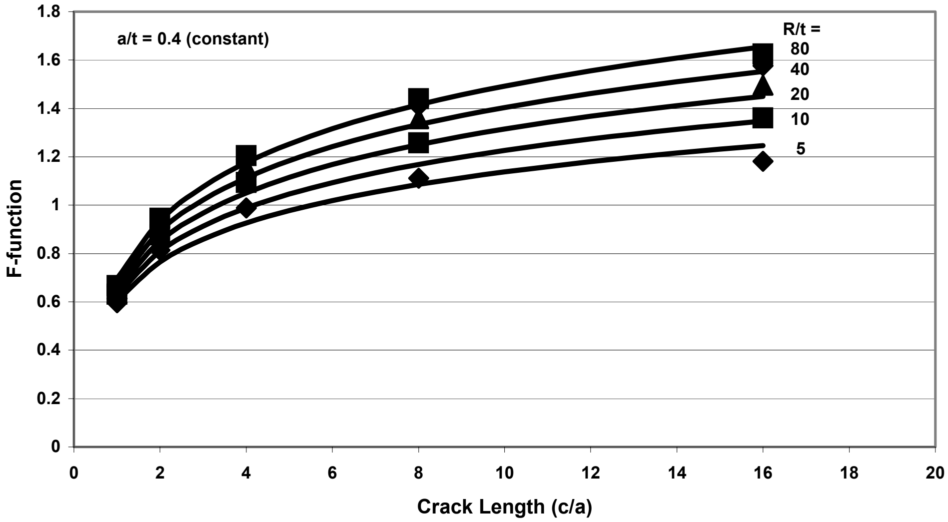

Figure E.2 Comparison of best-fit curve-fit expressions for F with numerical results from finite element analyses as a function of crack length for various R/t ratios for a constant crack depth of a/t = 0.4

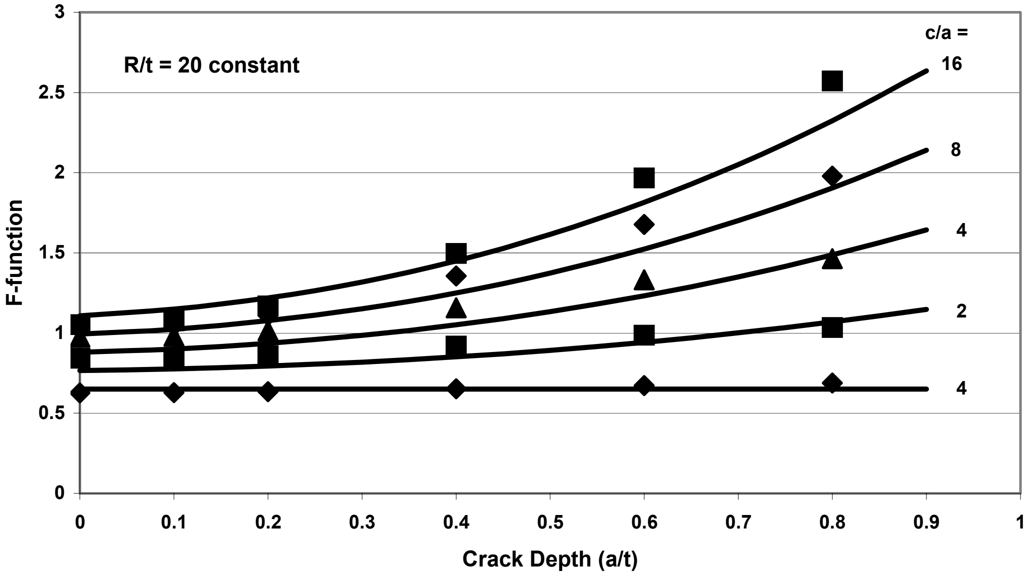

Figure E.3 Comparison of best-fit curve-fit expressions for F with numerical results from finite element analyses as a function of crack depth for various crack lengths for a constant R/t ratio of 20 analyses is quite good. Similar agreement was seen for the other flaw location and loading condition combinations, e.g., external flaws subjected to tension loading.

Of note from Figures E.1 through E.3 is the fact that the F-functions do not appear to be that sensitive to R/t ratio, especially once the R/t ratio gets larger than about 20. For the same size flaw, one can see from Figure E.1 that the difference in F between the value of R/t = 20 and R/t = 100 is at most 15 to 20 percent.

One limitation associated with this analysis, is that both the MPC data (Ref. E.1) and the CEA data (Ref. E.2) are limited in that they do not consider the case of very long cracks. The limit on c/a values for the MPC data set is 32 and the limit on c/a values for the CEA data set is 16. If one considers a crack in a pipe with an R/t ratio of 40 that is one-fourth of the pipe circumference in length and one-half of the pipe wall thickness in depth, it can be seen through simple mathematical manipulation that the c/a value is 20**B**, which is about twice the limit of the MPC data set and four times the limit of the CEA data set. The good news however, is that the F-function values are starting to level off to a near constant value for these longer crack lengths, see Figure E.2. Consequently, it may be possible to simply extrapolate the value for the F-functions at these higher c/a values.

The results of these efforts have been presented to the ASME Section XI Pipe Flaw Evaluation Working Group for consideration for possible incorporation into a future edition of the ASME Code.

E.1.2 Effect of R/t Ratio on Elastic-Plastic Fracture Mechanics (EPFM) Analyses

E.1.2.1 Existing *J*-Estimation Schemes - The *J*-estimation schemes for surface-flawed pipes have elastic and plastic contributions. The elastic solutions are known since there are tabular elastic *F*-functions for global bending and axial tension available in the literature. Furthermore, these tabulated values have been curve fit to simple mathematical expressions as discussed above.

The elastic-plastic contributions to *J* are more difficult to establish. During past NRC programs on piping, several circumferential surface-cracked-pipe *J*-estimation schemes were developed for Class 1 piping where the *R*/*t* ratios were less than 15. These estimation schemes are available in the NRCPIPES computer code, Ref. E.3. The surface-cracked pipe *J*-estimation scheme options in NRCPIPES are designated by the following procedures:

- SC.TNP1 and SC.TNP2,
- SC.TKP1 and SC.TKP2, and
- SC.ENG1 and SC.ENG2.

The differences in these solutions are briefly noted below.

- SC.TNP1 is the original SC.TNP solution by Ahmad in NUREG/CR-4872, Ref.E.4. This analysis used the 360-degree GE/EPRI surface-crack *h*-functions with a ***thin***-shell assumption in estimating the circumferential finite length surface flaw *h*-functions for pipes in bending.

- SC.TNP2 is a modification by Rahman in NUREG/CR-6298, Ref. E.5. This was a modification to the Ahmad solution where the distance from the crack plane to the point where the stress matched that of the unflawed pipe was modified. This length has been calibrated against numerous finite element (FE) analyses. The original assumption in the Ahmad SC.TNP solution (SC.TNP1) was that this distance was equal to the pipe thickness. Rahman found that this distance (L_W) was equal to the pipe thickness (t) times a function of the material strain-hardening exponent (n), i.e., $L_W = (n-1)*t$. This analysis was limited to pipes with $R/t \cong 7.5$.

- SC.TKP1 is the original SC.TKP solution by Ahmad in NUREG/CR-4872, Ref. E.4. This analysis used the 360-degree GE/EPRI surface-crack *h*-functions with a ***thick***-shell assumption in creating the circumferential finite length surface flaw *h*-functions for pipes in bending.

- SC.TKP2 is a modification by Rahman in NUREG/CR-6298, Ref. E.5. This was a modification to the Ahmad solution where the distance from the crack plane to the point where the stress matched that of the unflawed pipe was modified. This length has been calibrated against numerous finite element analyses. The original assumption in the Ahmad SC.TKP solution (SC.TKP1) was that this distance was equal to the pipe thickness. Rahman found that this distance (L_W) was equal to the pipe thickness (t) times a function of the material strain-hardening exponent, i.e., $L_W = [(n+1)/(2n+1)]t$. Again, only pipes with $R/t \cong 7.5$ were used to develop this equation.

- SC.ENG1 is an estimation scheme developed by Rahman for circumferential surface flaws that parallels the circumferential through-wall-cracked pipe estimation scheme of Brust in NUREG/CR-4853 and NUREG/CR-6235, Refs. E.6 and E.7, respecttively. The Brust circumferential through-wall-cracked pipe estimation scheme was called LBB.ENG. Rahman's SC.ENG1 analysis used the ***original*** Net-Section-Collapse limit-load equations in calculating a parameter, $H(a/t)$, which was equal to the thickness of the unflawed pipe divided by an equivalent thickness needed to reach limit-load conditions.

- SC.ENG2 is an estimation scheme developed by Rahman for circumferential surface flaws that also parallels the through-wall-cracked pipe estimation scheme of Brust, Refs. E.6 and E.7. Rahman's SC.ENG2 analysis used the ***Kurihara modification of the original*** Net-Section-Collapse limit-load equations in calculating a parameter, $H(a/t)$, which was equal to the thickness of the unflawed pipe, divided by an equivalent thickness needed to reach limit-load conditions. The Kurihara solution modified the original Net-Section Collapse equations empirically so they would be more accurate for short, deep flaws, Ref. E.8.

Work done by Mohan and others for validation of the ASME FAD curve approach in Code Case N494-2, Ref. E.9, showed that several investigators obtained the same J versus moment values using 3D calculations and line-spring analyses. The results also showed that the Code-Case N494-2 was restricted to a maximum R/t of 15 to avoid under predicting the crack-driving force, see Figure E.4.

E.1.2.2 Objective of the Higher R/t Analysis - This task involved the development of analyses to evaluate circumferential surface flaws in nuclear pipe with radius-to-thickness (R/t) ratios greater than 15. This effort used the finite element method to assess the crack-driving force for higher R/t pipe. The results were then compared with existing estimation schemes available in the NRCPIPES computer code. The objective was to determine if a correction could be applied to one of the schemes available in NRCPIPES to obtain a more accurate estimation of the J versus moment behavior for higher values of R/t, rather than to develop a new *J*-estimation procedure that required a separate option to be programmed into NRCPIPES. This was a less costly option to stay within budgeting restrictions.

E.1.2.3 Approach - The first part of this task was to generate *J* versus bending moment curves for pipes with internal circumferential surface flaws with or without internal pressure. The surface flaws were centered in the plane of the bending on the tension side of the pipes. The *J* values were taken at the mid-length of the surface cracks, i.e., the location with maximum nominal tension stress. The bending moment was generated by application of a rotational

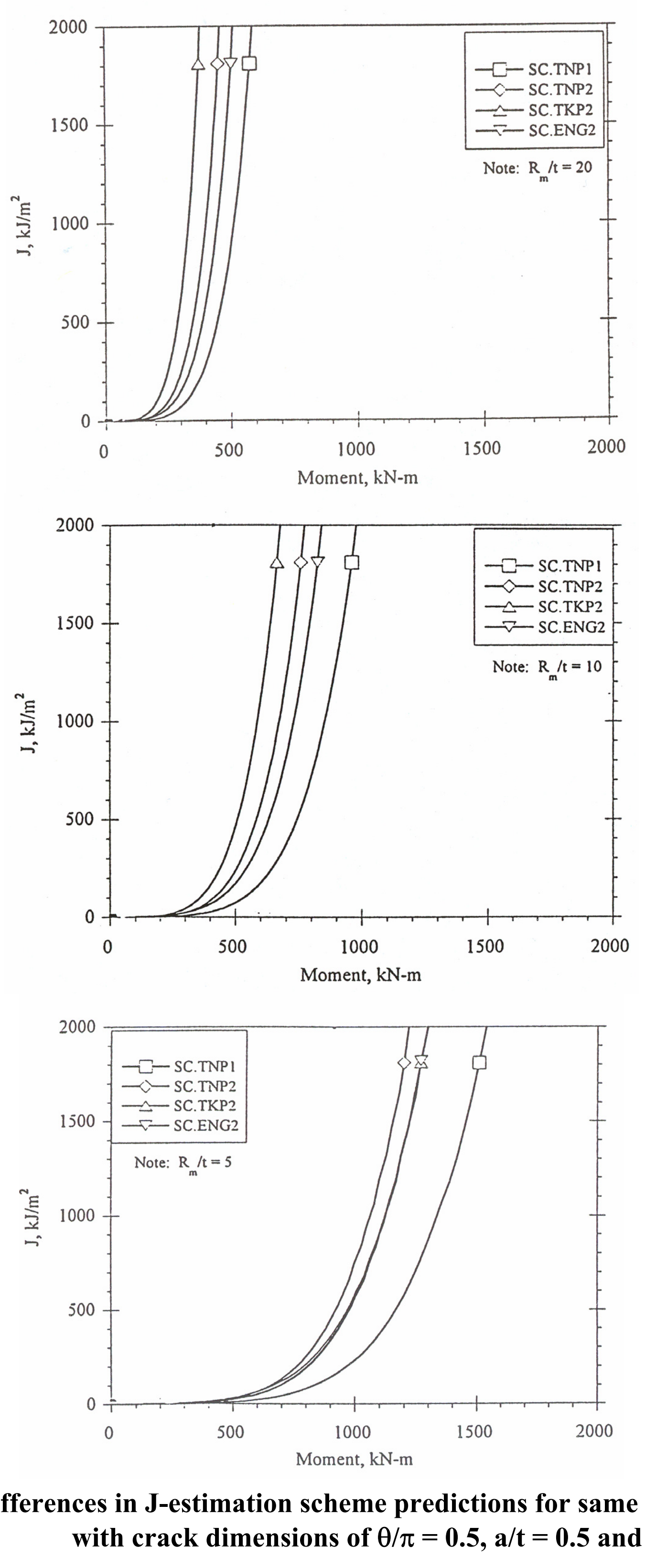

Figure E.4 Differences in J-estimation scheme predictions for same diameter pipe with crack dimensions of $\theta/\pi = 0.5$, $a/t = 0.5$ and $n = 5$

displacement to a cross-sectional plane of the pipe far from the crack plane. The location was a sufficient distance away from the crack plane to minimize the effects of the loading method on the behavior of the crack.

The pipe geometry used in the analyses consisted of a fixed mean radius (R_m) of 184.7 mm (7.27 inches). The pipe wall thickness (t) was calculated from the R_m/t ratio. For calculations involving the R_m/t ratio, the value of the radius used in this investigation was always the mean radius. R_m/t ratios of 5, 20, 40, and 60 were considered in the analyses. The results for R_m/t of 5 were considered the baseline, since the NRCPIPES estimation schemes were expected to yield similar results at this ratio.

The internal circumferential surface crack geometry was defined by the crack depth-to-thickness ratio (a/t) and the crack length-to-circumference ratio (θ/π). Crack depth ratios (a/t) of 0.25, 0.50, and 0.75 were used in the analyses. Likewise, crack length ratios (θ/π) of 0.25 and 0.50 were used.

The material properties for the analyses were typical of nuclear piping steels. The modulus of elasticity (E) was 182.72 GPa (26,500 ksi) and the Poisson's ratio (ν) was 0.3. The stress-strain relation was assumed to obey the generic Ramberg-Osgood power-law hardening equation,

$$\frac{\varepsilon}{\varepsilon_0} = \frac{\sigma}{\sigma_0} + \alpha\left(\frac{\sigma}{\sigma_0}\right)^n , \tag{E.7}$$

where σ_0 and $\varepsilon_0 = \sigma_0/E$ are the reference yield stress and strain, respectively, and α is a dimensionless parameter. The reference stress (σ_0) was 150 MPa (21.8 ksi). From these data, the reference strain (ε_0) was calculated to be 820 μm/m.

Four sets of problems and the associated geom.-etry, material properties, and loading conditions are summarized in Table E.2. The analyses were conducted using the ABAQUS® general-purpose finite element code (Version 6.2-1).

Finite Element Geometric Models – The finite element models were constructed using shell and line-spring elements. A typical model is shown in Figures E.5 and E.6. Only one quarter of the pipe was modeled due to the symmetry conditions. The shell and line-spring elements were type S8R5 and LS3S per ABAQUS® notation, respectively. There were ten equally spaced line-spring elements covering the one-half length crack front in the model. Fourteen (14) shell elements were geometrically spaced around the circumference, with smaller elements in the region adjacent to the crack. The axial length of the quarter model was $10D_m$ where D_m is the mean diameter of the pipe.

Applied Loading - Bending loads were imposed on the pipe section by applying a rotation at the far end of the pipe along a plane perpendicular to the axis of the pipe. In the shell and line-spring element models, the nodes on the far end of the pipe were tied to a reference node through the "*KINEMATIC COUPLING" command provided in ABAQUS®. The rotational degree of freedom applied to the reference node was then transferred to the end of the pipe through this coupling constraint. The end of the pipe where the rotations were applied was sufficiently far from the crack plane so that there were no extraneous effects at the crack surface due to the loading.

In the cases with internal pressure loading, the internal pressure and the associated axial load were applied first. The ends of the pipe were allowed to freely rotate when the pressure was applied. The magnitude of the axial load represented the end cap load from the internal pressure. The rotational displacement to produce the applied moment was applied afterward. There was no pressure applied to the crack face in the cases with internal pressure loading.

Finite Element Procedure Formulation - Small-strain formulation was used for all of the analyses. The Ramberg-Osgood stress-strain relation of Equation E.7 conforms to the "*DEFORMATION PLASTICITY" definition of ABAQUS®; however, the "*DEFORMATION PLASTICITY" definition does not work with the line-spring element.

Table E.2 Analysis matrix and dimensional and material parameters

Rm/t	5, 20, 40, 60			Rm	184.725	mm	E	182.72	GPa	Ramberg-Osgood			
θ/π	0.25, 0.50			Dm	369.45	mm	σo	150.00	MPa	$\frac{\varepsilon}{\varepsilon_o} = \frac{\sigma}{\sigma_o} + \alpha \left(\frac{\sigma}{\sigma_o} \right)^n$			
a/t	0.25, 0.50, 0.75			t	(variable)	mm	εo	0.000821	σo/E				
P(i)	0, P(i) s.t. σ(h)=1.0*Sm			Rm=(Do-t)/2	(variable)	mm	v	0.30					
σ - ε	n=5 (n=3, 7, 10)			L >= 10*Dm	3694.5	mm	Sm (MPa)	122.5					
	α=1												
Rm/t	**a/t**	**θ/π**	**Internal Pressure**	**Do (mm)**	**Thickness t (mm)**	**Crack Depth, a (mm)**	**Crack Length, s (mm)**	**a/s**	**Ri=Rm-t/2 (mm)**	**Internal Pressure (MPa)**	**Axial Load (N)**	**I (m^4)**	**Limit Moment (MN-m)**
5	0.25	0.25	0	406.40	36.945	9.236	145.1	0.064				7.3893E-04	1.3718
			Sm						166.25	24.020	1,042,851		1.2852
		0.50	0			9.236	290.2	0.032					1.1718
			Sm										1.1718
	0.50	0.25	0	406.40	36.945	18.473	145.1	0.127					1.0935
			Sm						166.25	24.020	1,042,851		1.0935
		0.50	0			18.473	290.2	0.064					1.0189
			Sm										0.8281
	0.75	0.25	0	406.40	36.945	27.709	145.1	0.191					0.8887
			Sm						166.25	24.020	1,042,851		0.8887
		0.50	0			27.709	290.2	0.095					0.4380
			Sm										0.4380
20	0.25	0.25	0	378.69	9.236	2.309	145.1	0.016				1.8302E-04	0.3146
			Sm						180.11	6.095	310,542		0.3146
		0.50	0			2.309	290.2	0.008					0.2846
			Sm										0.2845
	0.50	0.25	0	378.69	9.236	4.618	145.1	0.032					0.2649
			Sm						180.11	6.095	310,542		0.2649
		0.50	0			4.618	290.2	0.016					0.1955
			Sm										0.1955
	0.75	0.25	0	378.69	9.236	6.927	145.1	0.048					0.2122
			Sm						180.11	6.095	310,542		0.2122
		0.50	0			6.927	290.2	0.024					0.0954
			Sm										0.0954

Table E.2 Analysis matrix and dimensional and material parameters (continued)

Rm/t	a/t	θ/π	Internal Pressure	Do (mm)	Thickness t (mm)	Crack Depth, a (mm)	Crack Length, s (mm)	a/s	Ri=Rm-t/2 (mm)	Internal Pressure (MPa)	Axial Load (N)	I (m^4)	Limit Moment (MN-m)
40	0.25	0.25	0	374.07	4.618	1.155	145.1	0.008				9.1466E-05	0.1253
			Sm						182.42	3.055	159,675		0.1566
		0.50	0			1.155	290.2	0.004					0.1414
			Sm										0.1414
	0.50	0.25	0	374.07	4.618	2.309	145.1	0.016					0.1317
			Sm						182.42	3.055	159,675		0.1317
		0.50	0			2.309	290.2	0.008					0.0967
			Sm										0.0967
	0.75	0.25	0	374.07	4.618	3.464	145.1	0.024					0.1051
			Sm						182.42	3.055	159,675		0.1051
		0.50	0			3.464	290.2	0.012					0.0464
			Sm										0.0464
60	0.25	0.25	0	372.53	3.079	0.7697	145.1	0.005				6.0972E-05	0.0950
			Sm						183.19	2.038	107,440		0.1043
		0.50	0			0.7697	290.2	0.003					0.0942
			Sm										0.0942
	0.50	0.25	0	372.53	3.079	1.539	145.1	0.011					0.0876
			Sm						183.19	2.038	107,440		0.0876
		0.50	0			1.539	290.2	0.005					0.0643
			Sm										0.0643
	0.75	0.25	0	372.53	3.079	2.309	145.1	0.016					0.0699
			Sm						183.19	2.038	107,440		0.0699
		0.50	0			2.309	290.2	0.008					0.0307
			Sm										0.0307

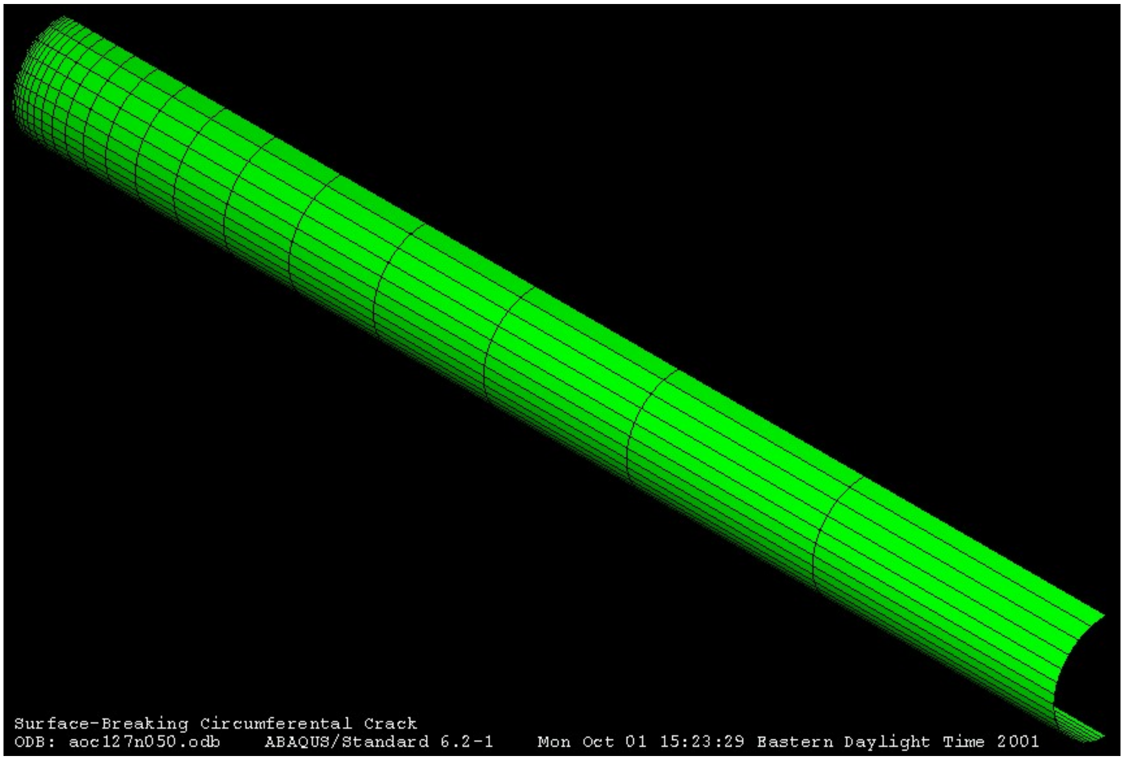

Figure E.5 A typical model using shell and line-spring elements

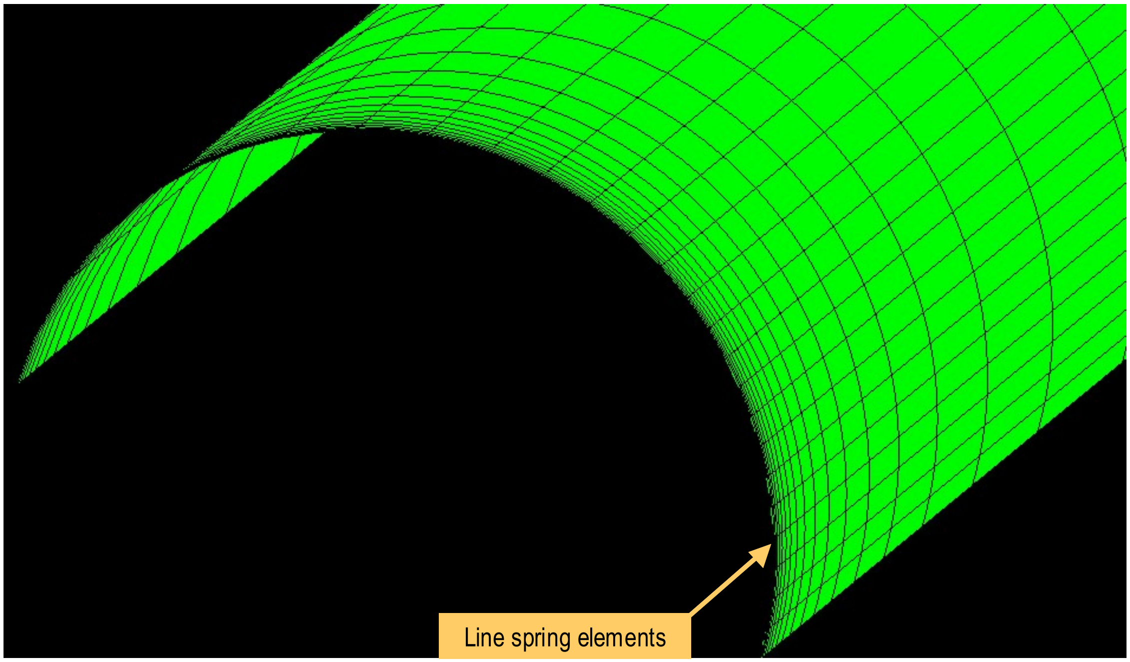

Figure E.6 Focused view of the shell and line-spring model, looking at the cross-sectional plane containing the line-spring elements

Therefore, the material properties were defined by the "*ELASTIC" and "*PLASTIC" commands in ABAQUS®. The first line of the "*PLASTIC" command defines the plastic flow stress at zero plastic strain. In the case of the Ramberg-Osgood stress-strain relation, the nonlinearity starts at zero stress. Strictly speaking, the first line in the "*PLASTIC" command would have zero plastic flow stress at zero plastic strain; however, ABAQUS® does not allow zero plastic flow stress at zero plastic strain. Consequently, a small finite plastic flow stress corresponding to zero plastic strain must be specified. The examination of the analysis results revealed that the magnitude of this finite plastic flow stress at zero plastic strain does not affect the J versus moment relation, provided the initial flow stress was less than one-third of the reference yield stress, $\mathbf{F}_0$.

E.1.2.4 Analysis Results – The results from the analyses are presented next.

Confirmation of the Analysis Procedure - To ensure the quality of the results, it was necessary to verify that the stress and strain state at the cracked plane was not affected by the boundary conditions applied at the far end of the model. The deformed shell and line-spring model, shown in Figure E.7, demonstrates that the cross-section at the far end of the pipe remains circular. Figure E.8 shows that the axial stress has the expected circumferential variation. This variation is independent of axial position for much of the model, except in the region close to the crack plane. As expected, the axial stress redistributes near the crack plane due to the reduced load-carrying capability along the length of the surface crack. The deformation and stress contours of Figures E.7 and E.8 confirm that the stress and strain states in the crack plane are free of end effects.

J versus moment Curves from Finite Element Analyses - One of the objectives of this task was to provide J versus moment curves so the *J*-estimation schemes from NRCPIPES can be investigated at higher R_m/t ratios. This section compares the J versus moment relationships generated from the finite element analyses. The results are plotted in the following figures based on R_m/t ratios and internal pressure. Figure E.9 shows the results of J versus moment for $R_m/t = 5$. As expected, the results in Figure E.9 show an increase in the crack driving force as the crack size, both length and depth, increases. The plots show a slight difference with change in crack length and a more significant increase in the driving force with increase in crack depth. Likewise, the crack-driving force increases with the application of internal pressure for the same crack size.

The results for $R_m/t = 20$ are shown in Figure E.10. These data show similar trends to the $R_m/t = 5$ results; however, the crack-driving force is significantly greater at the higher R_m/t for the same crack geometry. Likewise, these results show only a slight difference for the two crack lengths, but a significant difference as the crack depth changes.

These trends are also evident in the results for $R_m/t = 40$ and $R_m/t = 60$, as shown in Figures E.11 and E.12, respectively.

Following completion of the finite element analyses for all the cases in Table E.2, the J versus moment data was curve fit using a polynomial regression. The regression was then used to normalize the *J* results from the NRCPIPES output (J_{est}) with respect to the J value from the finite element analysis (J_{fe}). The ratio of J_{est}/J_{fe} provides an indication of the accuracy in the estimation scheme.

***J E*stimation Results from NRCPIPES -** The NRCPIPES program was used to investigate the various *J*-estimation schemes available for predicting J versus moment behavior for internal circumferential surface cracks. The six estimation schemes previously discussed (SC.TNP1, SC.TNP2, SC.TKP1, SC.TKP2, SC.ENG1, SC.ENG2) were used to generate J versus moment curves for the cases of $R_m/t = 5$, 20, and 40 and $a/t = 0.5$, $\theta/\pi = 0.25$, and $P_i = 0$. These corresponded to cases from the BINP Round Robin 2 problem set, see Appendix I. The results suggested that the SC.TNP2 estimation scheme produced the best approximation of the J versus moment behavior for the higher values

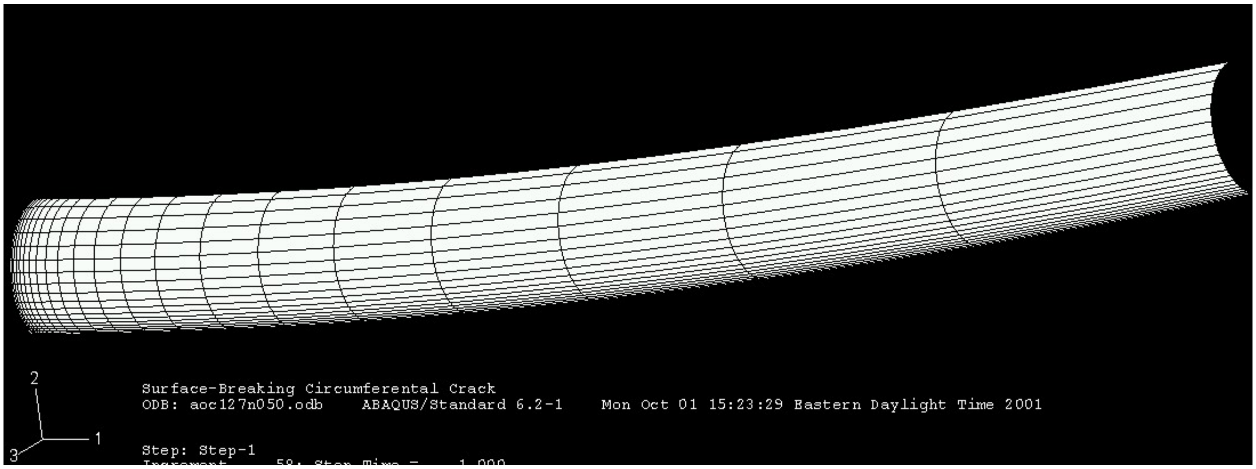

Figure E.7 A deformed shell and line-spring model

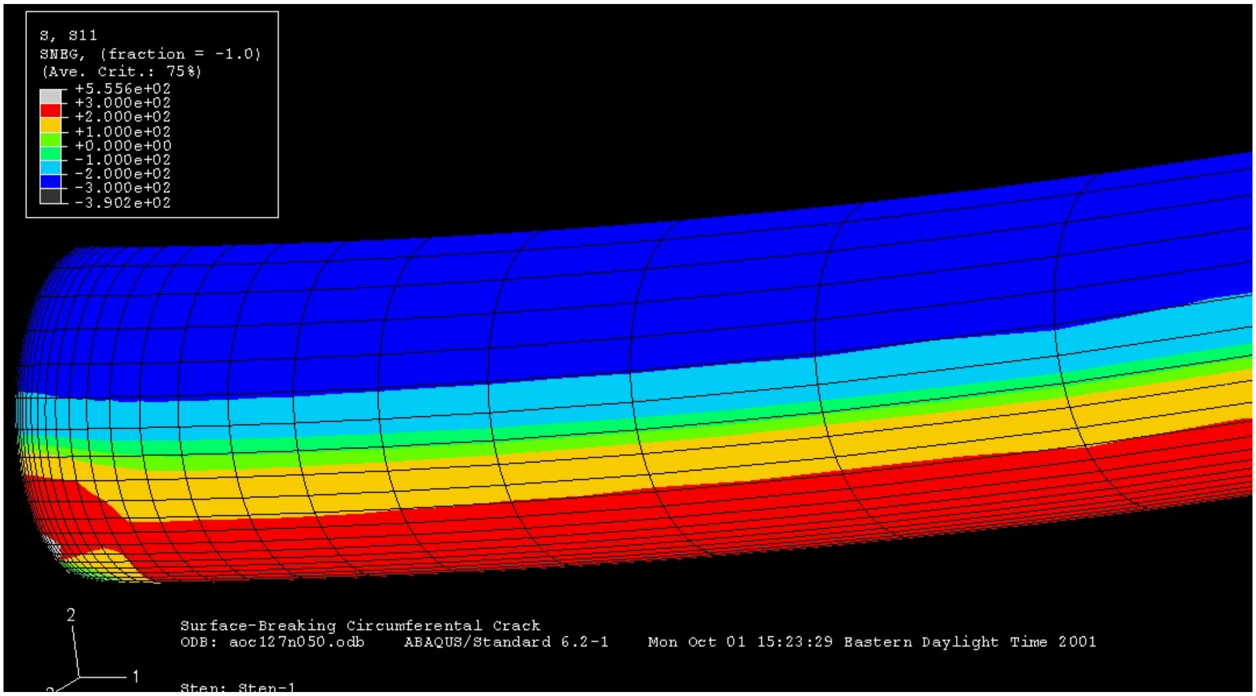

Figure E.8 Axial stress contours of a deformed shell and line-spring model

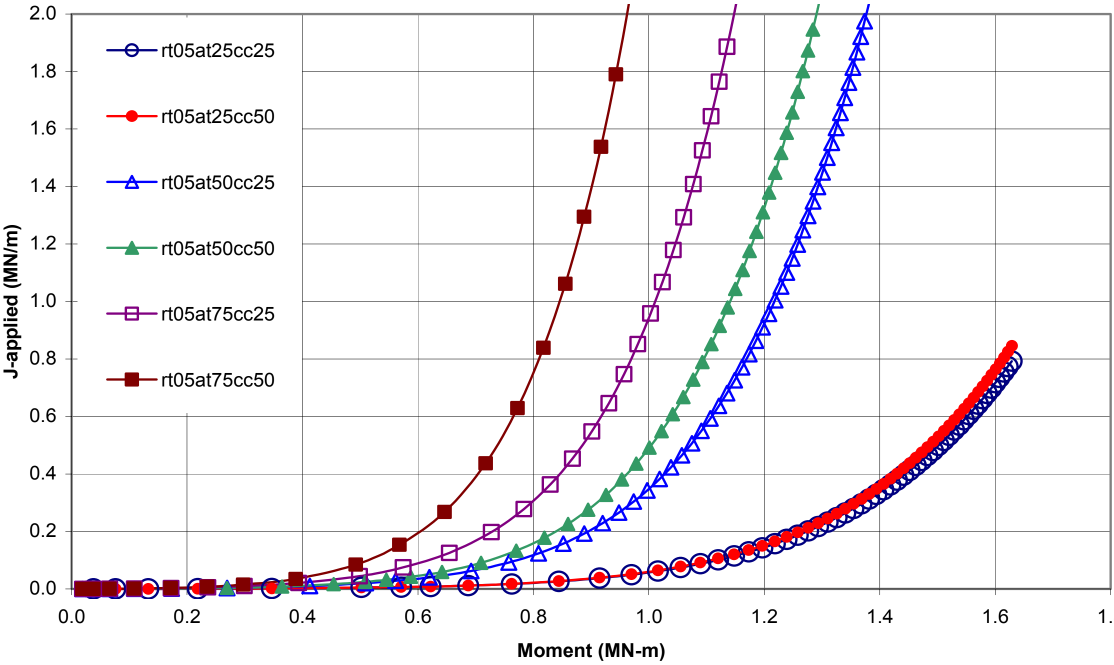

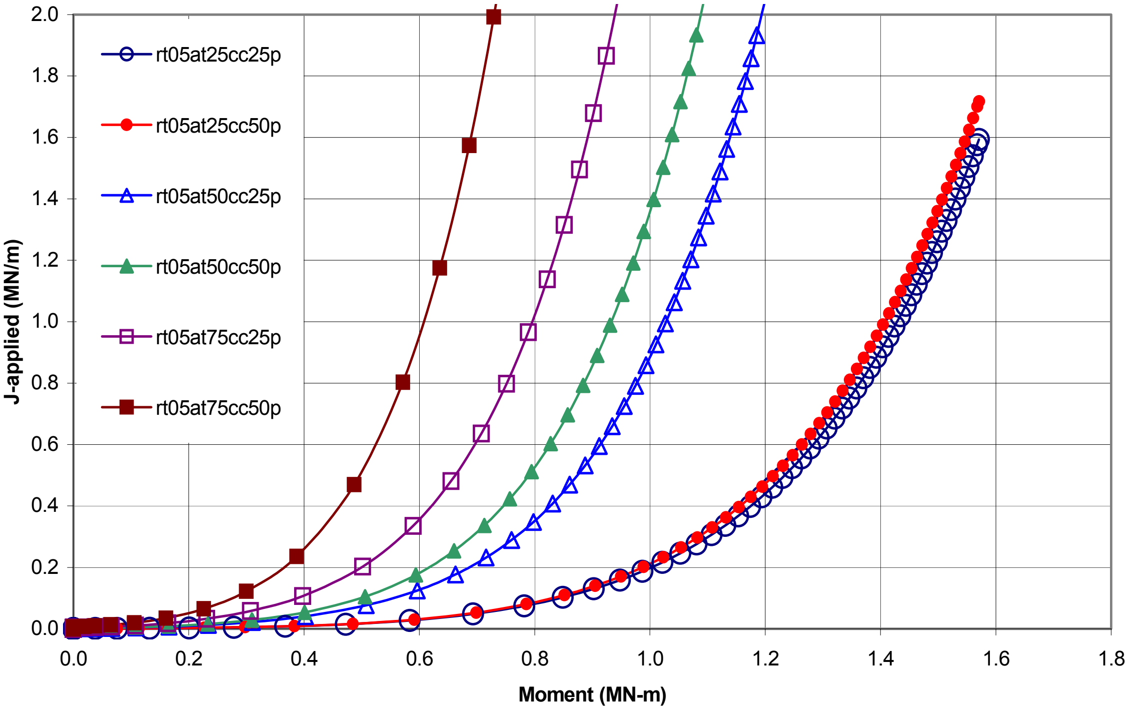

Figure E.9 J versus moment from finite element analyses for Rm/t = 5 and all a/t and θ/π values investigated. (Top) no internal pressure (Bottom) internal pressure (Notation: rt05→ Rm/t = 5, at 25→ a/t = 0.25, cc25→θ/π = 0.25, p→pressure)

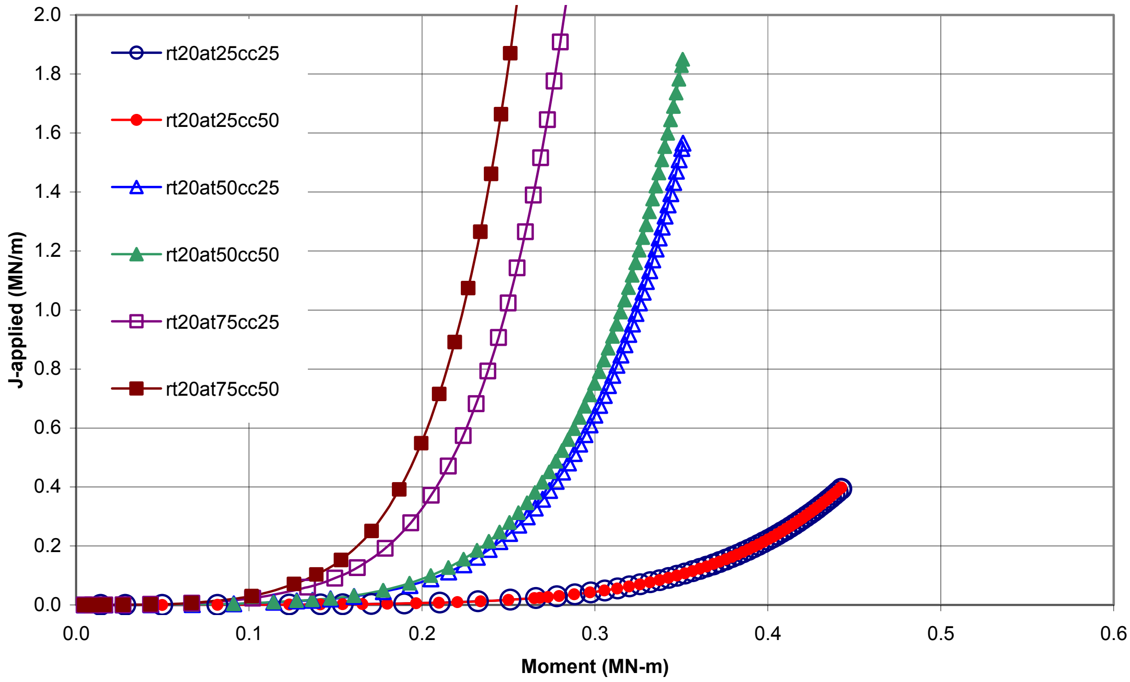

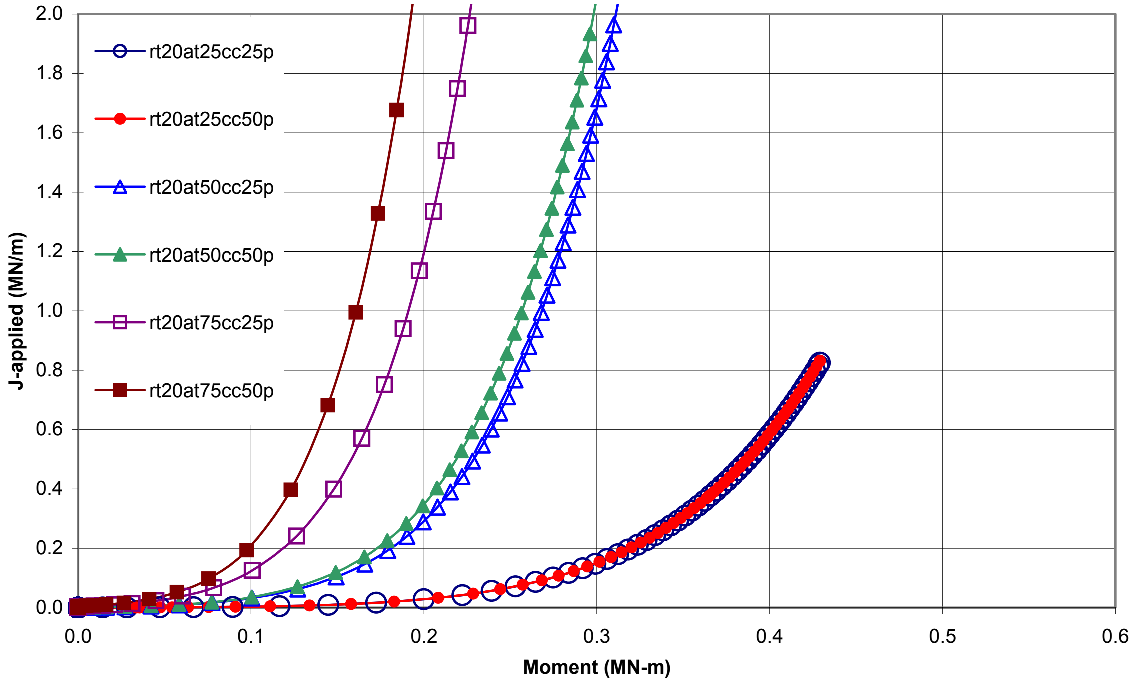

Figure E.10 J versus moment from finite element analyses for Rm/t = 20 and all a/t and θ/π values investigated. (Top) no internal pressure (Bottom) internal pressure (Notation: rt20→ Rm/t = 20, at25→ a/t = 0.25, cc25→θ/π = 0.25, p→pressure)

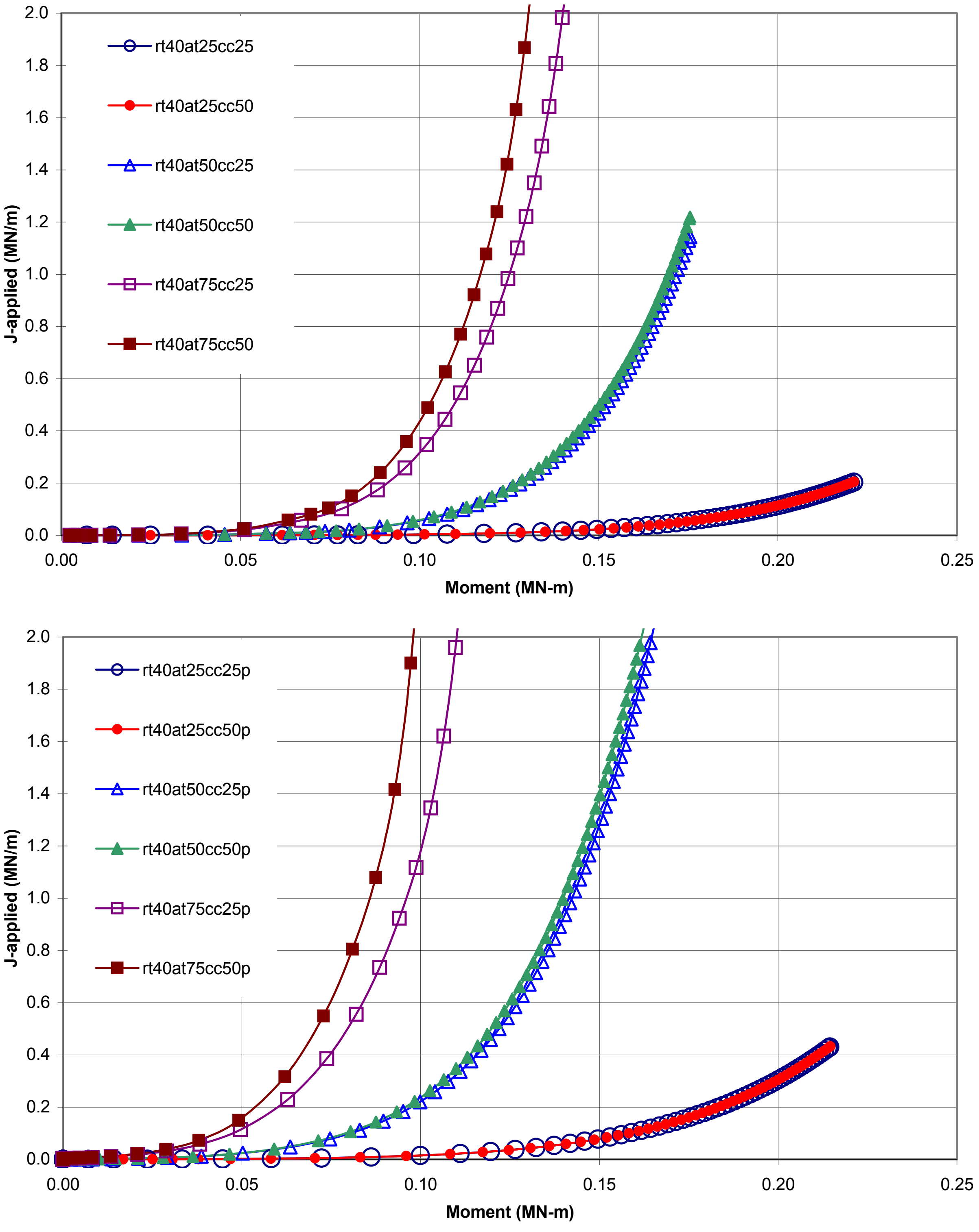

Figure E.11 J versus moment from finite element analyses for Rm/t = 40 and all a/t and θ/π values investigated. (Top) no internal pressure (Bottom) internal pressure (Notation: rt40→ Rm/t = 40, at25→ a/t = 0.25, cc25→θ/π = 0.25, p→pressure)

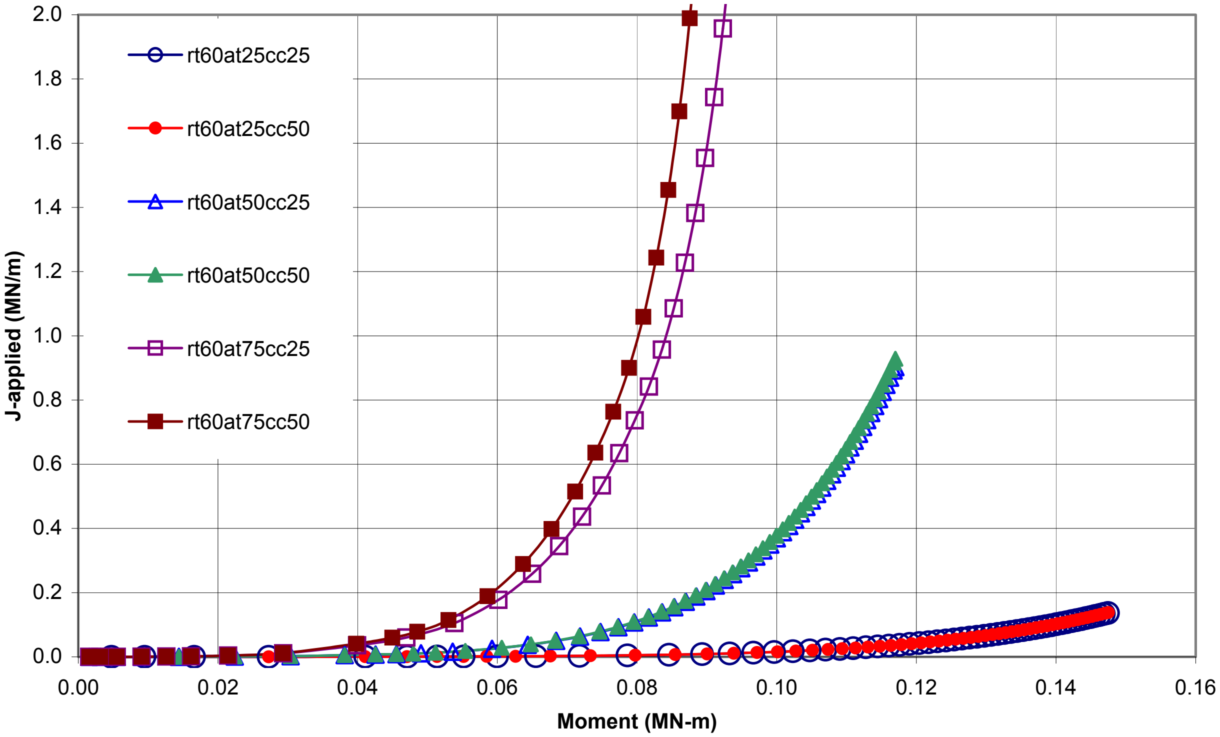

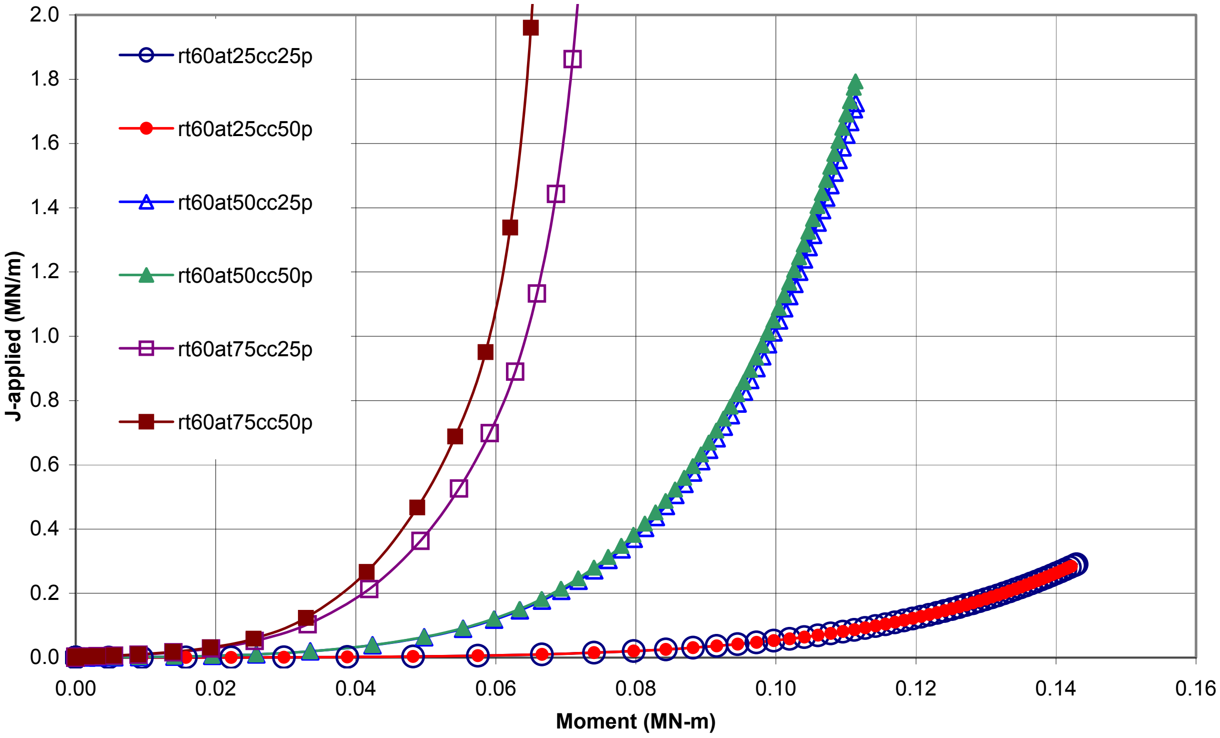

Figure E.12 J versus moment from finite element analyses for Rm/t = 60 and all a/t and θ/π values investigated. (Top) no internal pressure (Bottom) internal pressure (Notation: rt60→ Rm/t =60, at25→ a/t = 0.25, cc25→θ/π = 0.25, p→pressure)

of R_m/t. However, the SC.TNP2 method over predicted J at lower R_m/t values (R/t = 5) and under predicted J at higher R_m/t values (R/t = 20 and 40), see Figure E.13.

For each of the cases shown in Table E.2, the NRCPIPES program was run using the SC.TNP1 J-estimation scheme (L_w = t). The approach was to run SC.TNP1 (Lw = t) to establish the relationship between the SC.TNP1 estimation scheme and the FEA results. Then the Lw parameter was varied as a function of t to obtain the best agreement with the FEA results. The results are presented in four groups based on the R_m/t ratio, see Figures E.14 through E.17. For the cases with $R_m/t = 5$ and no internal pressure, the SC.TNP1 results are shown in Figure E.14, along with the FEA results for reference (symbols only). The method provided reasonable agreement with the finite element analyses for the larger size cracks ($\boldsymbol{\theta/\pi} = 0.50$ and $a/t \geq 0.50$); however, the estimation method under predicted the crack-driving force. For the cases with shallow cracks ($a/t = 0.25$) the estimation scheme was conservative and over predicted the crack-driving force. For $R_m/t = 5$ with internal pressure, the SC.TNP1 results are also shown in Figure E.14. These results are similar to those without pressure, except the crack-driving force is higher for each crack size. Also, the estimation scheme for the shallow cracks ($a/t = 0.25$) is no longer conservative relative to the finite element results.

For the cases with $R_m/t = 20$ and no internal pressure, the SC.TNP1 results are shown in Figure E.15. All estimation methods provided non-conservative results with respect to the finite element analyses for the deeper cracks ($a/t \geq 0.50$). For the cases with shallow cracks ($a/t = 0.25$), the estimation scheme was conservative and slightly over predicted the crack-driving force. For $R_m/t = 20$ with internal pressure, the SC.TNP1 results are also shown in Figure E.15. These results are similar to those without pressure, except the crack-driving force is also higher for each crack size. In addition, the estimation scheme for the short, shallow crack ($\theta/\pi = 0.25$ and $a/t = 0.25$) is no longer conservative relative to the finite element results. However, the long, shallow crack ($\theta/\pi = 0.50$ and $a/t = 0.25$) showed excellent agreement with the finite element analysis.

The cases with $R_m/t = 40$ and $R_m/t = 60$ showed trends very similar to those where $R_m/t = 20$. The primary difference is that the crack-driving force increases as the R_m/t ratio increases, for each crack size. The J versus moment curves for $R_m/t = 40$ with and without internal pressure and $R_m/t = 60$ with and without internal pressure are shown in Figures E.16 and E.17, respectively.

E.1.2.5 Correction Factor L_w for SC.TNP - The SC.TNP (SC.TNP1 and SC.TNP2) estimation scheme allows the use of a correction parameter (L_w) to obtain better agreement with finite element analyses for particular geometry and material inputs. It has been shown that the length parameter provides a reasonable correction when related to the pipe thickness for a material with a strain-hardening exponent between 3 and 10 (Ref. E.10). It was decided that the SC.TNP method and the L_w parameter would be investigated as a correction mechanism for higher R_m/t pipe analyses.

The matrix of analyses was previously shown in Table E.2. The NRCPIPES code was run for each of these cases using values of L_w = C1*t. The value of the coefficient C1 was determined such that J from the estimation scheme (J_{est}) was within 10 percent of the J value from the finite element analysis (J_{fe}) for the range of J values representative of nuclear piping materials, (i.e., 88 < J < 350 kJ/m2 [500 < J < 2000 in-lb/in2] for stainless steel welds or carbon steel pipe or welds where EPFM is expected). At these J levels, the total J was dominated by $J_{plastic}$, so that inaccuracies in the $J_{elastic}$ term in the NRCPIPES code are insignificant. For comparison purposes, the cases were placed in four groups based on crack length and internal pressure. Within these groups, the results are compared with respect to R_m/t ratio and crack depth-to-thickness ratio (a/t).

The coefficient C1 is plotted as a function of R_m/t and a/t in Figure E.18 for the cases where the crack length, θ/π, was 0.25 and there was no internal pressure on the pipe. The values of C1

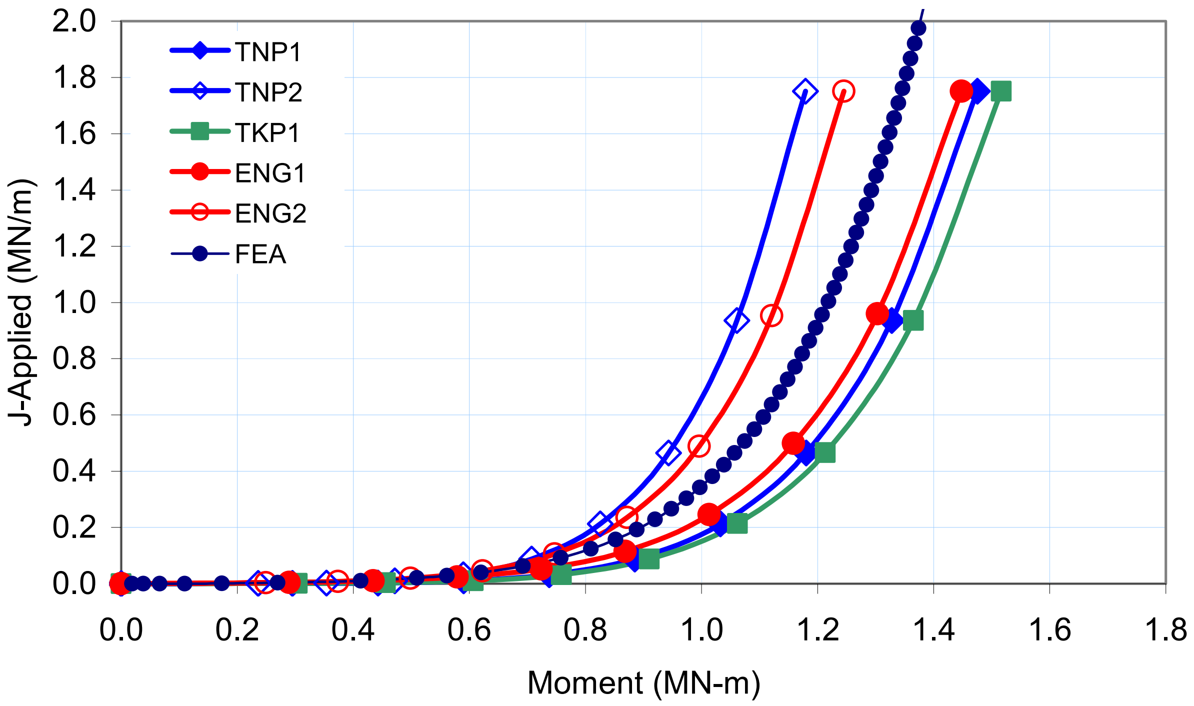

Figure E.13a J versus moment from FEA and NRCPIPES J-estimation schemes for $R_m/t = 5$, a/t= 0.5 and 2/B = 0.25

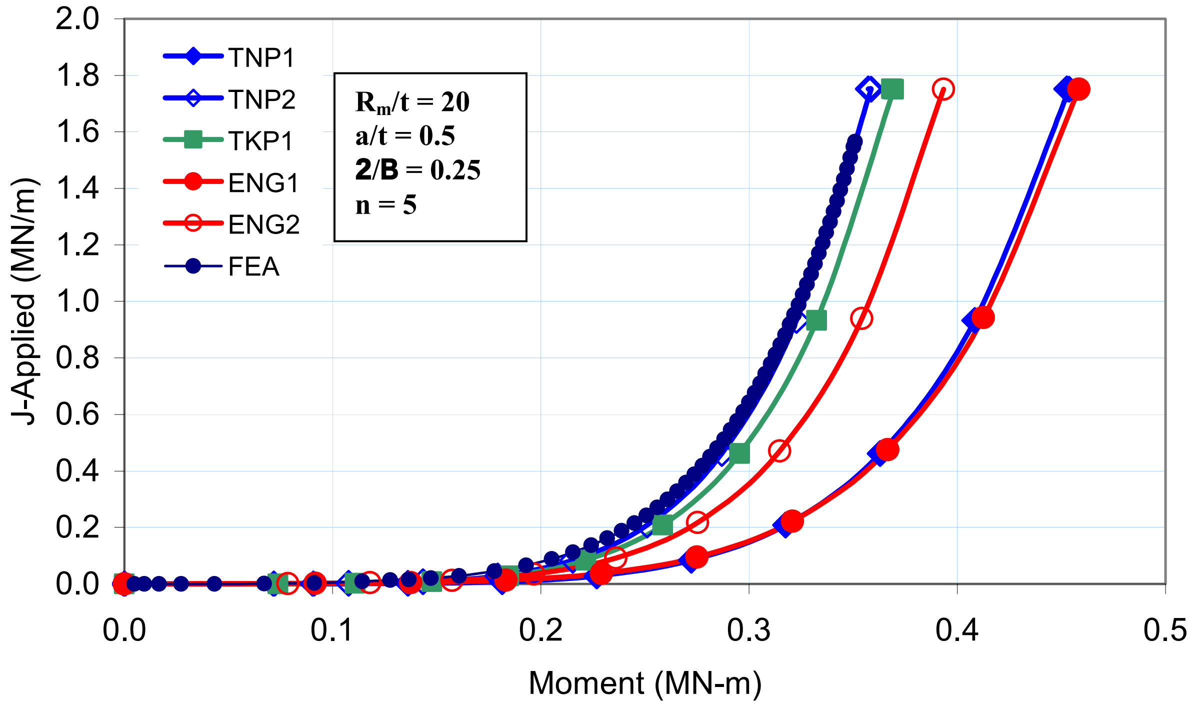

Figure E.13b J versus moment from FEA and NRCPIPES J-estimation schemes for Rm/t = 20, a/t = 0.5, and θ/π = 0.25

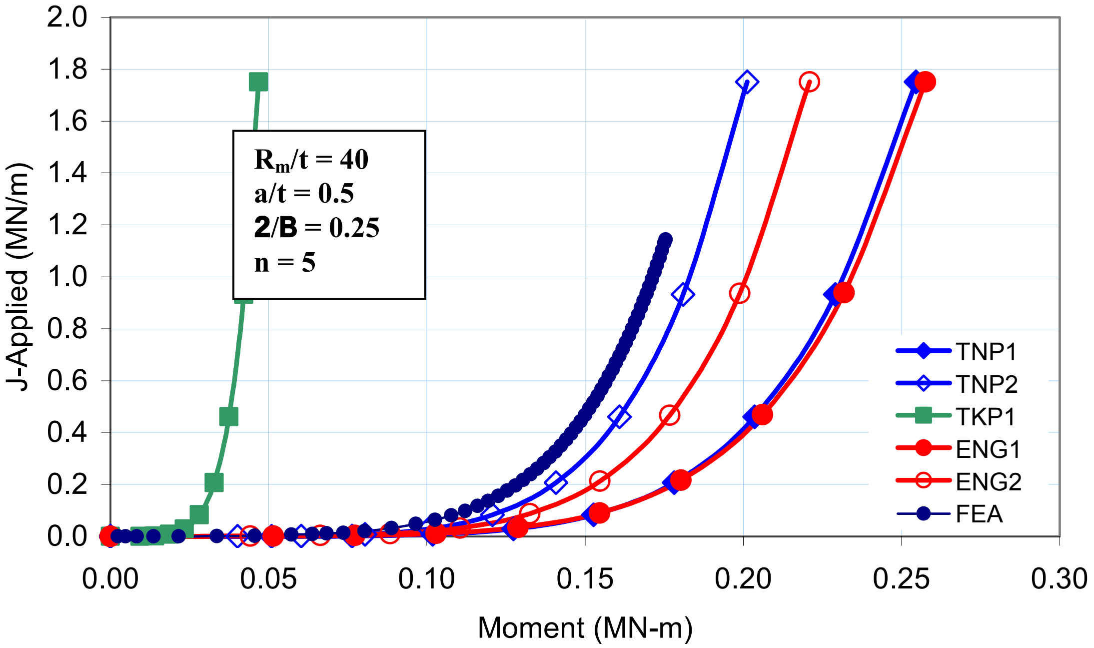

Figure E.13c J versus moment from FEA and NRCPIPES J-estimation schemes for $R_m/t = 40$, a/t= 0.5 and 2/B = 0.25

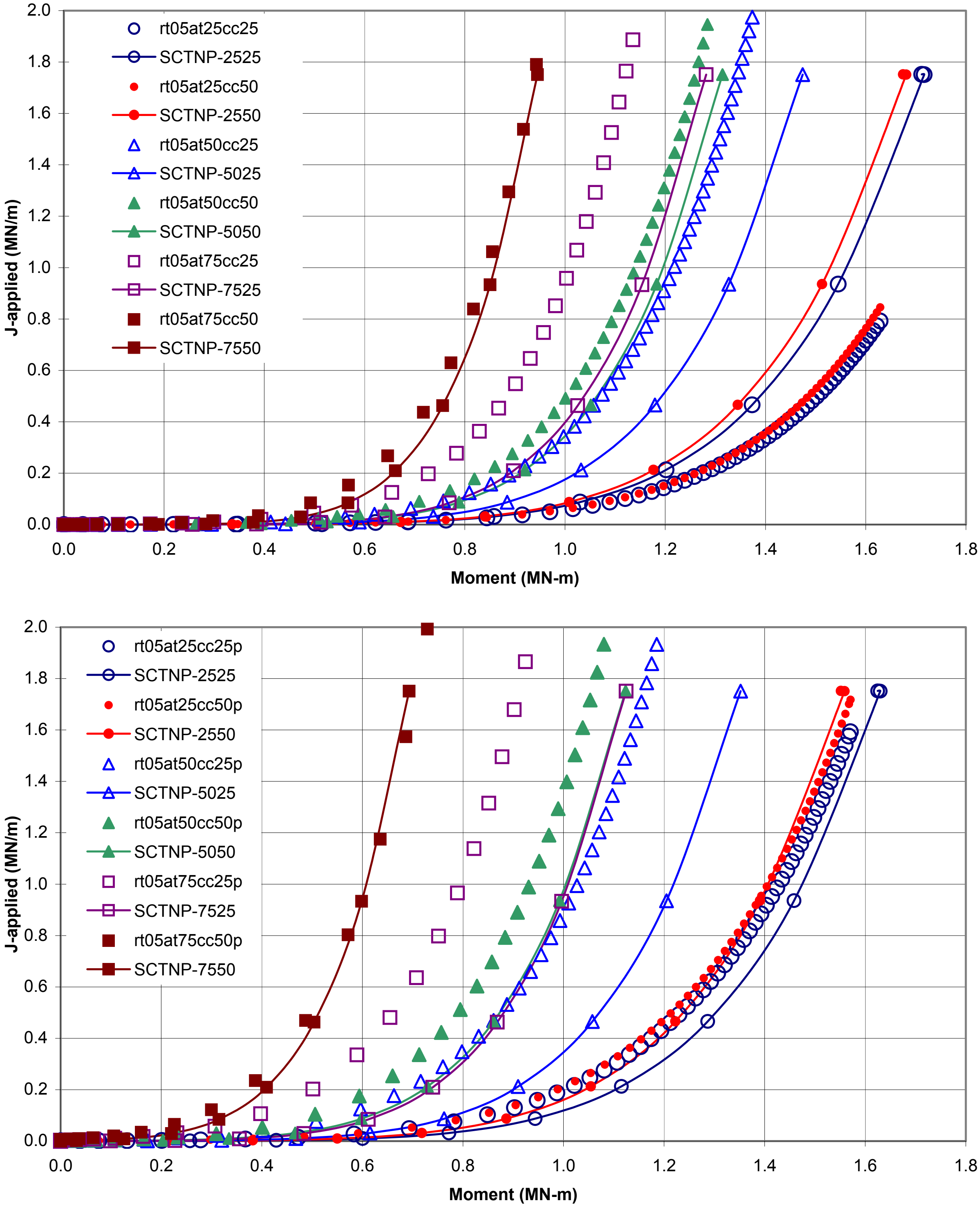

Figure E.14 J versus moment from FEA (symbol) and the SC.TNP1 analysis in NRCPIPES (symbol and line) for Rm/t = 5 and all a/t and θ/π values investigated. (Top) no internal pressure (Bottom) internal pressure (Notation as previously described)

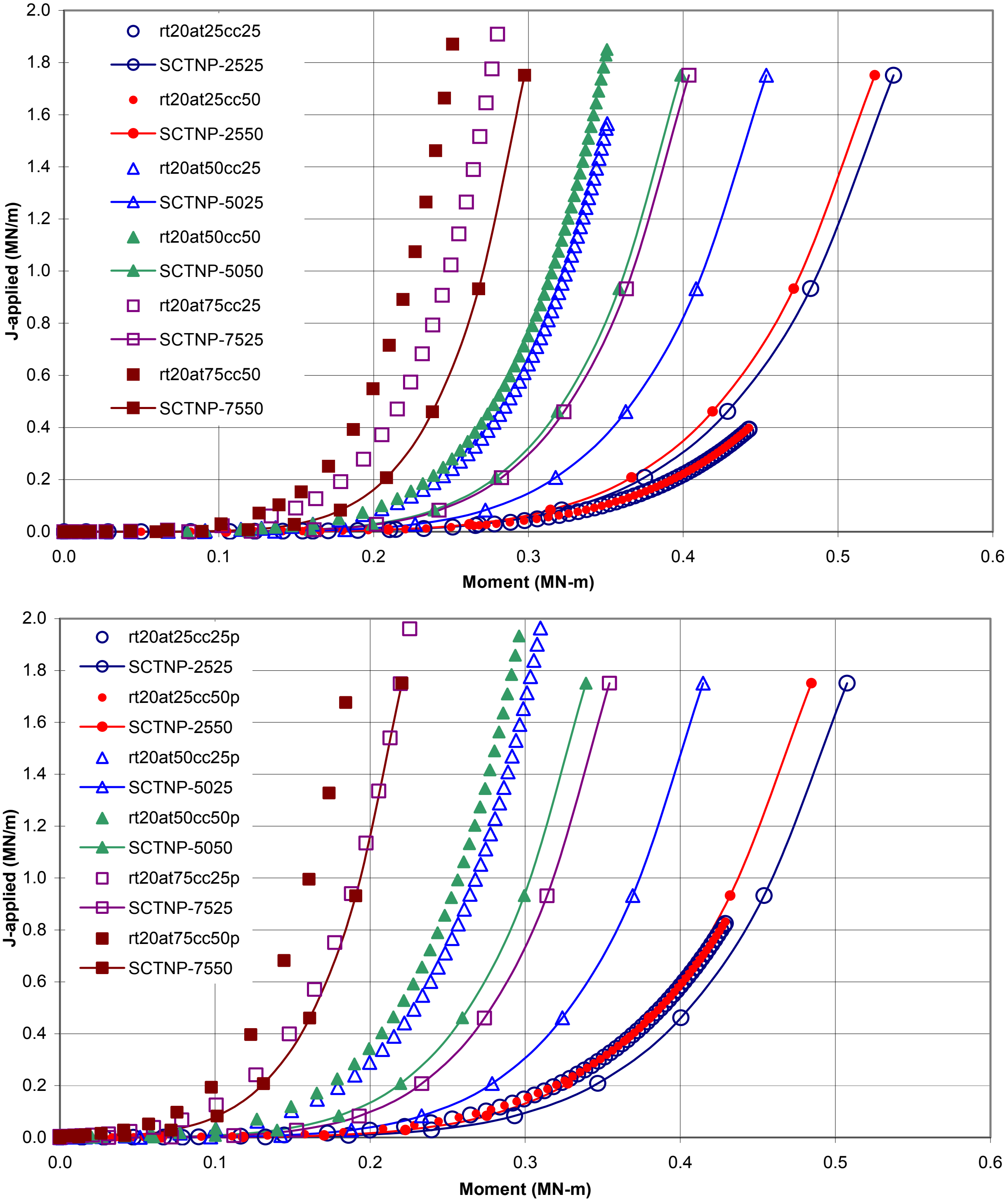

Figure E.15 J versus moment from FEA (symbol) and the SC.TNP1 analysis in NRCPIPES (symbol and line) for Rm/t = 20 and all a/t and θ/π values investigated. (Top) no internal pressure (Bottom) internal pressure (Notation as previously described)

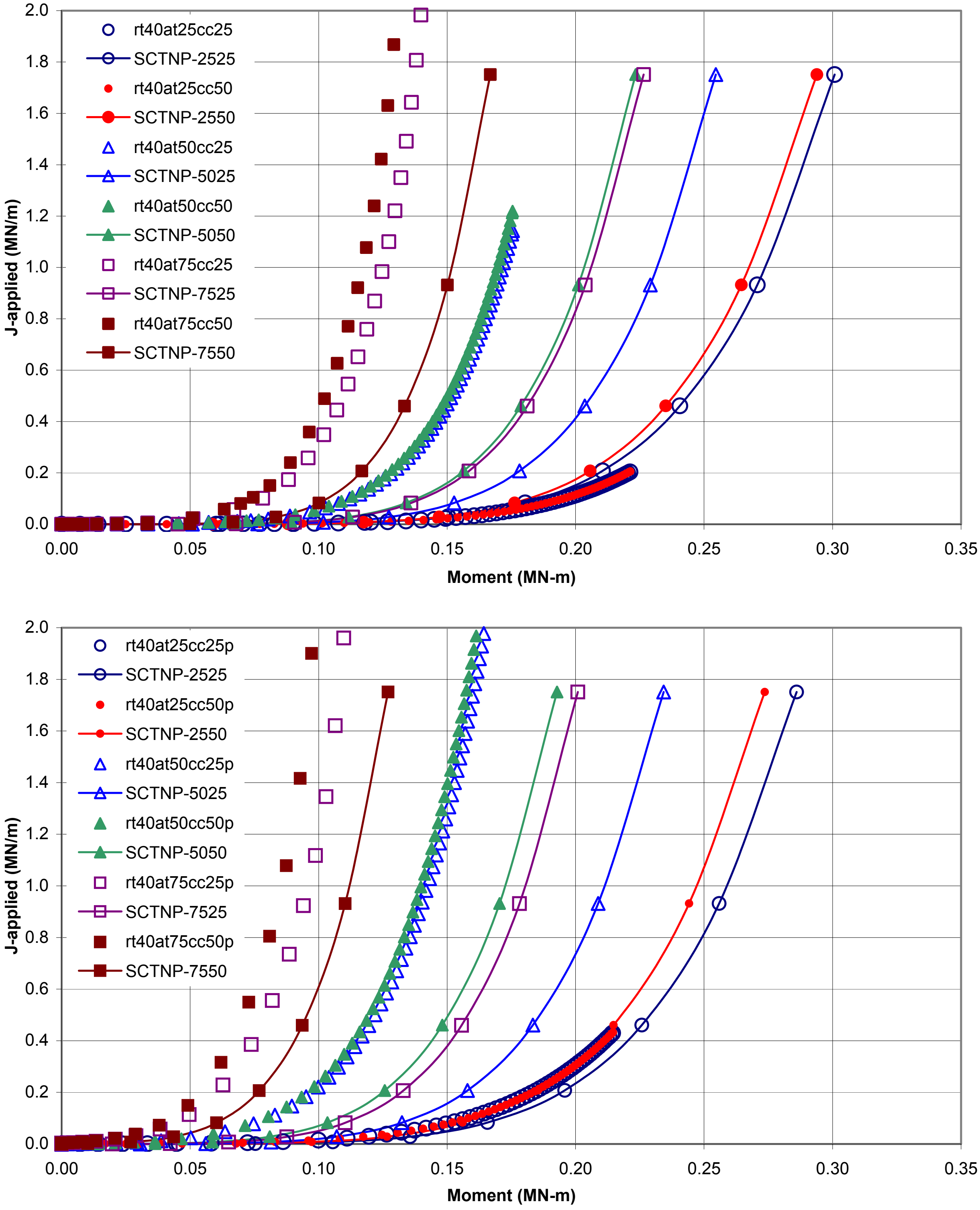

Figure E.16 J versus moment from FEA (symbol) and the SC.TNP1 analysis in NRCPIPES (symbol and line) for Rm/t = 40 and all a/t and θ/π values investigated. (Top) no internal pressure (Bottom) internal pressure (Notation as previously described)

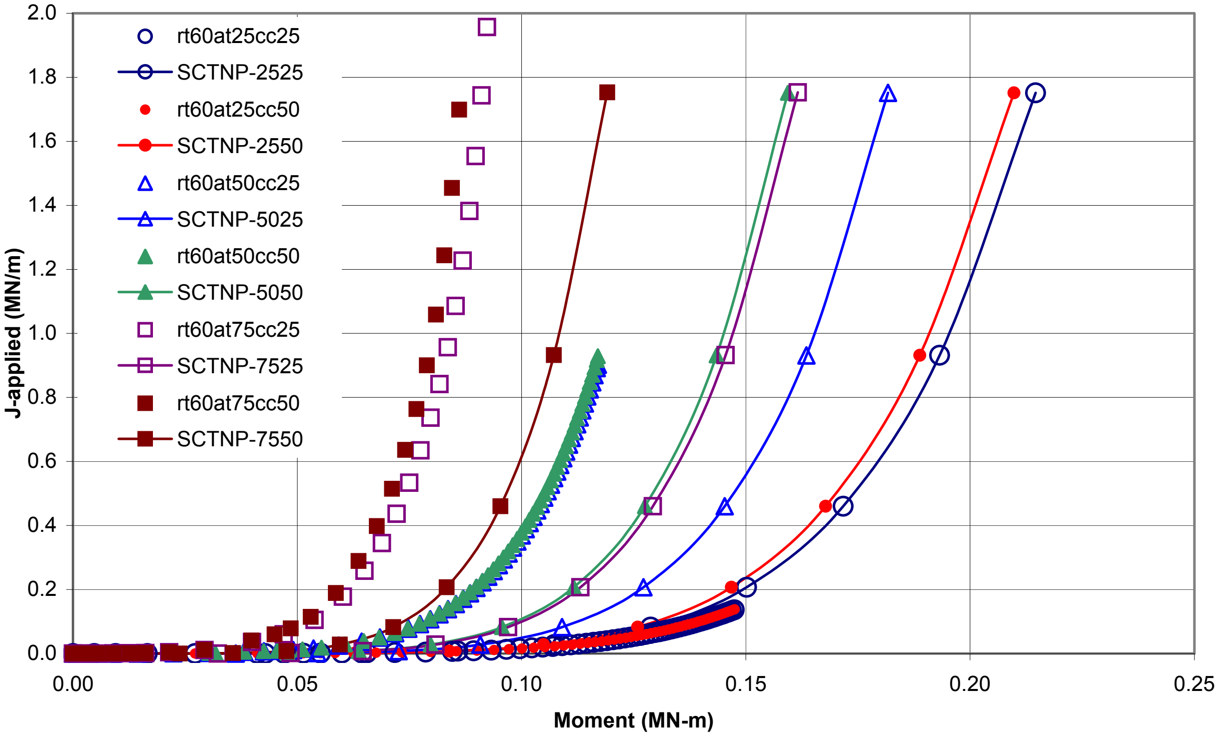

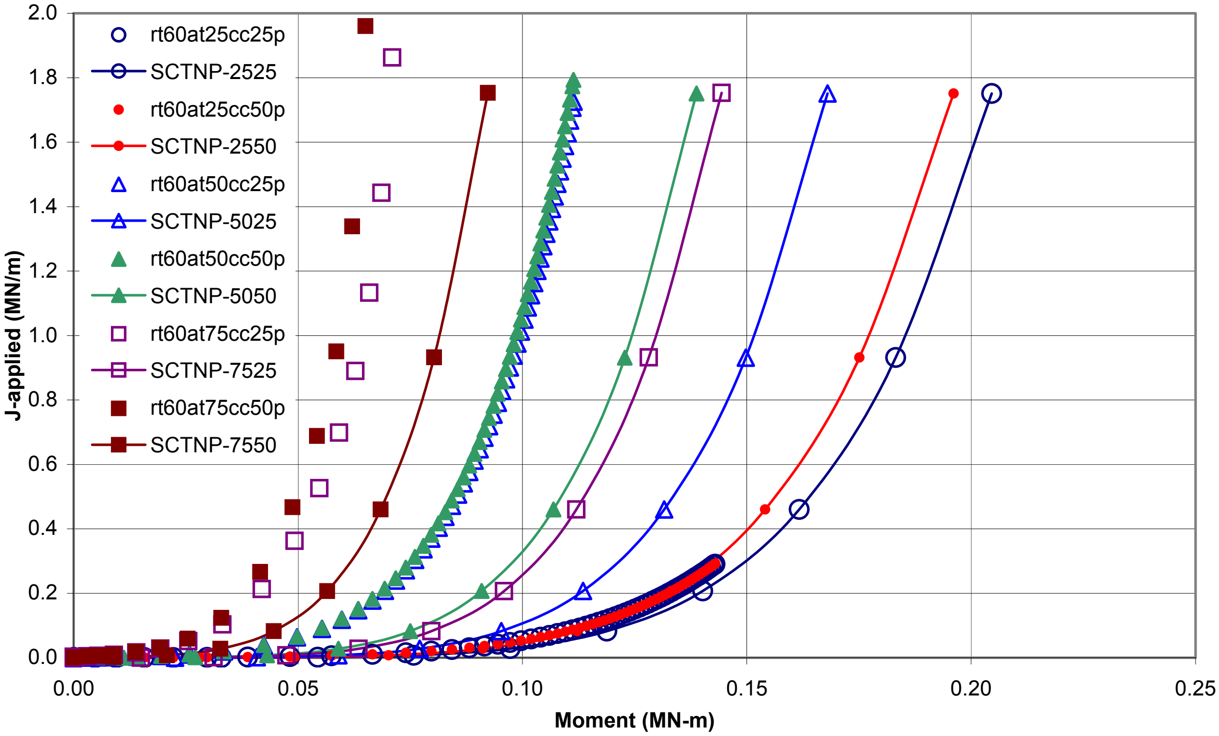

Figure E.17 J versus moment from FEA (symbol) and the SC.TNP1 analysis in NRCPIPES (symbol and line) for Rm/t = 60 and all a/t and θ/π values investigated. (Top) no internal pressure (Bottom) internal pressure (Notation as previously described)

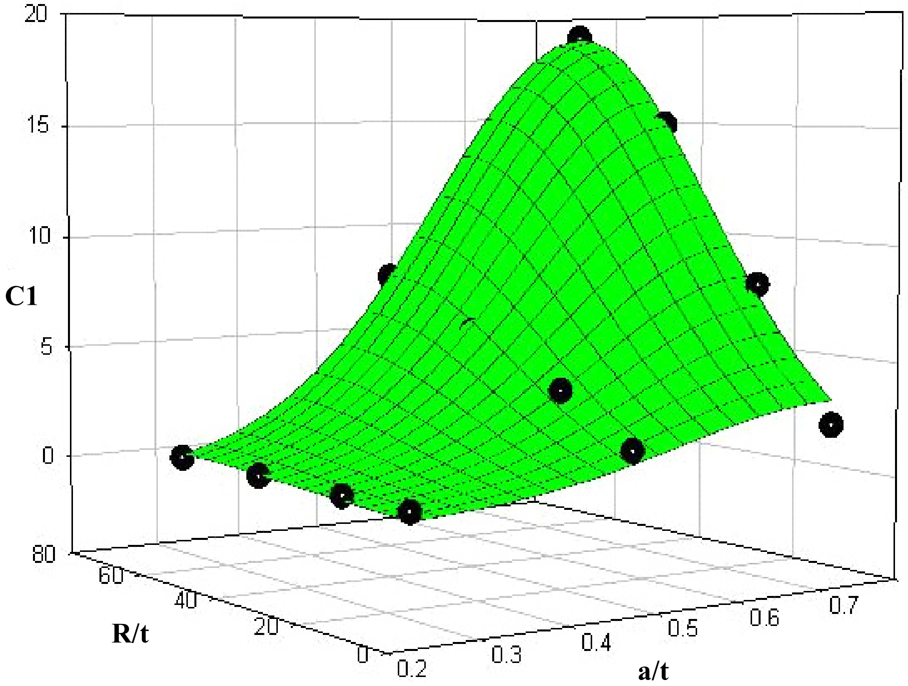

Figure E.18 Length correction coefficient (C1) as a function of Rm/t and a/t for θ/π = 0.25 and no internal pressure

as a function of R_m/t and a/t are shown as circular data points. A Gaussian regression was performed on these points to yield the surface plot shown in Figure E.18. This figure shows that the correction coefficient C1 increases slightly as the crack becomes deeper for the $R_m/t = 5$ case and remains relatively constant at the shallow crack depth $a/t = 0.25$ for the range of R_m/t values analyzed. However, the coefficient increases significantly as both R_m/t and a/t increase.

Figure E.19 shows the plot of C1 as a function of R_m/t and a/t for the cases where the crack length, θ/π, was 0.50 and there was no internal pressure on the pipe. This plot shows that the correction coefficient C1 increases and then decreases as the crack becomes deeper for $R_m/t = 5$ and remains relatively constant at the shallow crack depth $a/t = 0.25$. Again, the coefficient increases as both R_m/t and a/t increase; however, the corresponding increase in the value of C1 is much less for the longer crack length, compared to the results in Figure E.18. The shape of the regression surface suggests that the value of C1, as a function of R_m/t, reaches a maximum at $a/t < 0.75$, as the rate-of-change of C1 decreases at greater crack depths. This trend was not evident in the plot of Figure E.18 for the shorter crack length.

Figure E.20 shows the plot of C1 as a function of Rm/t and a/t for the cases where the crack length, θ/π, was 0.25 and internal pressure was applied to the pipe. The trends are similar to the previous surface plots, with the coefficient C1 increasing as both R_m/t and a/t increase. Also, the value of C1 is relatively constant for the shallow crack ($a/t = 0.25$) at all values of R_m/t and for $R_m/t = 5$ at each crack depth. Likewise, the shape of the regression surface suggests that the value of C1, as a function of R_m/t, reaches a maximum at $a/t < 0.75$, where the rate-of-change of C1 decreases with increasing crack depth.

The last group of results is shown in Figure E.21 for a crack length, θ/π, of 0.50 and internal pressure applied to the pipe. Again, the value of C1 increases as both R_m/t and a/t increase. This plot also suggests a maximum value of C1 occurs at crack depths less than $a/t = 0.75$.

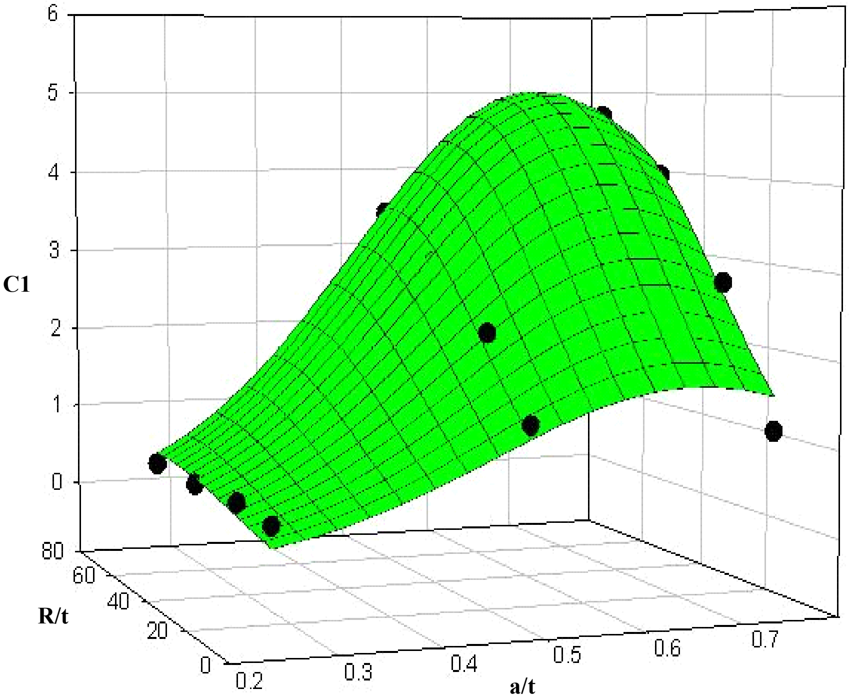

Figure E.19 Length correction coefficient (C1) as a function of Rm/t and a/t for θ/π = 0.50 and no internal pressure

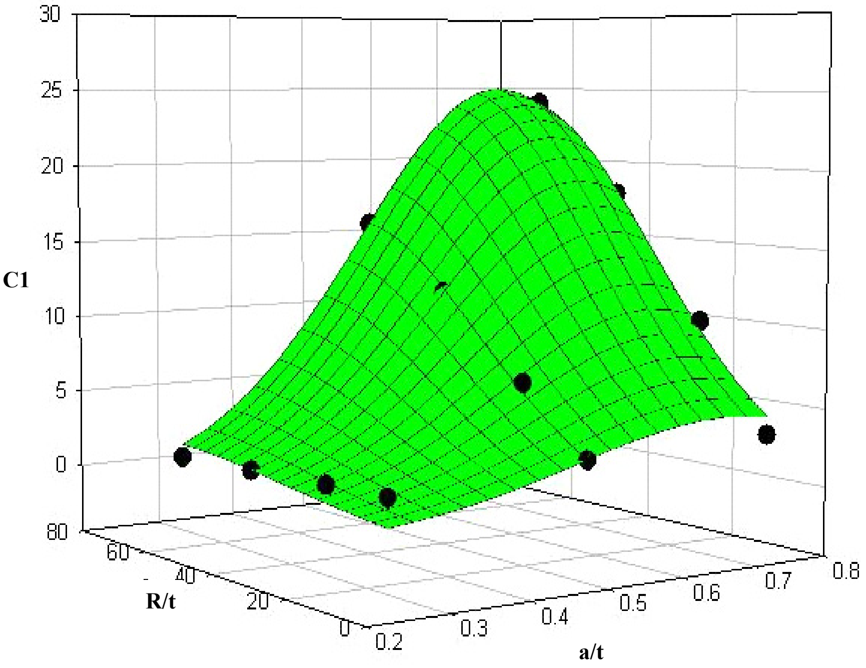

Figure E.20 Length correction coefficient (C1) as a function of Rm/t and a/t for θ/π = 0.25 with internal pressure applied to produce a longitudinal stress equivalent to Sm/2

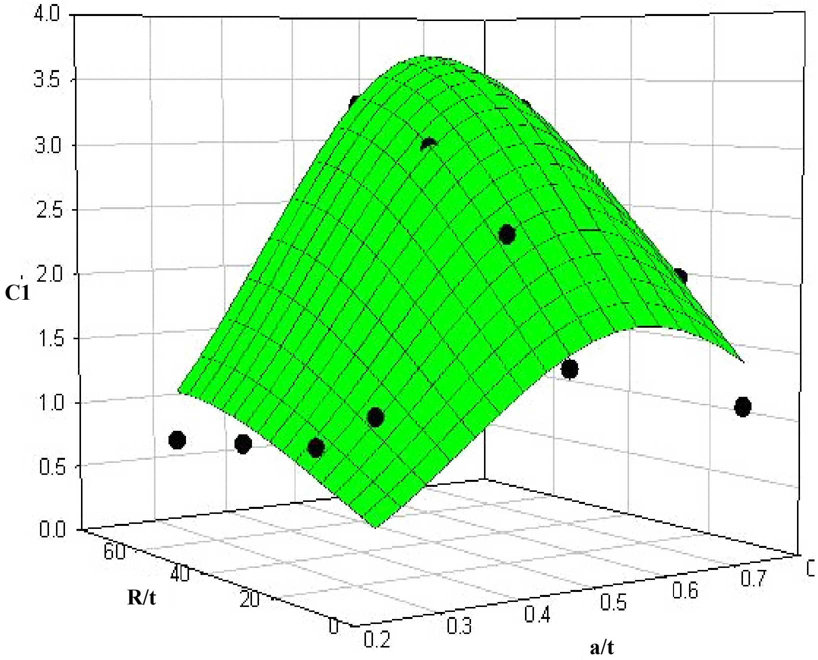

Figure E.21 Length correction coefficient (C1) as a function of Rm/t and a/t for θ/π = 0.50 with internal pressure applied to produce a longitudinal stress equivalent to Sm/2

J Versus Moment as a Function of n - In addition to the previous results, a brief analysis was conducted on the influence of the material strain-hardening exponent on the J versus moment relationship for one pipe geometry. The analysis was conducted using the pipe model with $R_m/t = 5$ and a flaw geometry of $a/t = 0.5$ and $\theta/\pi = 0.50$. There was no internal pressure applied to the pipe. Figure E.22 shows the J versus moment results from both the finite element analyses, the lines with symbols, and the SC.TNP2 analysis in the NRCPIPES code where the Lw term for the SC.TNP2 analysis has been multiplied by a value of C1 that results in an acceptable match (within 10 percent) with the FEA results, lines only. The results indicate a linear increase in the value of the coefficient C1 as a function of increasing strain-hardening exponent between n = 3 and n = 10, see Figure E.23.

E.1.2.6 Discussion - The J versus moment relations from the finite element analyses shown in Figures E.9 thorugh E.12 are typical of those for circumferentially surface-cracked pipe. As expected, the crack-driving force increased as the crack size, length and depth, increased for a given pipe geometry. In addition, the crack-driving force was greater for the pipe and crack geometries that were subjected to internal pressure. As the radius-to-thickness ratio (R_m/t) increased, the crack-driving force also increased, as expected.

The initial analyses of the various *J*-estimation schemes available in NRCPIPES showed that the SC.TNP2 and SC.ENG2 estimation schemes produced conservative results compared with the finite element analysis for $R_m/t = 5$, i.e., the analysis overpredicted the FEA J values. The other schemes produced non-conservative estimations, see Figure E.13a. However, for the higher R_m/t pipe, all of the estimation schemes in NRCPIPES produced non-conservative results for the model with a crack depth of $a/t = 0.5$ and a crack length of $\theta/\pi = 0.25$. (The one exception is that the SC.TKP analyses were very conservative for the R/t = 40 case. This estimation scheme (SC.TKP) is known to have significant problems outside the range for which the influence functions GN were developed, $5 \leq R/t \leq 20$, Ref. E.5). These analyses were

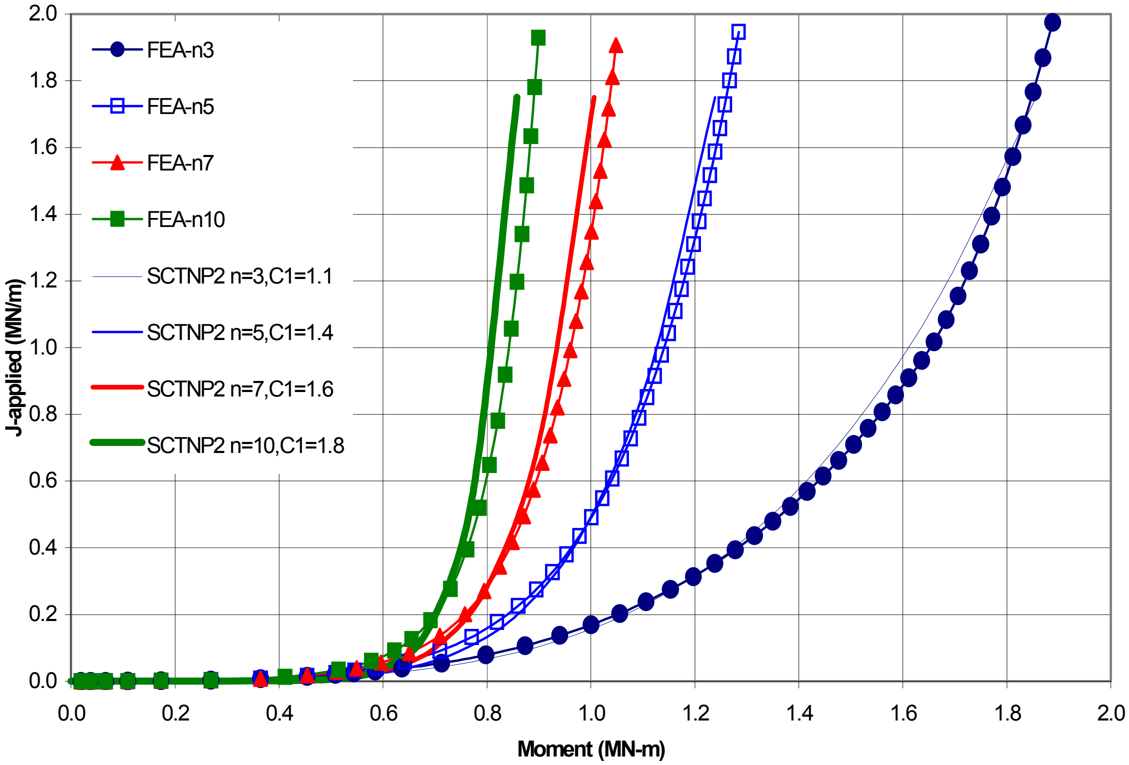

Figure E.22 J versus moment as a function on strain-hardening exponent (n)

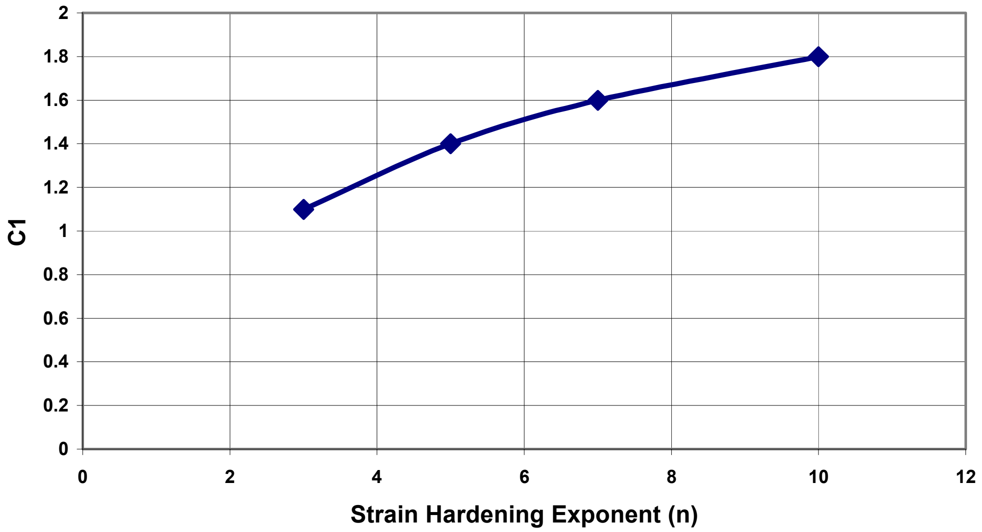

Figure E.23 C1 versus strain hardening exponent (n) relationship conducted for a material with a strain-hardening exponent of 5.

Consequently, the L_W parameter within the SC.TNP method was used to calculate a correction factor for estimating the J versus moment response of higher R_m/t pipe. The L_W input parameter to SC.TNP was calculated as a function of the pipe thickness, t, as L_W = C1*t. For the various pipe and crack geometries, the values of C1 plotted as a function of R_m/t and *a/t* generated the surface plots shown in Figures E.18 through E.21. A Gaussian regression analysis of the surface produced a relationship of the form shown in Equation E.8.

$$C1 = \alpha_1 * \exp^{-0.5*\left[\left(\frac{\frac{a}{t}-x_o}{b}\right)^2+\left(\frac{\frac{R_m}{t}-y_o}{c}\right)^2\right]} \tag{E.8}$$

The results of the regression analyses for the four surfaces shown in Figures E.18 through E.21 are summarized in Table E.3. Note, the coefficients prescribed for Equation E.8 in Table E.3 were developed for the case where the strain hardening exponent (n) was 5. Hence, Equation E.8 using these coefficients is only valid for this case, n=5. Budgetary constraints precluded the development of these coefficients for other values of the strain hardening exponent. However, for most nuclear grade pipe materials, whether they be carbon or stainless steel, the value of n will be close to five such that this limitation was not deemed to be that great.

Within the bounds of the pipe and crack geometry parameters investigated, the coefficient C1 is used to calculate the NRCPIPES reference length input parameter L_W as L_W = C1*t, where t is the thickness of the pipe. The use of this parameter in the SC.TNP estimation scheme has been shown to produce a J versus moment response within ±10 percent of the results from the finite element analysis using the line-spring and shell element model previously described.

Figures E.24 through E.27 show comparisons of the J versus moment results from the revised SC.TNP analysis (Lw = C1*t; closed diamonds in the figures) with FEA results (open diamonds) from Figures E.9 through E.12 for the case of a/t = 0.5, **2/B** = 0.25, no internal pipe pressure, and R/t = 5, 20, 40, and 60, respectively. The same material property data as prescribed in Table E.2 that were used in the development of the FEA results for Figures E.9 through E.12 were used for these SC.TNP analyses. It can been seen from these figures that the revised SC.TNP analysis using the revised reference length parameter (Lw = C1*t) does an excellent job of matching the FEA results for the same test cases for all values of R/t ratio. In fact, the agreement between the SC.TNP results and the FEA results is near perfect at the higher R/t ratios (R/t = 40 and 60). As a check for other cases, a second analysis was conducted for the case of the longer but shallower crack (**2/B** = 0.5 and a/t = 0.25), R/t = 40, and an internal pipe pressure of 3.055 MPa (equivalent to 0.5 S_m). The results of that comparison between the revised SC.TNP analysis and the FEA analysis are shown in Figure E.28. As can be seen from that figure,the agreement is still quite good for this other case.

Table E.3 Surface regression coefficients

Coefficient	θ/π = 0.25 P_i = 0	θ/π = 0.50 P_i = 0	θ/π = 0.25 $P_i = f(S_m)$	θ/π = 0.50 $P_i = f(S_m)$
a_1	18.8942	5.02094	25.1609	3.69173
b	0.193618	0.199894	0.198097	0.231661
c	29.009	36.4407	31.7623	46.5544
x_o	0.752846	0.665584	0.68709	0.60135
y_o	59.2929	58.0279	63.3041	61.7603
R^2	0.9934	0.9841	0.9885	0.9018

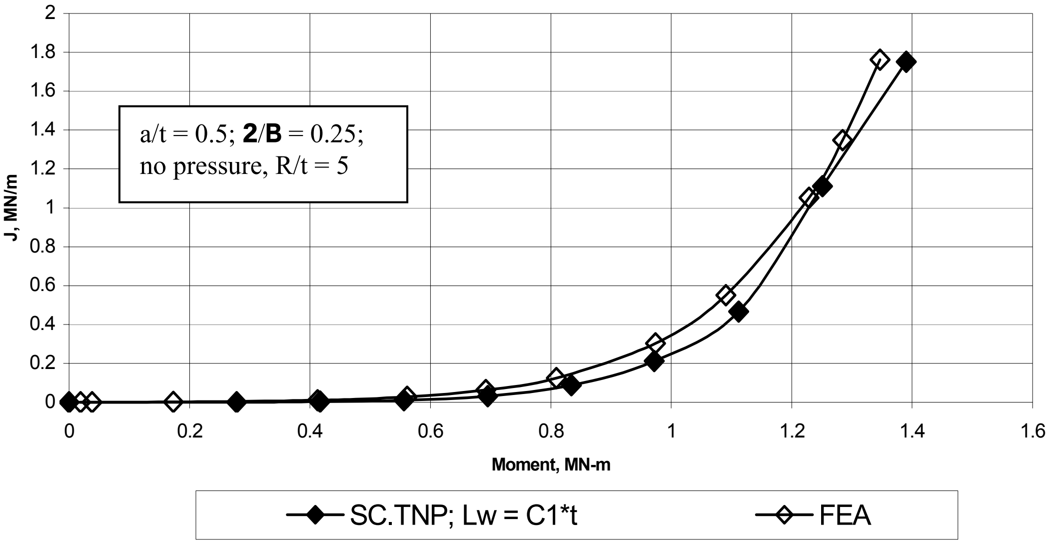

Figure E.24 Comparison of J versus moment response between the revised SC.TNP analysis (Lw = C1*t) and FEA analysis for the case of a/t = 0.5, 2/B = 0.25, no pressure, and R/t = 5

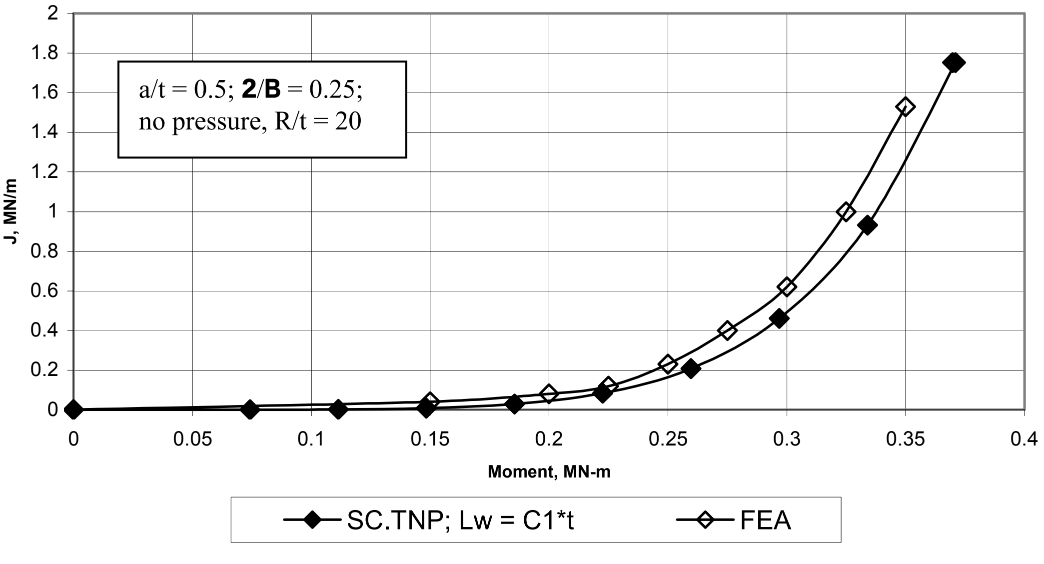

Figure E.25 Comparison of J versus moment response between the revised SC.TNP analysis (Lw = C1*t) and FEA analysis for the case of a/t = 0.5, 2/B = 0.25, no pressure, and R/t = 20

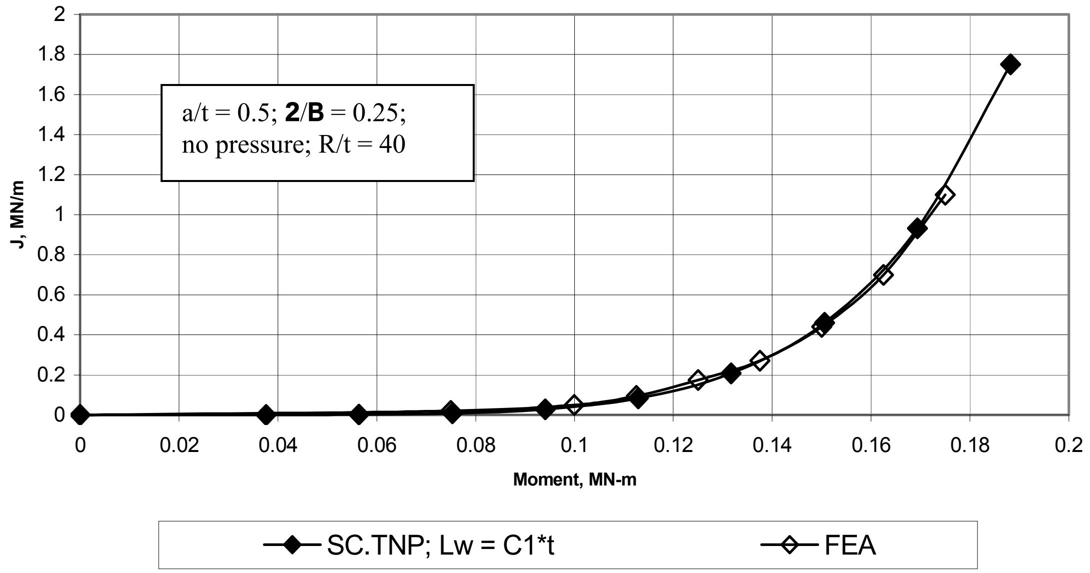

Figure E.26 Comparison of J versus moment response between the revised SC.TNP analysis (Lw = C1*t) and FEA analysis for the case of a/t = 0.5, 2/B = 0.25, no pressure, and R/t = 40

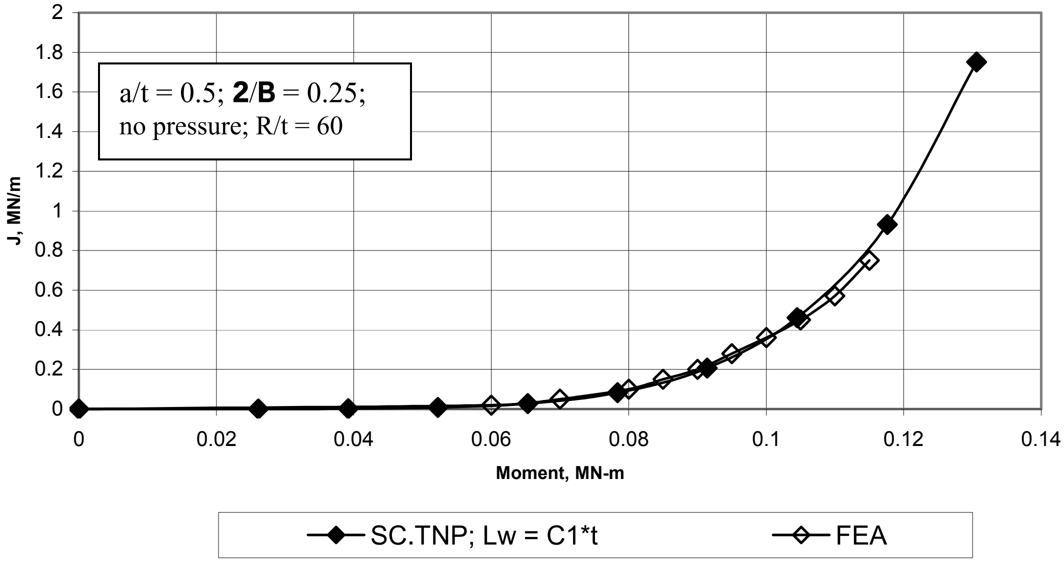

Figure E.27 Comparison of J versus moment response between the revised SC.TNP analysis (Lw = C1*t) and FEA analysis for the case of a/t = 0.5, 2/B = 0.25, no pressure, and R/t = 60

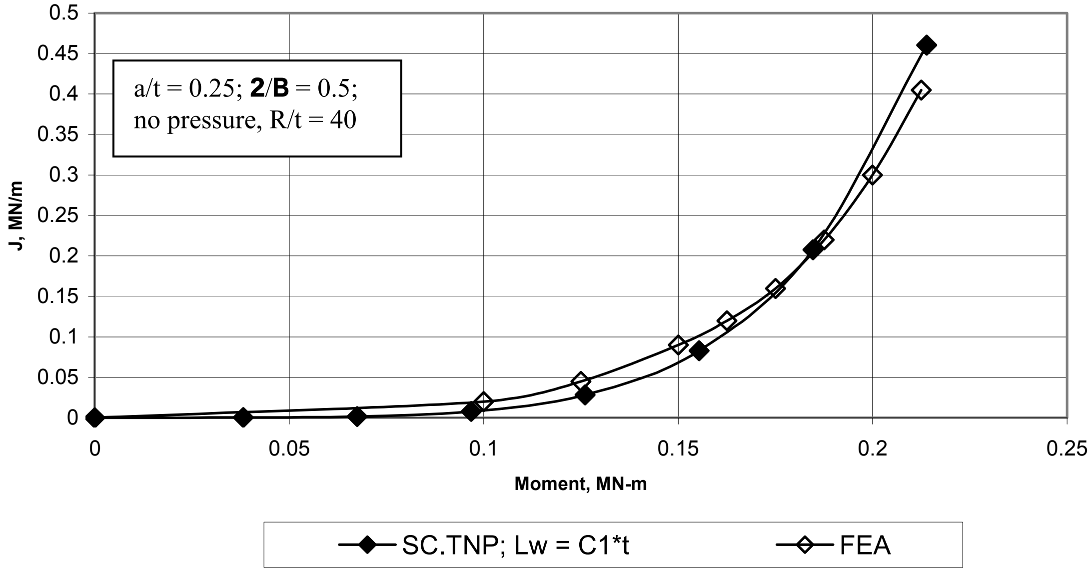

Figure E.28 Comparison of J versus moment response between the revised SC.TNP analysis (Lw = C1*t) and FEA analysis for the case of a/t = 0.25, 2/B = 0.50, pressure = 3.055 MPa, and R/t = 40

Consequently, Equation E.8 could be used in a spreadsheet analysis, where that value could be used in the existing SC.TNP analysis in the NRCPIPES code (Version 3.0). It should be noted that this would produce a more accurate solution for the crack-driving force. The material resistance, however, will be underestimated when using a typical L-C orientated specimen. This would be due to anisotropy and constraint issues, which are not addressed in this report. The anisotropy and constraint aspects could cause the actual surface-cracked pipe fracture resistance to increase by a factor of 3 to 5.

Finally, it should also be noted that there is evidence from the large strain analysis of Miura (see the results for the Second Round Robin in Appendix I), that for cases where $R_m/t = 40$ or greater there may be localized buckling that was not captured by the small-strain analyses required to be used with line-spring elements. The localized buckling gives lower failure loads; hence, this estimation procedure may overestimate the maximum loads in those cases. The precise limits on this estimation procedure have not been explored in this work.

E.1.3 Effect of R/t Ratio on Limit-Load Analyses

As part of the Degraded Piping (Ref. E.10) and Short Cracks (Ref. E.7) programs it was found that the pipe R/t ratio had an effect on the load-carrying capacity of surface cracked pipe that failed under limit-load conditions, see Figure E.29. As can be seen in this figure, for relatively small diameter (6- to 16-inch diameter) pipe experiments with surface cracks in the base metal of relatively high toughness stainless steel pipes which should have failed under limit-load conditions, the ratio of maximum experimental stress to the Net-Section-Collapse (Ref. E.11) decreased as the pipe R/t ratio increased. This was attributed to ovalization effects as the pipes ovalized during bending such that the effective moment of inertia (i.e., bending resistance) decreased more for the thinner pipes tested.

The experimental data available from References E.10 and E.7 are limited to R/t ratios less than 20. For Class 2, 3, and Balance of Plant piping, the R/t ratios may be significantly

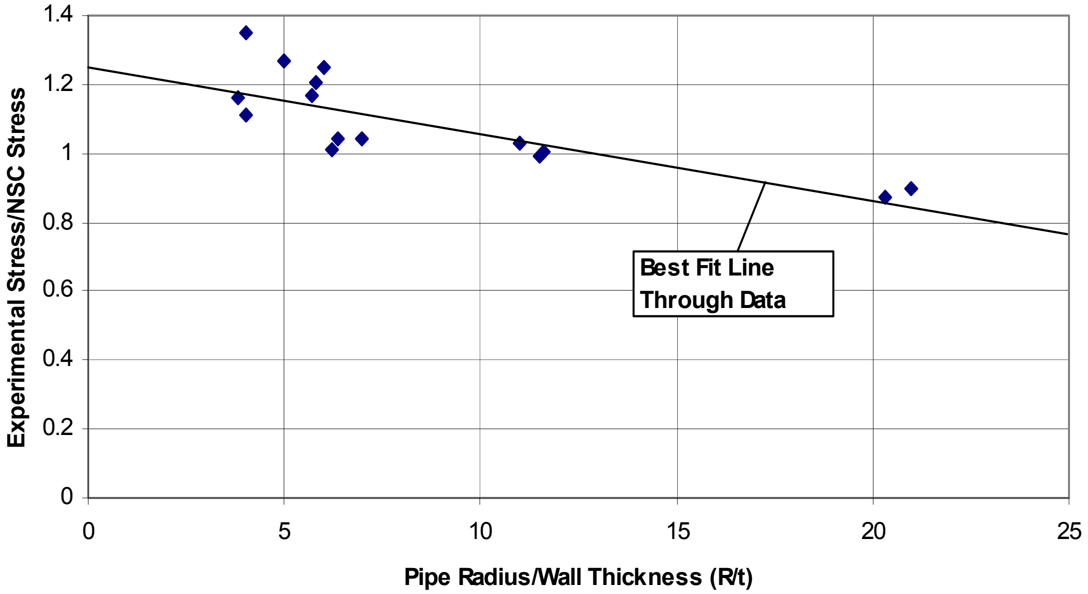

Figure E.29 Plot of the ratio of the experimental stress to the predicted stress as a function of pipe R/t ratio for pipes expected to fail under limit-load conditions

greater than 20. As such one of the original objectives of this overall effort was to develop additional experimental data for the case where the R/t ratio approached 40 to 50. However, during the course of this program it was decided to eliminate the proposed effort from the work scope due to the limited resources available. The cost to conduct the single experiment proposed was deemed to be prohibitive in light of the available funding available.

E.2 Effect of Lower Operating Temperatures for Class 2, 3, and BOP Piping on the Transition Temperature Behavior of Ferritic Pipes

The ASME Section XI pipe flaw evaluation criteria only apply to Class 1 piping. There is a desire in the industry to expand the Code procedures to Class 2, Class 3, and balance-of-plant (BOP) piping. Most of this piping is ferritic material. Oftentimes these pipes operate at lower temperatures. The current Appendix H ferritic pipe flaw evaluation procedures in Section XI of the ASME Boiler and Pressure Vessel Code currently requires that for pipe operating below 93ºC (200ºF), the use of a linear elastic fracture toughness value of J_{Ic} = 45 in-lb/in^2 (K_{Ic} = 35.5 ksi√in) be used, Ref. E.12. This toughness is equivalent to lower-shelf brittle fracture toughness behavior. Hence, a key question to be addressed is to determine if ferritic pipe with a surface crack actually exhibits brittle fracture initiation behavior at lower operating temperatures. If upper-shelf behavior for the start of ductile tearing can be demonstrated for all commonly used nuclear ferritic piping steels, then the flaw assessment rules can be simplified, and there will be larger flaw size tolerances. This work could lead to a simplified method to assess if upper-shelf flaw assessment rules can be extended to Class 2/3/BOP piping at lower operating temperatures.

The objective of this effort was to develop an initial procedure to assess the lowest temperature that ductile fracture initiation behavior might be expected for a surface crack in ferritic nuclear grade pipe. This involves a methodology to account for constraint effects on the ductile fracture initiation temperature and relating that back to Charpy impact data for typical ferritic pipe materials. This draft procedure could then be the basis for future validation tests. If found to be reasonable, then this procedure could be used in the ASME pipe flaw evaluation procedures as a screening criterion to determine if LEFM or EPFM fracture will occur.

E.2.1 General Methodology

There are two main differences between Class 1 and Class 2/3/BOP piping. As previously discussed, Class 2/3/BOP piping has a higher ratio of pipe diameter-to-thickness than Class 1 pipe. Therefore, new F-functions and elastic-plastic fracture mechanics (EPFM) solutions are needed. (See prior discussions earlier in this appendix.) Also, Class 2/3/BOP piping operates at lower temperatures. Past results, primarily from the oil and gas industries, show that the constraint effects of surface cracks in ferritic pipe under global bending or pressure loading may result in a significantly lower brittle-to-ductile transition temperature than for a through-wall crack in the pipe or from standard C(T) or Charpy tests results.

There are three optional approaches that can be taken to determine the lowest temperature where ductile fracture occurs. These are;

- Option 1- Use a specimen that closely simulates the constraint conditions and anisotropy that exists for the surface crack in a pipe. As will be shown later, it is believed a fixed-grip single-edge-notched tension (SENT) test with the crack growing in the radial direction, i.e., L-R orientation for a circumferential surface crack and C-R direction for an axial surface crack, has the same constraint conditions as a surface-cracked pipe. Although there are some test data to support this approach, validating pipe tests should be conducted.

- Option 2 - Use standard C(T) specimen test data with a correction for constraint effects on transition temperature and upper-shelf toughness, or

- Option 3 - Use Charpy energy or shear area percent curves with temperature shifts to account for dynamic loading, thickness effects, and constraint effects to estimate the lowest temperature where ductile fracture initiation will still occur. If only a few Charpy test data points exist, then a procedure for estimating the entire Charpy transition curve needs to be used.

In many cases, the available data for Class 2/3/BOP piping will at best consist of Charpy impact energy and percent shear area values at a specified temperature such as 0ºC (32ºF), 10ºC (50ºF), or room temperature. Seldom is there a full Charpy transition curve, so that a procedure is needed to estimate the full Charpy curve from a few data points. Option 3 is the mostly likely method to be used.

Another approach based on the use of Option 3 procedure is to assess from a database of Charpy energy versus temperature curves what is the reasonable bound Charpy energy/shear area percent curves for a class of ferritic pipe steels. The lowest temperature for ductile fracture initiation for that class of steels can then be estimated. (This temperature will shift with the thickness of the pipe.) If that lower-bound temperature were less than the lowest temperature that the plant could operate at, then one would anticipate that that class of steels would always initiate in a ductile manner. This might provide a simple screening criterion to determine if LEFM or EPFM fracture is anticipated, and would be very useful for ASME or other Code applications.

The Option 3 procedure was the focus of this effort. The details of this procedure involve the following steps. Much of this methodology comes from older gas pipeline work and, as such, may be new terms that are not familiar to engineers dealing with nuclear piping.
Table E.4 also gives a summary of the new terms and definitions to be used throughout this report.

1. Use Charpy V-notch impact specimen data to determine the transition temperature corresponding to an 85 percent shear area (Tc).

Table E.4 Definition and equivalence of different transition temperature fracture parameters

Fracture Parameter	Definition	Equivalent to	Related to
Fracture initiation transition temperature (FITT$_{(SC)}$) of surface-cracked pipe under quasi-static loading.	Lowest temperature for ductile fracture initiation of a surface-cracked pipe (axial or circumferential flaw) under quasi-static loading.	Believed to be equivalent to transition temperature of fixed-grip SENT specimen (L-R orientation for circumferential crack and C-R orientation for axial crack) under quasi-static loading	Figure E.40a shows surface crack to through-wall crack FITT differences.
Fracture initiation transition temperature (FITT$_{(TWC)}$) of a through-wall-cracked (TWC) pipe under quasi-static loading.	Lowest temperature for ductile fracture initiation of a TWC in a pipe (axial or circumferential flaw) under quasi-static loading.	Transition temperature of bend-bar or C(T) specimen. (L-C orientation for circumferential TWC and C-L orientation for axial TWC)	From full-scale ferritic pipe test data, FITT$_{(TWC)}$ is 33 to 50ºC lower than FPTT.
Fracture propagation transition temperature (FPTT) of through-wall-cracked pipe	Lowest temperature where a dynamically propagating through-wall crack is ductile.	Experimentally shown to be equal to 85% shear area transition temperature of full-thickness DWTT specimen.	Related to Charpy 85% transition temperature as a function of the pipe thickness (validated for lower yield strength line-pipe steels and nuclear grade ferritic pipe).
Charpy V-notch impact transition temperature (T_c)	85% transition temperature of standard Charpy specimen.	Can also examine energy versus temperature curve if shear area percent not rated. (Not valid to use energy transition temperature for materials that have energy changes on upper shelf).	Can be determined by knowing the temperature and shear area percent of a few specimens. Correlations for other thickness Charpy specimens exist.

2. Relate the Charpy transition temperature (Tc) to the full-thickness transition temperature for dynamic fracture. This corresponds to a term called the fracture propagation transition temperature (FPTT). For gas pipelines steels, this is commonly determined from the drop-weight tear test (DWTT), Ref. E.13, where the temperature corresponding to 85 percent shear area in the DWTT is equal to the FPTT. There are correlations between the Charpy and the DWTT 85 percent shear area transition temperatures.

3. Relate the FPTT to the fracture initiation transition temperature (FITT) for a through-wall crack (TWC) in the pipe. The difference between the FITT and FPTT comes from fracture behavior of ferritic steels being sensitive to strain rate.

4. Relate the FITT for a through-wall crack to the FITT for a surface crack (SC). Constraint effects shift the fracture initiation transition temperature as a function of surface-crack depth.

5. The resulting FITT for a surface crack in a pipe corresponds to the lowest temperature where ductile fracture behavior will occur under quasi-static loading and can be calculated by knowing the upper-shelf toughness.

The technical background for these steps in the Option 3 procedure is given below. Following that, each step of the methodology is described along with an example calculation. An example of the estimated lowest operating temperature for ductile fracture initiation that is expected for A106B pipe is given.

E.2.2 Technical Background

The methodology developed for the Option 3 approach uses some terms not frequently used in the nuclear industry, but are familiar in the oil and gas industry, hence this background is described in detail. The Option 3 approach starts off by using the Charpy impact specimen data for the pipe material as the initial input. Through a series of adjustments to account for loading rate, thickness, and constraint effects; the approximate fracture initiation transition temperature (FITT) is determined for a piping material with a surface crack. The FITT is the lowest temperature where ductile fracture is expected to occur, so that the failure stress of the flawed pipe remains relatively constant at higher temperatures (not accounting for strength or upper-shelf toughness changes with increasing temperature). The methodology is the same for an axial or circumferential surface crack.

First of all, the general approach is to relate the dynamic transition temperature for crack behavior from Charpy impact tests to the minimum temperature for quasi-static ductile fracture initiation for a surface-cracked pipe. The minimum temperature where a through-wall crack might propagate as a ductile fracture was termed the fracture propagation transition temperature (FPTT) in the oil and gas industry back in the 1950's. It was highly desired not to have long-running brittle fractures in gas pipelines, of which there were some early cases of brittle fractures of 5 to 15 kilometers in length. Full-scale tests showed that the standard thickness Charpy test was not sufficient to determine the FPTT. Consequently, a full-thickness impact test called the drop-weight tear test, DWTT, (Ref. E.13) was developed. Note that the DWTT is not the same as the drop-weight test (Ref. E.14) used in reactor pressure vessel surveillance work. A drop-weight-tear test (DWTT) specimen is shown in Figure E.30 along with a Charpy specimen in the C-L orientation (through-wall axial crack growth direction). Figure E.31 shows the comparison of shear area percent values from 99 full-scale pipe burst tests and 37 DWTT, Ref. E.15. The gas pipeline industry typically stipulates that when the DWTT specimens had 85-percent shear area or more, then in the full-scale test the material was fully ductile (100% shear area) for a dynamic propagating crack. This 85-percent shear area transition temperature (85% SATT) is therefore equal to the FPTT, or the minimum temperature where an unstable growing crack will be ductile.

In the case that DWTT data does not exist, empirical equations between the Charpy test and the DWTT test can be used. It is assumed here that for ferritic nuclear piping steels there are no DWTT data, so that these correlations need to be used. From past testing results, it has been determined that the FPTT will vary to the square root of the thickness of the material, Ref. E.16. This is shown in Figure E.32 and Figure E.33 for gas linepipe steels having similar strength, chemistry, and fabrication histories to nuclear ferritic pipes.

The next step is to account for the strain-rate effect on the transition temperature shift between a propagating through-wall crack (FPTT) and the initiation of a through-wall crack (fracture initiation transition temperature or FITT(TWC)). Experimental data from ferritic linepipe steels with comparable strengths to nuclear ferritic pipe steels show that there is a shift in the dynamic to quasi-static transition temperature of about 33ºC to 50ºC (60°F to 90ºF), see results in Figure E.34 and Figure E.35 from Kiefner (Ref. E.17). These figures show the results from full-scale axial through-wall-cracked pipe burst tests (keeping the flaw size constant), and DWTT test results. To put them on a common plot, the upper-shelf burst pressure for the pipe tests was normalized to 100 percent, and when the DWTT specimen had 100 percent shear area that was 100 percent ductile failure. The FITT(TWC) occurs when the pipe failure pressure just started to drop from the upper-shelf value. The shift in temperature between the FITT(TWC) and FPTT then is due to the strain-rate effects. (Again note that the FPTT coincides with the 85 percent shear-area transition temperature of the DWTT specimen.)

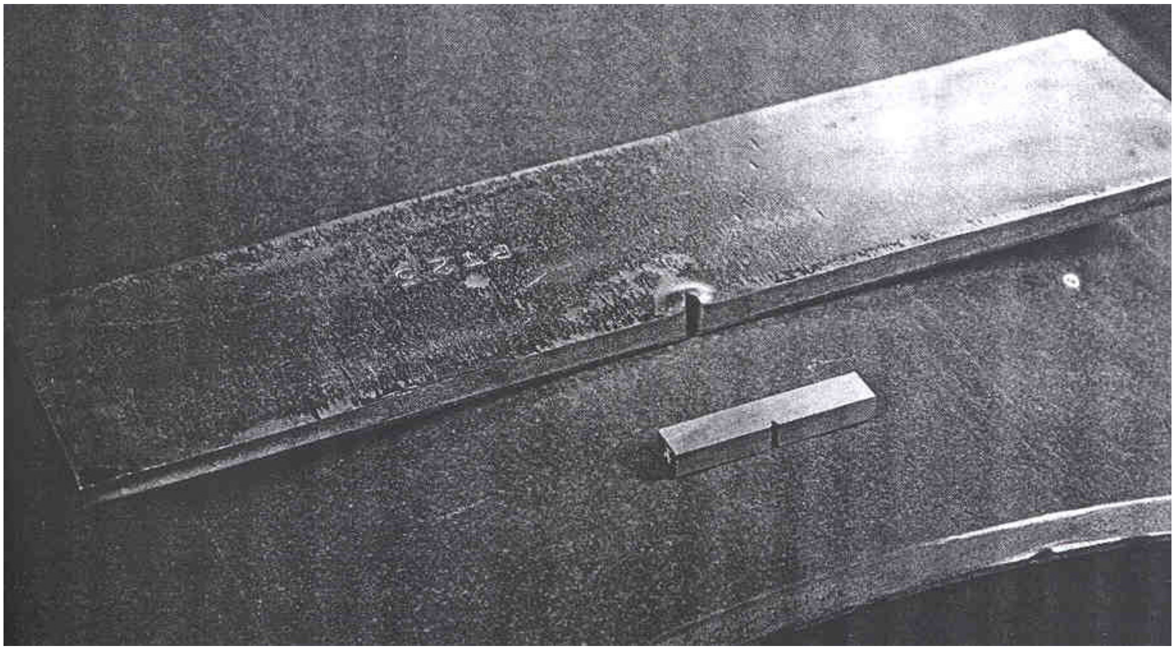

Figure E.30 Photo showing a Charpy and full-thickness DWTT specimens on a pipe

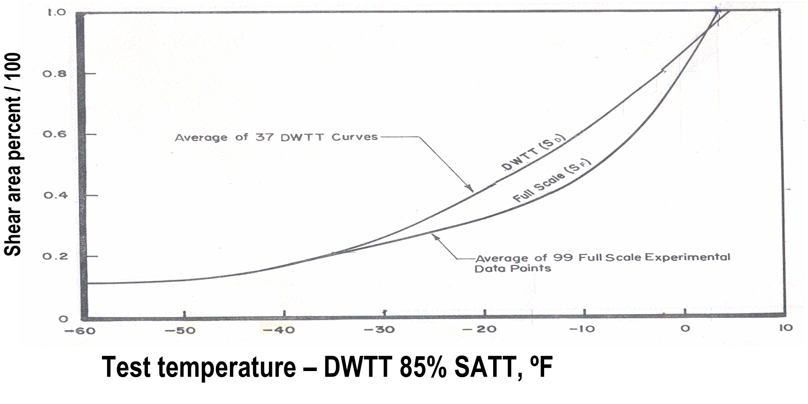

Figure E.31 Comparison of fracture appearances (percentage of shear area on the fracture) from full-scale dynamic crack propagation results to impact results from the DWTT

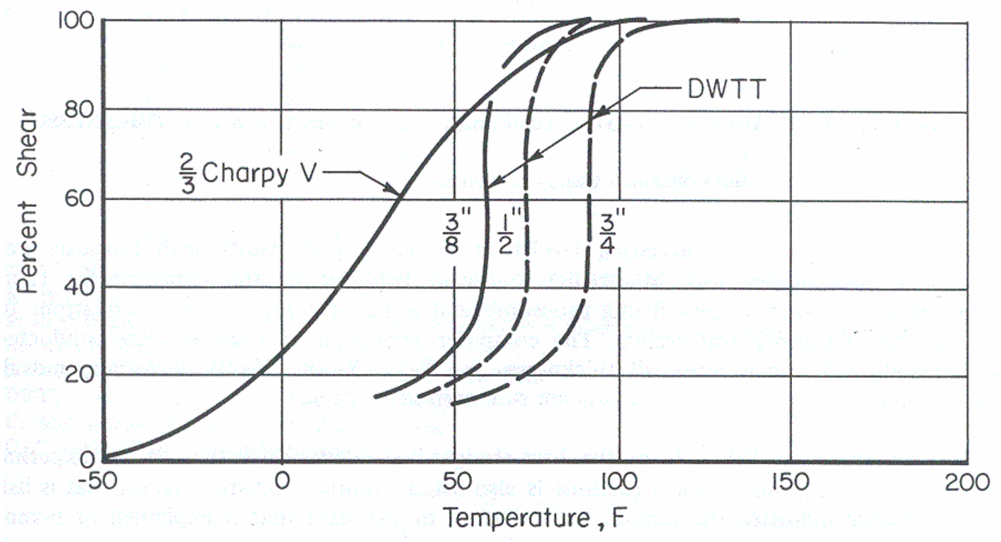

Figure E.32 Results showing the transition curve differences between a 2/3-thickness Charpy specimen and DWTT specimens of different thicknesses from the same material

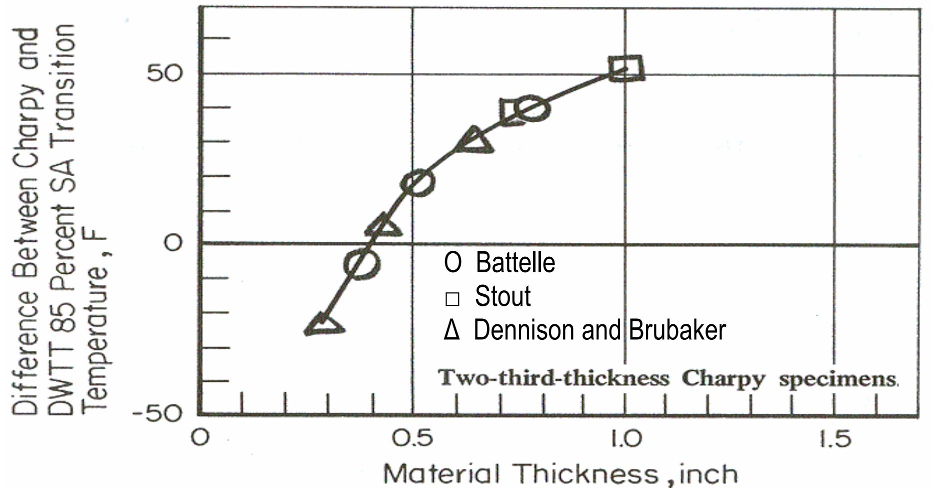

Figure E.33 Experimental results from several investigators showing the effect of thickness on the difference between the Charpy and DWTT 85% SATT, Ref. E.16

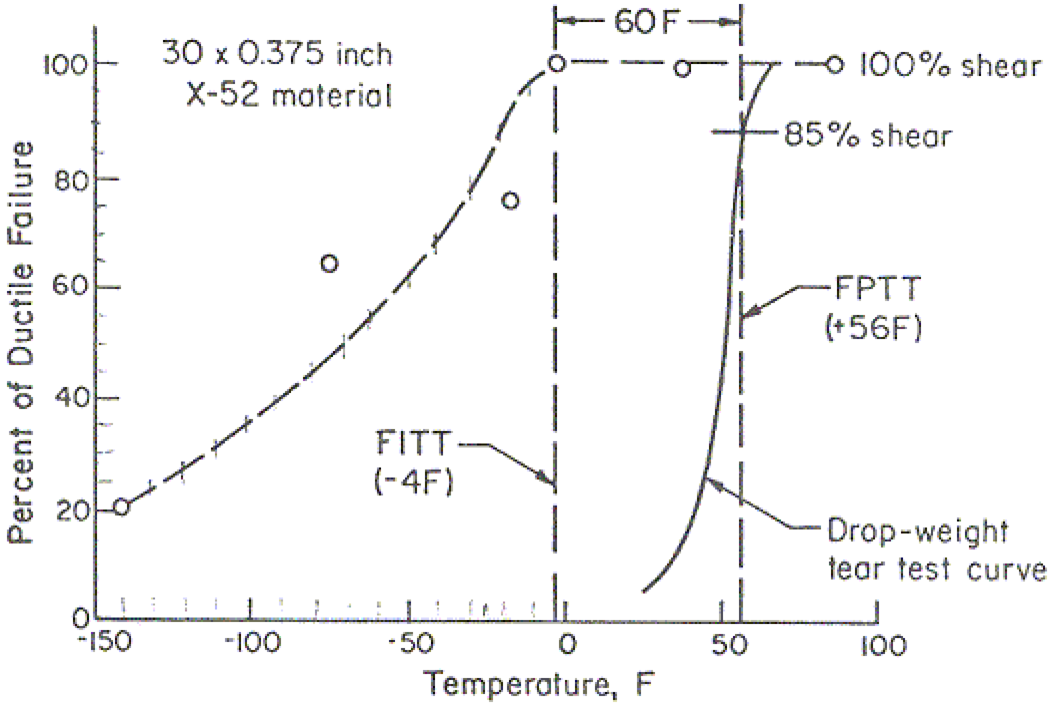

Figure E.34 Axial through-wall-cracked pipe and DWTT data showing the temperature shift from the FITT to the FPTT for linepipe steel – Case 1, Ref. E.17

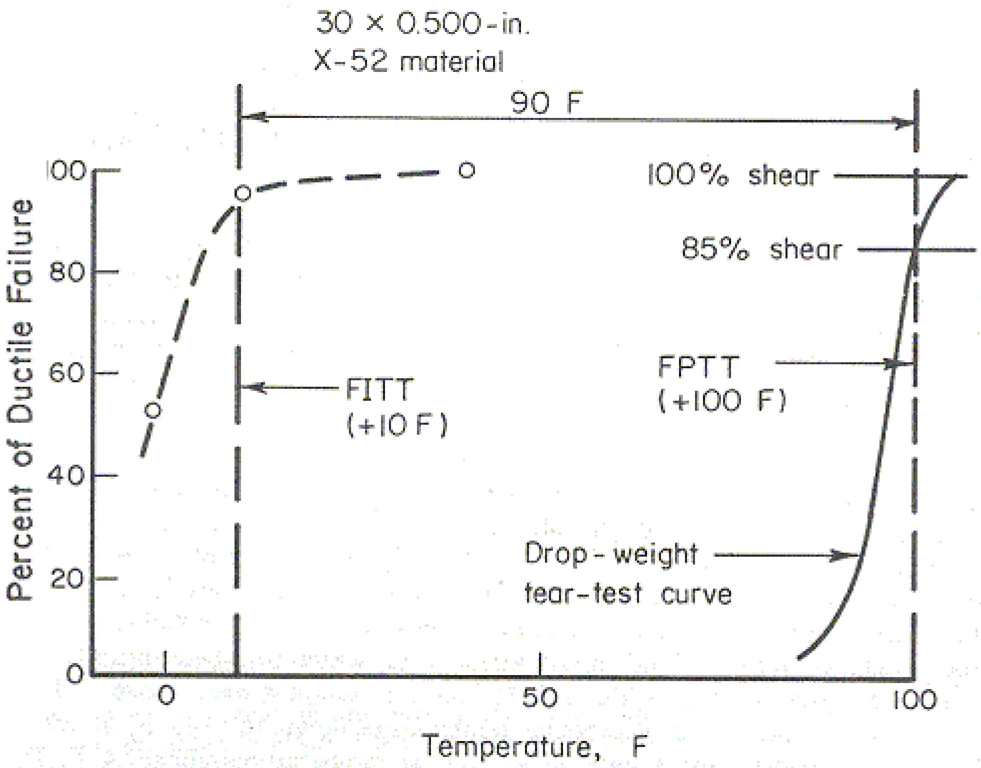

Figure E.35 Axial through-wall-cracked pipe and DWTT data showing the temperature shift from the $FITT_{(TWC)}$ to the FPTT for linepipe steel – Case 2, Ref. E.17

In the event that actual quasi-static fracture toughness data is available for the material of interest, the $\mathrm{FITT}_{(TWC)}$ can directly be determined from C(T) or bend-bar specimen tests at various temperatures. Figure E.36 shows the comparison of bend-bar specimen transition temperature and full-scale axial through-wall-cracked pipe test results, Ref. E.18. Note that for the through-wall crack, the bend-bar gave the same FITT as the pipe tests. Since bend-bar and C(T) specimens have similar constraint conditions, either should give the FITT for a through-wall-cracked pipe.

The next step is to account for the difference in the transition temperature from a through-wall initiating crack to the initiation of a surface crack, i.e., determine the surface-cracked-pipe FITT ($\mathrm{FITT}_{(SC)}$). This difference occurs due to constraint effects at the crack tip. The bend-bar and C(T) specimens have a large degree of bending which increases the triaxial stresses at the crack tip. On the other hand, the surface crack has mainly membrane loading in the ligament giving lower triaxial stresses and constraint at the crack tip. The higher triaxial stresses will trigger cleavage failure earlier. This can somewhat be seen from data by Kiefner in comparing the FPTT from the DWTT to the surface-cracked pipe FITT results. In Figure E.37, Kiefner showed this difference was greater than 75°C (136ºF), which was more than for the through-wall-cracked pipe results in Figure E.34 and Figure E.35.

Additional pipe test data are available from Sugie (Ref. E.19) or base metal Grade B pipe with surface cracks having an a/t of 0.5 with a machined V-notch. In this case, Sugie had CTOD bend-bar specimen results that normally would give the through-wall-crack fracture initiation transition temperature. From these surface-cracked pipe tests, a shift in the FITT from the through-wall crack to the surface crack was observed to be from 40ºC (72ºF) to more than 95ºC (171ºF), see Figure E.38. Hence, these full-scale pipe test results showed a significant shift in the brittle-to-ductile transition temperature for fracture initiation between a through-wall crack and a surface crack.

To further explore the surface-crack to through-wall-crack FITT differences, Wilkowski conducted a program for the American Gas Association's (A.G.A.) Welding Supervisory Committee, Ref. E.20. In this program, it was postulated that a fixed-grip SEN(T) specimen with the crack in the L-R orientation would simulate anisotropic and constraint effects that a surface crack in a pipe would experience. A schematic of this specimen is shown in Figure E.39. Later in Reference E.21, this same specimen was further optimized for testing so that there was a straight fatigue crack produced with the use of blunt side grooves and a scalloped notch, see photo in Figure E.39.

In the initial A.G.A. work by Wilkowski, three different ferritic linepipe materials were tested that had a combination of two thickness and two strengths. The initial program used a double-clip gage method to determine the CTOD values, along with d-c electric potential data to determine the point of crack initiation. In addition to the L-R SEN(T) specimens meant to simulate surface-crack constraint conditions, t by 2t COD bend-bar specimens in the L-C orientation were also tested. This orientation is for a through-wall crack growing around the circumference, and based on past experimental results should represent the constraint condition similar to a through-wall crack in the pipe (Ref. E.18).

The bend-bar CTOD values at crack initiation were determined using the d-c electric potential method and standard procedures to calculate the CTOD values from a crack-mouth-opening displacement measurement. Hence, the difference in the bend-bar and SEN(T) specimens were expected to be similar to the differences between a through-wall crack and a surface crack in a pipe. Since tests were conducted at various temperatures, the comparisons in Figure E.40a show the differences in the fracture initiation transition temperatures (FITT) of the surface crack relative to the through-wall crack. Figure E.40b shows the differences in the upper-shelf toughness values. The differences in the upper-shelf toughness values may be due to a combination of constraint and anisotropy of the ferritic steel used, whereas the transition temperature effects are not affected by anisotropy. This assumption that the transition temperature is

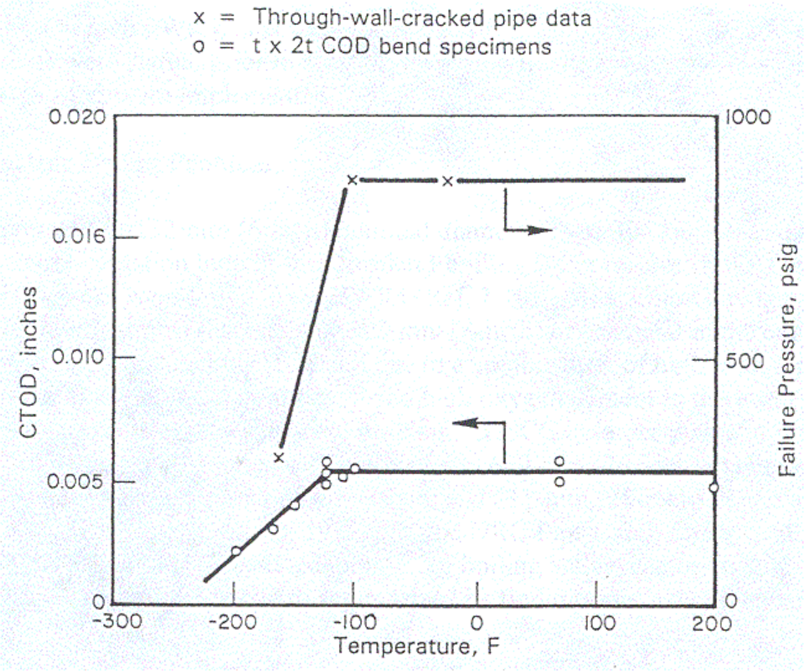

Figure E.36 Comparison of t x 2t CTOD transition temperature with axial through-wall-cracked 48-inch (1,219-mm) diameter pipe fracture data, Ref. E.18

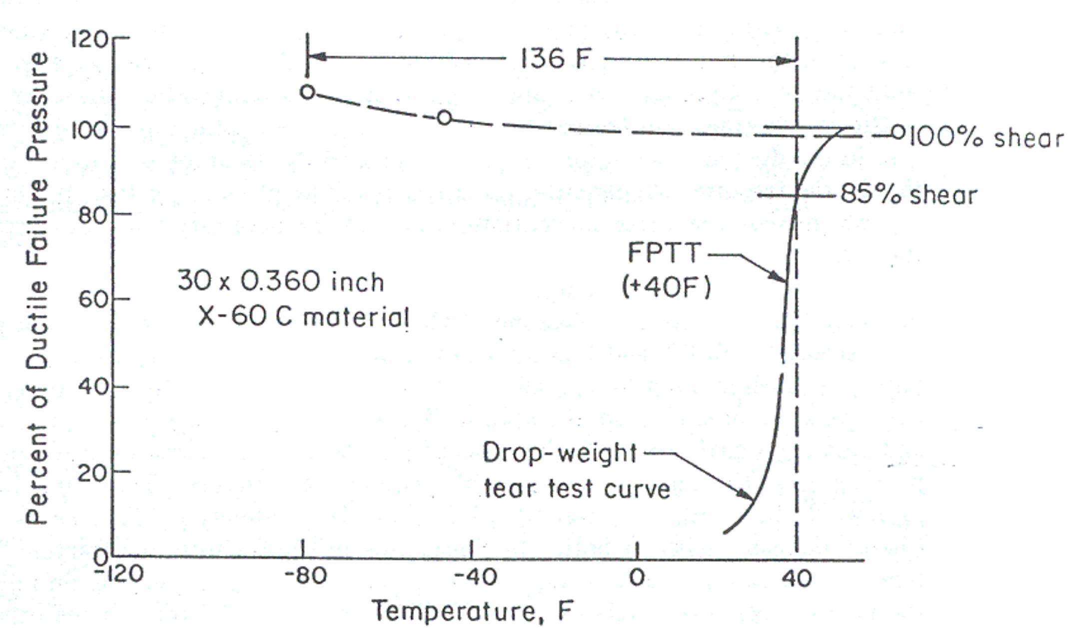

Figure E.37 Results from Kiefner showing surface-flawed pipe results relative to FPTT from DWTT data, Ref. E.17

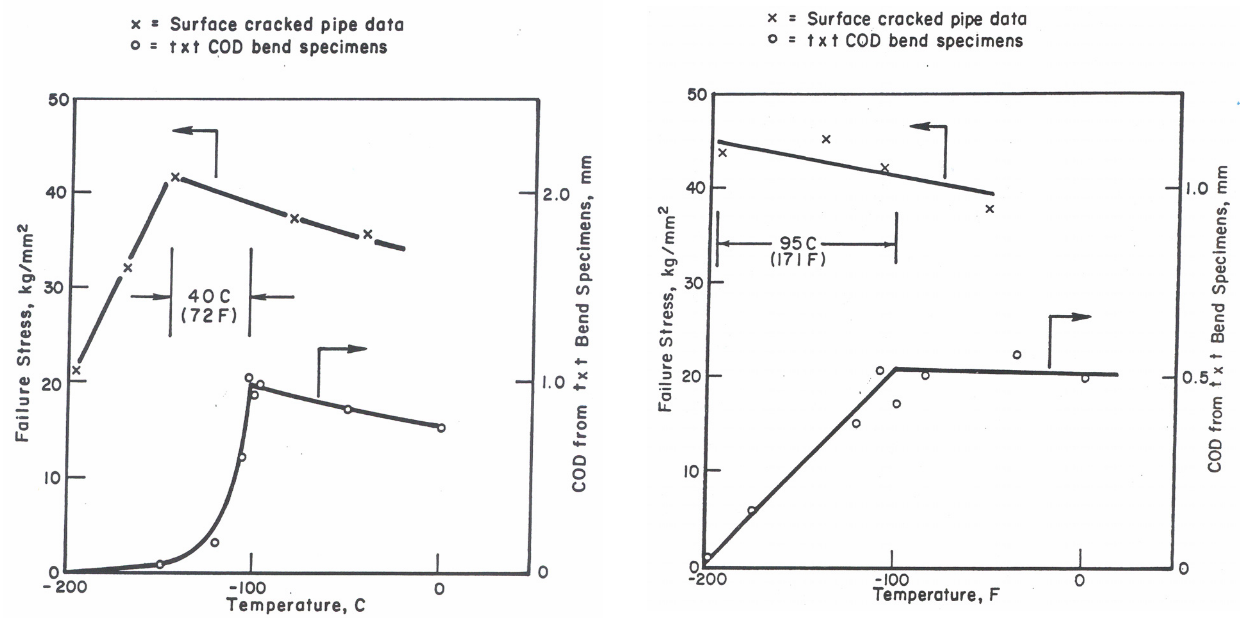

Figure E.38 Results from Sugie showing surface-flawed pipe results relative to bend-bar FITT, Ref. E.19

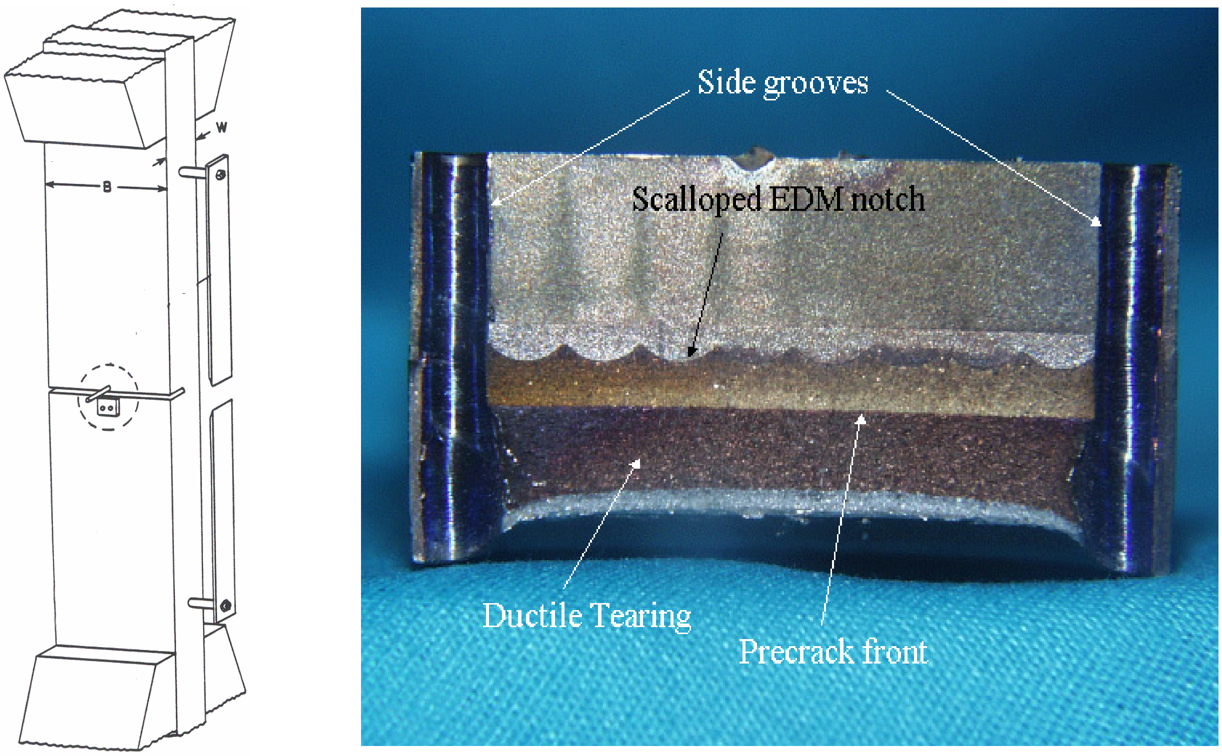

Figure E.39 Fixed-grip SEN(T) specimen
(Side-grooves in photo not illustrated in sketch)

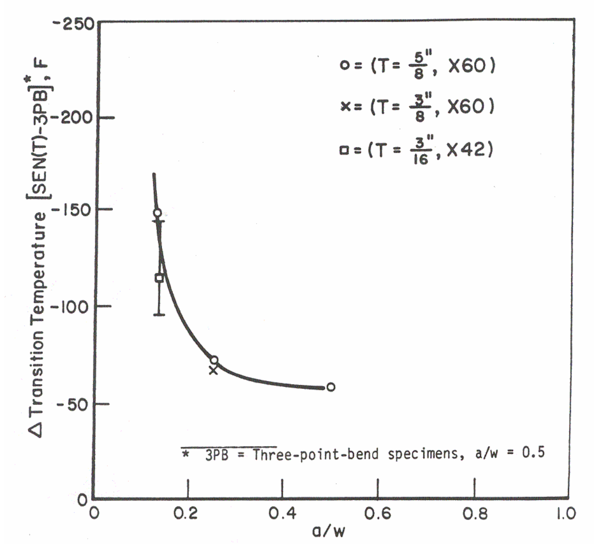

(a) Transition temperature shifts

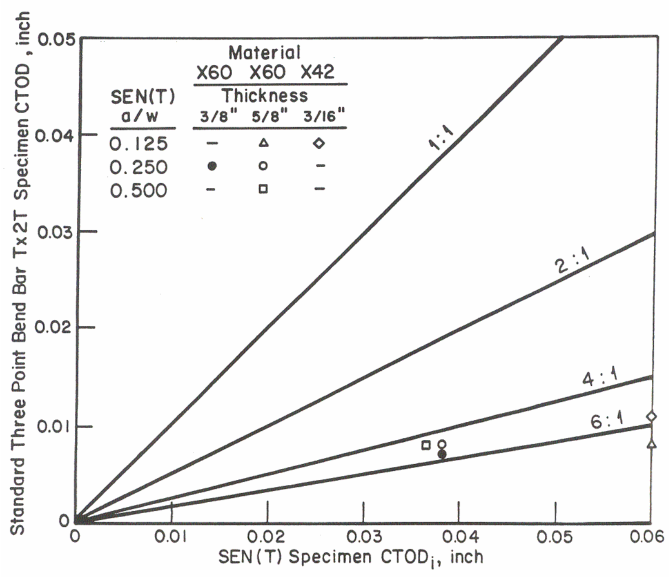

(b) Upper shelf CTOD values

Figure E.40 Results from Ref. E.20 in comparing transition temperatures of bend-bar specimens and fixed-grip SEN(T) specimen

not significantly affected by the anisotropy is illustrated in Figure E.41 (obtained from WRC Bulletin 175, Ref. E.22). This figure shows Charpy specimens in different orientation had different absorbed energies, but the brittle-to-ductile transition temperatures were about the same.

Figure E.40a therefore is expected to provide an initial estimate of the trends of the difference in the FITT for a surface crack versus the through-wall crack. Also knowing that:

1. the FITT to FPTT transition temperature is estimated to be 33 to 50ºC based on the results in Figure E.34 and Figure E.35
2. the full-scale FPTT can be determined from the DWTT which is related to the Charpy transition temperature through the experimental data trends in Figure E.33,

then the transition temperature for a surface-cracked pipe by any combination of test data and empirical correlations can be determined. Obviously using a test specimen like the SEN(T) specimen in the L-R orientation should give the most accurate result, whereas the Charpy data is the most readily available data, and requires the use of several empirical relationships that are valid for this class of ferritic steels. Note that if only a few Charpy shear area versus temperature values are known, then a statistical temperature relationship such as that shown in Figure E.42 could be used to determine the Charpy 85 percent shear area transition temperature (TC). Also, if the Charpy specimens have a thickness less than the standard size (10 mm), then Figure E.43 can be helpful in determining the difference between the Charpy and DWTT 85 percent shear area transition temperatures.

The following section shows how the above data and trend curves can be used to assess the lowest temperature where ductile fracture is anticipated in A106 Grade B pipe with either a through-wall crack or a surface crack when only Charpy data are available. Of particular interest is to examine the trend curves from a statistical evaluation of Charpy data for A106 B pipe to see if some preliminary guidelines can be established. Afterwards, this relationship is compared to results from a number of other full-scale pipe tests available in the literature.

E.2.2.1 Charpy Input Data

The analysis methodology begins by using the Charpy impact energy data to determine the transition temperature corresponding to an 85 percent shear area. Depending upon the source of the test material used to develop the Charpy energy data, the test specimens may vary in size. Typical Class 2/3/BOP piping, for example, may be too thin to yield full-thickness test specimens. Since the transition temperature is a function of thickness, the specimen size used to develop the input data must be known.

The shear area versus temperature data from full-thickness Charpy test specimens for both the C-L and L-C orientations from the PIFRAC database (Ref. E.23) is given in Figure E.44. The L-C data were not necessarily from the same pipes as the C-L data. If so then it would be expected that the average transition temperature curves should be virtually identical. Nevertheless, the difference of the average transition temperature curves is only about 10ºC (18ºF) for these two data sets. The average Charpy full-thickness specimen 85 percent shear area transition temperature (T_c) is approximately 70ºC (158ºF) for these data, which is probably representative of most A106B pipes, but a more complete database should be established before any general rules should be applied. (Note, the results in Figure E.44 appear to be close to the 1972 results presented in Figure E.41). Additionally, one might want to use a mean plus one standard deviation T_C value instead of a mean value.

E.2.2.2 Drop-Weight Tear Test Transition Temperature

The drop-weight tear test (DWTT) is representative of full-thickness impact behavior. If experimental data exist from DWTT of the pipe material, the analysis can begin at Step 2 using these data to estimate the 85 percent shear area transition temperature (T_d). Otherwise, the DWTT transition temperature (T_d) can be calculated using the curves

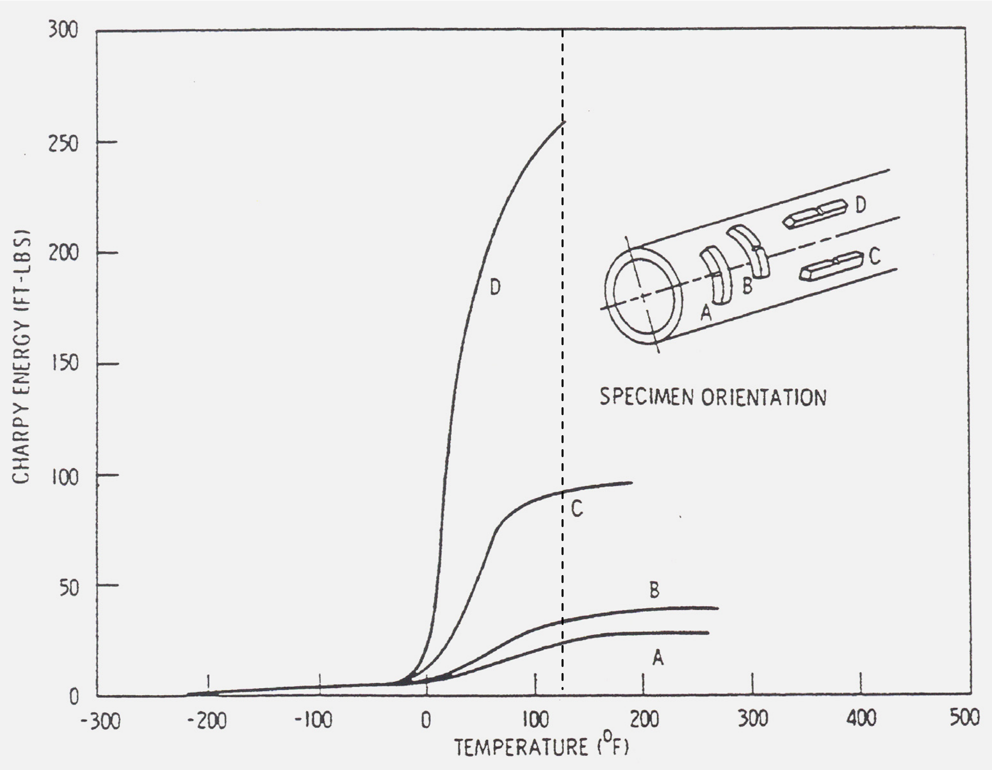

Figure E.41 Charpy energy curves for A106B – WRC Bulletin 175 (Ref. E.22) (Orientation D is for circumferential surface flaw Orientation A is for axial through-wall flaw – typically reported)

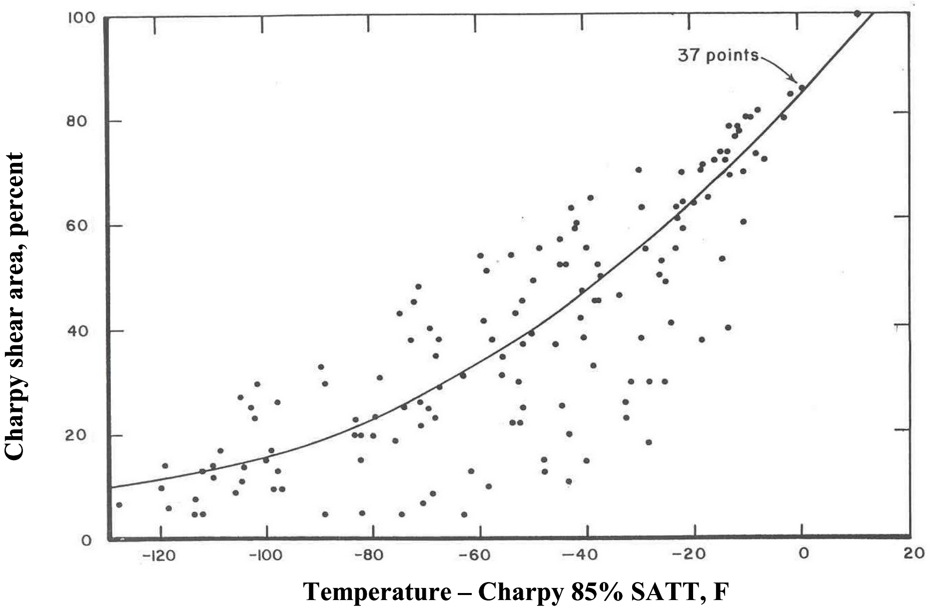

Figure E.42 Normalized fit of Charpy shear area transition curves from lower-strength linepipe steels (Ref. E.15)

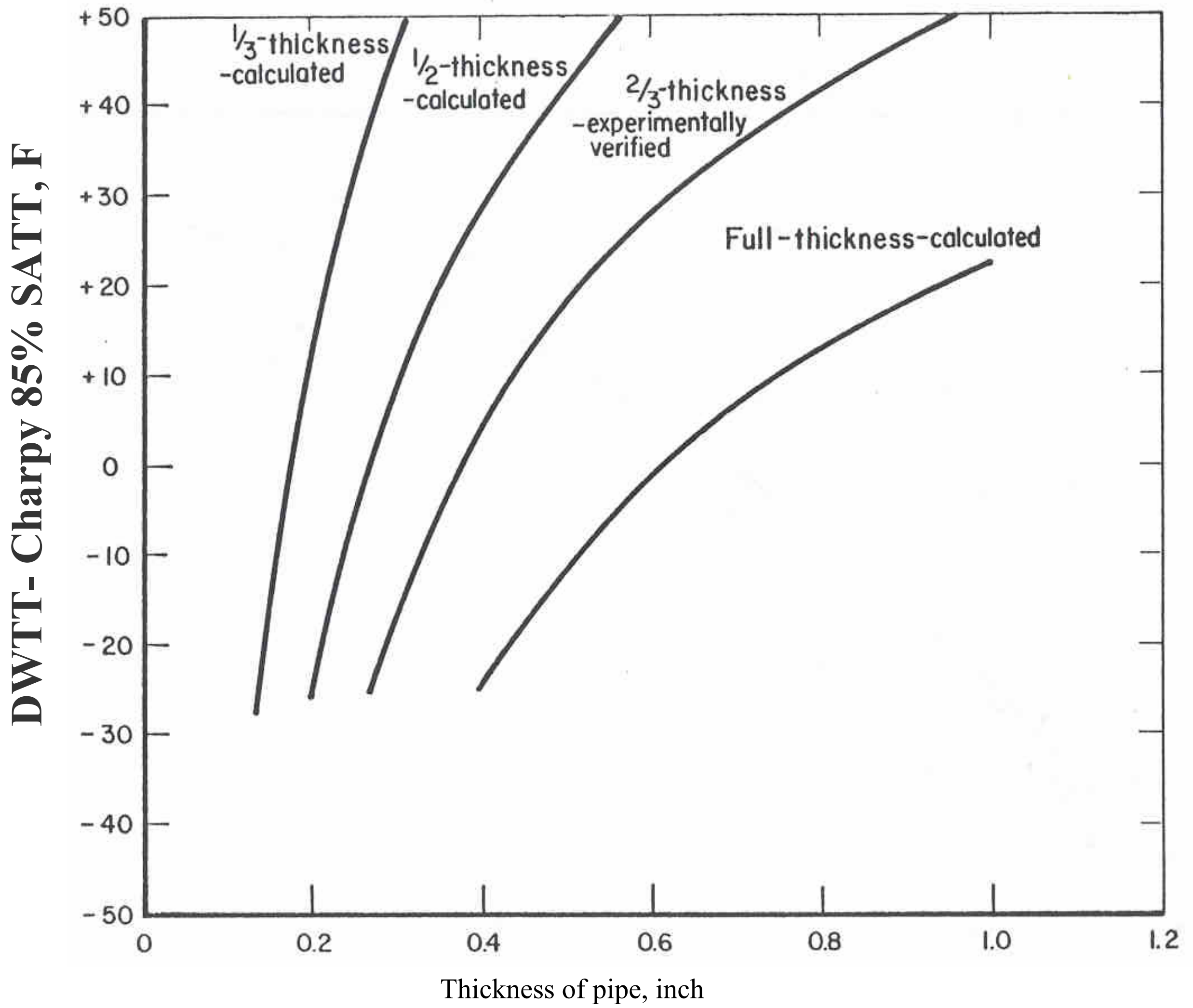

Figure E.43 Relationship between DWTT and Charpy 85% shear area transition temperatures (SATT) as function of Charpy specimen thickness (Ref. E.15)

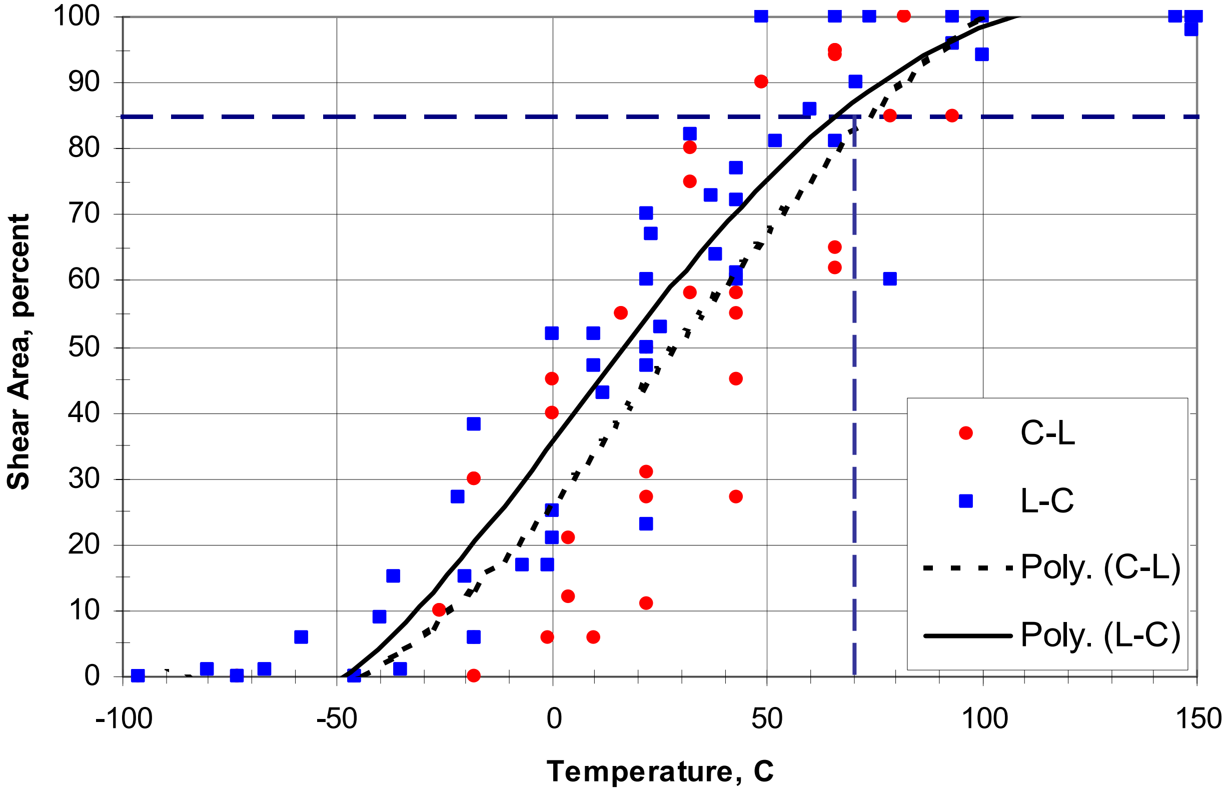

Figure E.44 Shear area versus temperature from full-thickness Charpy test data for A106B taken from PIFRAC database, Ref. E.23

in Figure E.43 which shows a transition temperature correction curve based on material thickness from DWTT results and Charpy specimen thickness which is based on experimental data for X52 and X60 linepipe steels. The lowest curve represents full-size Charpy behavior and was calculated based on the transition temperature being proportional to 1/√t and a function of the material yield strength. The thickness-temperature difference shift increases as the yield strength increases. While the curves in Figure E.43 are based on an average yield strength of 400 MPa (58 ksi), it is believed to be applicable for typical ferritic pipe in the Class 2/3/BOP applications.

The curves shown in Figure E.43 are used to estimate the shift in the transition temperature due to material thickness. For instance, a 12.7-mm (0.5-inch) thick pipe material will require an offset of approximately -10ºC (-18ºF) from the full-thickness Charpy derived transition temperature (T_c) to the DWTT transition temperature (T_d) at 85 percent shear area.

E.2.2.3 Fracture-Propagation Transition Temperature

The fracture-propagation transition temperature (FPTT) represents the temperature at which the mode of a dynamically propagating crack changes from shear to cleavage, Ref. E.16. The full-thickness transition temperature for pipeline material is typically determined by the drop-weight tear test (DWTT). As the thickness of the DWTT specimen increases, the transition temperature of the material also increases. This response is also observed in piping. Consequently, as was noted earlier, the DWTT has been shown to be a reasonable predictor of full-size pipe behavior, Ref. E.15. The shape of the curve from both DWTT and full-size pipe data is similar for shear area as a function of temperature. Therefore, the DWTT transition temperature (T_d), calculated either from Figure E.43 or directly from test data, is used to predict the fracture propagation transition temperature (FPTT).

E.2.2.4 Fracture-Initiation Transition Temperature for Through-Wall-Cracked Pipe

The fracture-initiation transition temperature (FITT) represents the temperature at which the mode of fracture initiation changes from brittle to having enough ductile crack growth so that failure pressures are the same at higher temperatures, Ref. E.17. This FITT value will be different for a through-wall crack than a surface crack due to constraint effects. For a through-wall crack, it is expected that the FITT(TWC) will be lower than the FPTT (propagating through-wall crack) because propagation is a dynamic event involving high strain rates increasing the likelihood of cleavage fracture.

As previously noted, from a series of tests conducted on full-size pipe with axial through-wall flaws, it was shown that the fracture-initiation temperature was 33ºC to 50ºC (60°F to 90ºF) below the FPTT determined from DWTT results, Ref. E.17. The variation in the FITT was attributed to differences in the flaw geometry and material properties.

In this methodology, the predicted upper-shelf FITT(TWC) for a pipe with a TWC is offset from the FPTT by approximately -33ºC to -50ºC (-60°F to -90ºF).

E.2.2.5 Fracture-Initiation Transition Temperature for Surface-Cracked Pipe

Previously it was shown that surface-cracked pipe have a lower FITT than through-wall-cracked pipe. This is because of the constraint differences in the triaxial stresses at the crack tip that induce cleavage fracture. Therefore, the methodology applies an additional offset to the predicted transition temperature in the presence of a surface crack. The t x t 3-point bend-bar flaw orientation is representative of the behavior expected from through-wall-cracked pipe, even though the failure stresses are considerably lower. The change in transition temperature measured from 3-point bend-bar tests and single-edge-notch tension SEN(T) tests are shown in Figure E.40(a).

E.2.3 Example Problem

The methodology is demonstrated in the following sections by an example.

E.2.3.1 Input Data

The example is based on the following input data:

1. Charpy data for A106B pipe steel, L-C orientation, 10-mm thick specimen (full thickness). This data is shown in Figure E.44.
2. Surface crack depth-to-thickness, $a/t = 0.25$.
3. Pipe thickness, $t = 15$ mm (0.60 inch).

E.2.3.2 Application of the Methodology

The Charpy data shown in Figure E.44 was obtained from the PIFRAC database (Ref. E.23) for A106B pipe material. The figure contains data for test specimens that were 10-mm (0.394-inch) thick (full thickness) and machined in an L-C orientation. The data was curve fit and the transition temperature corresponding to 85 percent shear area was determined to be +70°C (+158°F). This represents the full-thickness Charpy transition temperature (T_c).

The transition temperature shift from the Charpy specimen to the full-size pipe transition temperature, represented by (T_d), is determined from Figure E.43 using the lower curve. The change in temperature (T_d-T_c) equals -5.5ºC (-10°F). Thus $T_d = T_c + -5.5$ºC = +64.5°C (+148ºF). This is the fracture propagation transition temperature (FPTT) for the full-thickness pipe material.

The next step is to determine the fracture initiation transition temperature (FITT) for a through-wall-cracked pipe. Based on the experimental data previously discussed (Figures E.34 and E.35), the change in temperature to obtain the FITT(TWC) is FPTT (or Td) –33°C to –50°C (–60°F to -90ºF). Using the average, ΔT = -42°C (-75ºF), the FITT(TWC) = T_d - 42°C = +22.5°C (+73°F).

The final step is to calculate the upper-shelf fracture initiation transition temperature (FITT) for a surface-cracked pipe with a flaw depth-to-thickness ratio of a/t = 0.25. The change in temperature to obtain the FITT(SC) is based on the curve in Figure E.40a. For a/t = 0.25, ΔT = -38.9ºC (-70ºF). Therefore, FITT(SC) = FITT(TWC) -38.9ºC = -16.4ºC (+2.5ºF). Thus the predicted upper-shelf fracture initiation transition temperature for an A106B pipe with a wall thickness t = 15 mm (0.6 inch) and a/t = 0.25 equals –16.4ºC (+2.5ºF).

E.2.4 General Trends for A106B

This methodology was applied to predict the fracture initiation transition temperature for surface cracks (FITT(SC)) over a range of material thickness and crack depths using the A106B Charpy data shown in Figure E.44 in combination with Figure E.40a, Figure E.43, and the average shift of 42ºC (75ºF) from the FPTT to FITT for a through-wall crack. The results are shown in Figure E.45. Also shown in this plot are the propagation and initiation transition temperature curves for a through-wall crack. The data suggest that A106B pipe operating above 10ºC (50ºF) with a wall thickness less than 25 mm (1.0 inch) will exhibit ductile fracture initiation behavior so that the failure pressure for all surface-crack geometries of practical concern should be the same as that for warmer temperatures (not accounting for changes in strength properties with temperature). At 20ºC (68ºF), A106B pipe up to 50-mm (2-inch) is predicted to have ductile initiation for all surface-crack geometries.

E.2.5 Validation with Existing Data in Literature

There are a number of A106B and other ferritic nuclear grade pipe tests that have been conducted in the past that can be used to assess the validity of the general trend curve given in Figure E.45. These tests and their results are summarized in Table E.5. The results showed that the general trend in Figure E.45 is correct, however, the data for A106B pipe tests are not sufficient to accurately demark the predicted brittle-to-ductile transition temperatures, i.e., the tests were conducted much warmer than the minimum predicted temperature for ductile fracture.

In addition to the A106B tests, there have also been a limited number of tests on similar ferritic steels. Those test results and comparisons to the minimum predicted transition temperatures are given in Table E.6. In these cases, the actual Charpy 85 percent shear area transition temperature (or percent best estimate of that value) was used to determine the FITT for the flaw type (surface crack or through-wall crack) tested. Again, most of these results show that the analysis procedure is correct, however, the tests were generally conducted well above the minimum transition temperature so that there were no brittle fracture cases to bracket the FITT. Only in three cases were there tests that were close to the predicted FITT. These were the Kiefner X60 surface-cracked pipe tests, and the two sets of tests by Sugie on Grade B pipe. The Kiefner X60 lowest temperature test agrees with the predicted FITT(SC), but there was no brittle initiation data point to get the actual experimental FITT(SC). The Sugie tests had a lower FITT(SC) than predicted. This may be due to the experiments using a machined V-notch rather than a sharp fatigue crack, or scatter in the material behavior, where we used an average trend curve. Nevertheless, the results showed that the general procedure is at least conservative (assuming no great effect from the machine notch versus fatigue crack in the past pipe tests).

E.2.6 Limitations on the Methodology

The methodology developed to predict the fracture initiation transition temperature for a surface-cracked pipe is based on the use of empirical correlations between experimental data from standardized and non-standardized material properties tests and full-size pipe tests. Previous work has suggested that the shift in transition temperature is a function of material properties as well as pipe and crack geometry. As a result, the methodology relies on the extrapolation of standard test specimen data to predict full-scale pipe fracture behavior.

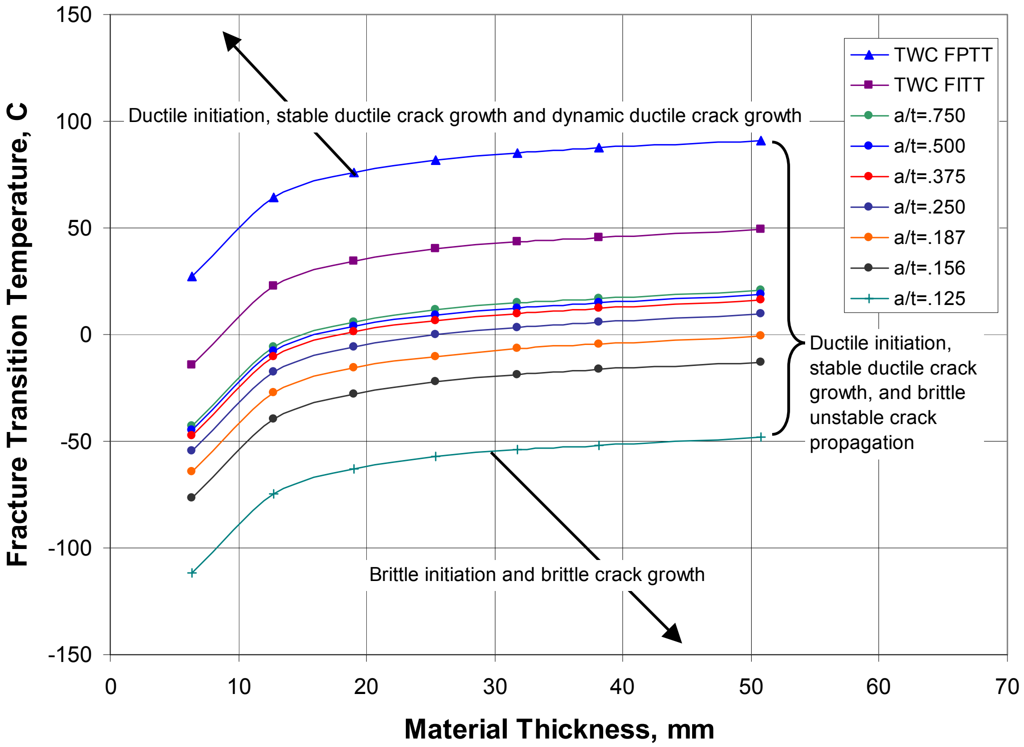

Figure E.45 Preliminary FITT relationship as a function of material thickness and crack depth (Based on upper-bound A106B data in PIFRAC database – L-C orientation)

Table E.5 Circumferentially cracked A106B pipe test results and comparison to minimum temperature for ductile fracture

Reference	Pipe thickness, mm (inch)	Flaw type	Test temperature, °C (°F)	Result	Predicted FITT, ºC (ºF)
CISE-a	5.5 (0.217)	TWC	20 (68)	Ductile initiation, brittle propagation	-17.9 (0)
CISE-b	10.9 (0.429)	TWC	20 (68)	Ductile	4.4 (40)
CISE-c	17.1(0.673)	TWC	20 (68)	Ductile	12.8 (55)
CISE-d	18.8 (0.740)	TWC	20 (68)	Ductile	15.5 (60)
GEAP	11.0 (0.432)	TWC	20 (68)	Ductile initiation, brittle propagation	4.4 (40)
DTRC	14.0 (0.55)	TWC	51.7 (125)	Ductile	7.2 (45)

Table E.6 Circumferentially cracked ferritic pipe test results and comparison to minimum temperature for ductile fracture

Ref.	Material	Full-size Charpy 85% SATT transition temperature °C (°F)	Thickness, mm (inch)	Flaw type	Test temperature °C (°F)	Result	Predicted FITT with adjustment for actual Charpy data ºC (ºF)
NUPEC-a	STS 42	<20 (<70)	9.14 (0.36)	TWC	20 (68)	Ductile	-35 (-31)
NUPEC-b	STS 42	<20 (<70)	8.79 (0.346)	SC a/t=0.5	20 (68)	Ductile	-65 (-85)
NUPEC-c	STS 42	<20 (<7)	19.00 (0.748)	SC a/t=0.5	20 (68)	Ductile	-45.5 (-50)
Kiefner(i)	API X60	20 (70)	9.14 (0.360)	SC a/t=0.5	-62 (-80)	Ductile	-65.6 (-86)
MPA	German ferritic pipe	0ºC (32)(ii)	8.00 (0.315)	SC a/t=0.5	20 (68)	Ductile	-87.2 (-125)
JAERI-a	STS42	<20 (<70)(iii)	10.6 (0.429)	TWC	20 (68)	Ductile	-29.4 (-21)
JAERI-b	STS42	<20 (<70)(iv)	10.6 (0.419)	SC a/t=0.5	20 (68)	Ductile	-51.7 (-61)
DP^{3}II	API X65	-40 (-40)	15.9 (0.625)	TWC	-7 (20)	Ductile	-146 (-230)
Short Crack	A53-weld	-80 (-112)(iv)	6.02 (0.237)	SC a/t=0.6	20 (68)	Ductile	-181 (-293)
Sugie-HT	Grade B	-15 (5)(v)	9.5 (0.375)	SC a/t=0.5	-135 (-211)	SC FITT	-99 (-146)
Sugie-SR	Grade B	-20 (-4)(v)	9.5 (0.375)	SC a/t=0.5	-196 (-320)	Ductile	-104 (-155)

(i) Results in Figure E.37. Charpy calculated from DWTT. Transition temperature 27.8°C (50°F) lower than A106B for this steel.

(ii) ¾ thickness Charpy specimens – transition temperature 41.6°C (75°F) lower than A106B for this steel (accounting for Charpy specimen size). Unpublished data form Dr. Karl-Heinz Herter.

(iii) Using the NUPEC STS42 data.

(iv) ¼-thickness specimen in weld metal.

(v) Original data from 2/3-thickness Charpy tests. Correction to full-thickness specimen made. Accounted for actual material Charpy transition temperature for predicted surface-crack FITT.

The Charpy impact data, like that shown in Figure E.44, is based on a standardized test method; however, the thickness of the test specimens is dependent on the source material. As a result, sub-sized specimens are frequently required to characterize thin-walled pipe. The reasonable bounds on the Charpy 85 percent shear area transition temperature for typical nuclear ferritic pipe base metals and weld metals should be explored further before a general trend can be used for those grades of steel.
Figure E.46 shows Charpy data from PIFRAC for A516 Grade 70 base metal and welds, and Figure E.47 shows Charpy data for A106B welds (also from PIFRAC). It is encouraging that the welds had a lower 85 percent transition temperature than the base metals, and the limiting case was the A106B base metal (Figure E.44).

The offset used to shift the transition temperature from propagation (FPTT) to initiation (FITT) for a through-wall crack was based on only two full-scale pipe experiments on X-52 material. The similitude between the FITT for the through-wall crack and bend-bar or C(T) specimens was also verified by only one set of pipe tests on line-pipe steel. These are steps in the analysis that could use further validation.

Likewise, the transition temperature shift from the TWC to the surface-crack pipe behavior as a function of crack depth was based on results from non-standard laboratory tests of X-42 and X-60 steel that are believed to be representative of the constraint in surface-cracked pipe. Further validation of this assumption is needed.

To validate the general Option 3 procedure, and several of the assumptions used, a series of specimen and surface-cracked pipe tests were conducted in this program and will be discussed next. These tests involved:

- Charpy tests (L-C orientation) at various temperatures on that same material,
- Modified DWTT specimens (L-C orientation) at various temperatures (full-thickness of pipe but with shorter ligaments due to pipe curvature – the dynamic tear test (DTT) was used instead of the DWTT – ASTM Standard E604),
- C(T) specimens (L-C orientation) at various temperatures,
- SEN(T) tests (L-R orientation) at various temperatures, and
- 6-inch diameter Schedule 120 A106 B pipe with circumferential surface cracks (fatigue sharpened) in the base metal at various temperatures.

This preliminary investigation of the general trend curve for determining the FITT for a surface crack from A106B Charpy data is encouraging since most the Class 2/3/BOP piping would be less than 25-mm (1.0-inch) thick and have a minimum operating temperature above 10ºC (50ºF). Furthermore, the A106B base metal appears to be a limiting case when compared to existing data for A516 Grade 70 base metal and weld metal data for these two pipe materials. Nevertheless, before these results are used, a larger database of ferritic nuclear pipe Charpy data and weld metal data are needed, as well as a statistical evaluation (rather than using average trend curves), and validation of all the steps in the procedure is needed. Preliminary validation tests were conducted in the BINP program as discussed next. Nevertheless, it is encouraging that the upper-shelf EPFM analyses in the ASME Appendix H can probably be used for most practical Class 2/3/BOP piping ferritic base metals.

E.2.7 Validation of Methodology

In order to validate this methodology for predicting the FITT of a surface-cracked pipe from the 85-percent shear area transition temperature from Charpy specimen tests, a series of Charpy, dynamic tear test (DTT), compact (tension), single-edge-notch [tension] (SEN(T)), and full-scale surface-cracked pipe experiments were conducted. The test specimens used in all of these tests came from two lengths of 6-inch nominal diameter, Schedule 120, A106 Grade B pipe that came from the same heat. The Battelle pipe identification numbers for these two lengths of pipe were DP2-F93 and F94.

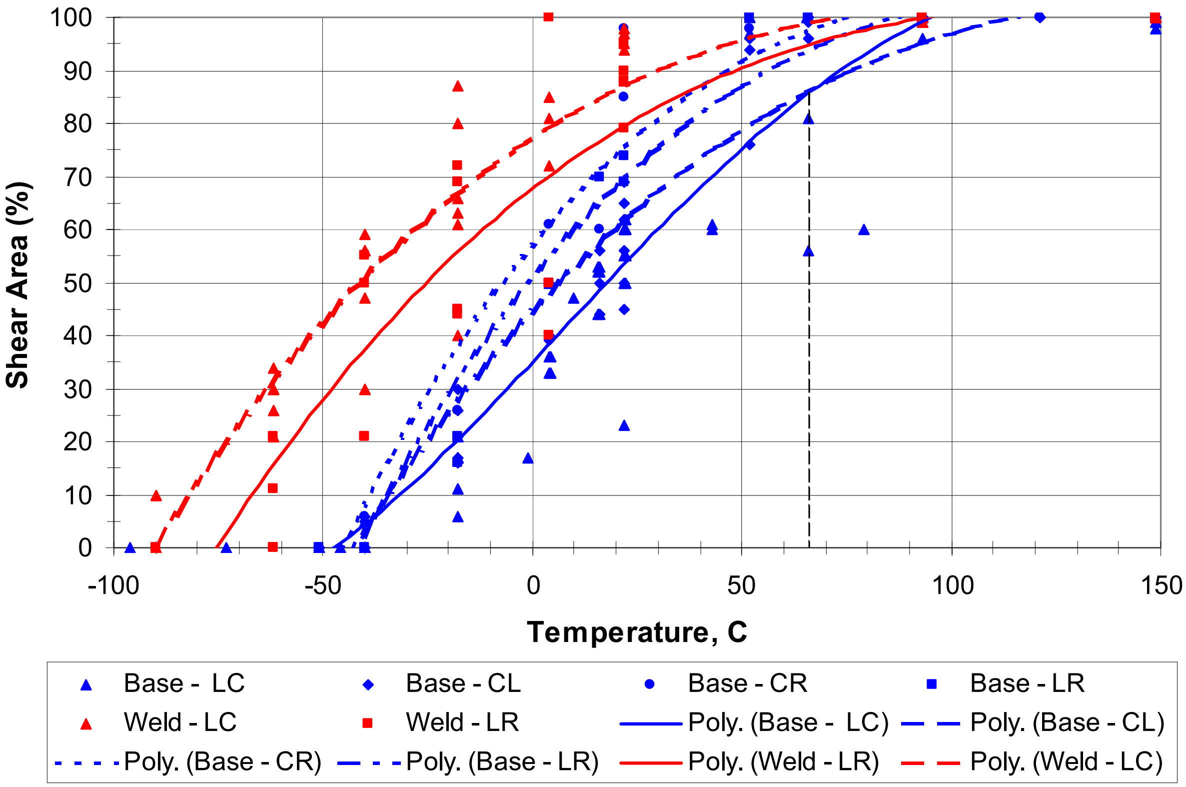

Figure E.46 Charpy data from PIFRAC for A516 Grade 70 pipe and welds

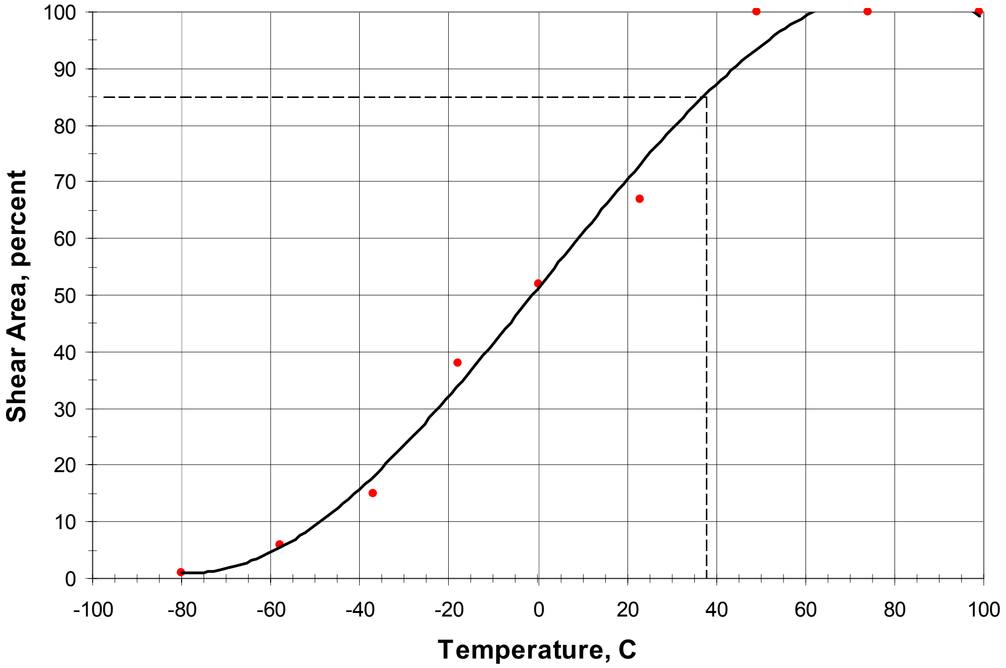

Figure E.47 Charpy data from PIFRAC for one A106B pipe weld

Figure E.48 is a plot of the shear area percent from a series of Charpy specimen tests as a function of the test temperature for both lengths of pipe, i.e., DP2-F93 and F94. From Figure E.48 one can see that the 85-percent shear area transition temperature for both lengths of pipe was approximately 58 C (136 F).

The next series of tests conducted were the dynamic tear tests (DTT). The test specimens for these tests were machined from the pipe without flattening. As such, the maximum wall thickness achievable was approximately 10 mm (0.4 inches). Based on Figure E.43, the FPTT 85-percent shear area transition temperature for this specimen geometry for this specimen thickness for this material should have been approximately 44 C (111 F). Figure E.49 is a plot of the shear area as a function of the test temperature for these DTT. As can be seen in Figure E.49, the actual measured 85-percent shear area transition temperature of 54 C (130 F) was approximately 10 C (19 F) warmer than anticipated.

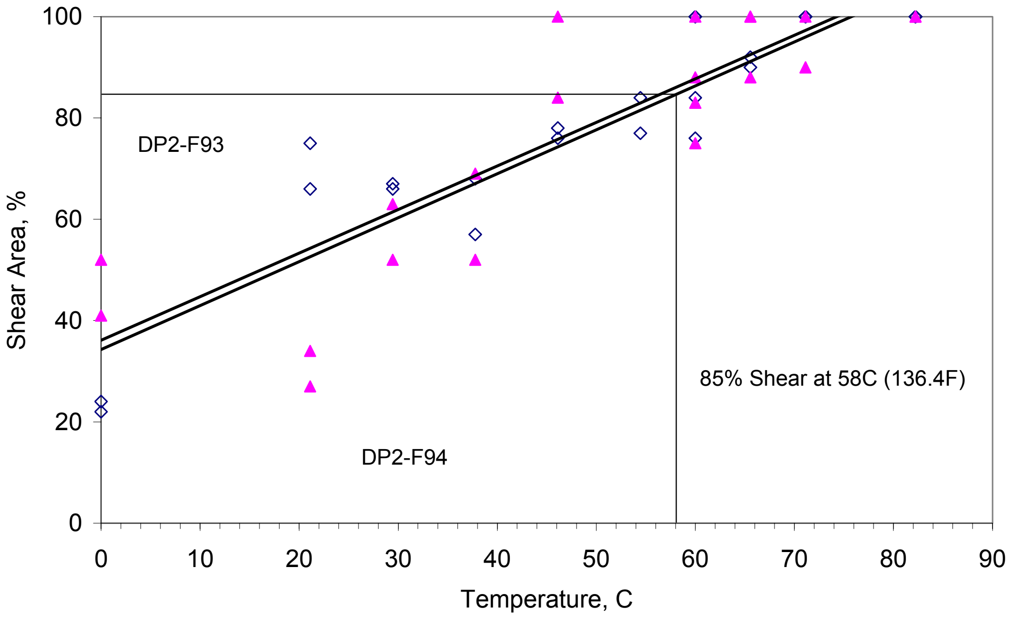

Figure E.48 Shear area as a function of test temperature for the Charpy specimen tests for material DP2-F93 and F94

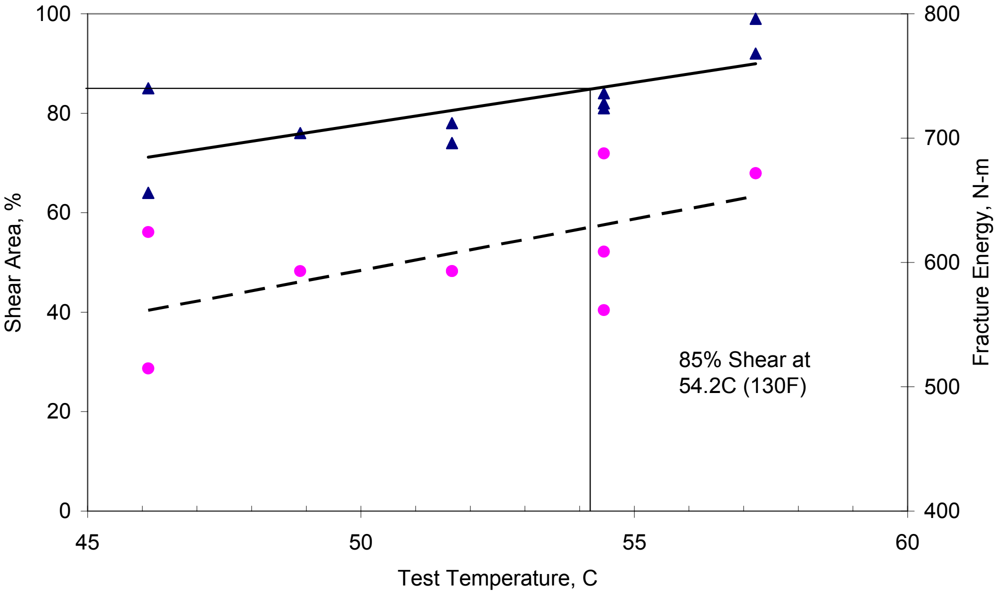

Figure E.49 Shear area as a function of test temperature for the DTT specimen tests for material DP2-F93 and F94

The next series of tests conducted were the compact (tension) specimen tests. It was anticipated that the transition temperature for these tests would provide an indication of the transition temperature for a through-wall cracked pipe. Based on Figures E.34 and E.35 it was anticipated that there would be a shift in the transition temperature of approximately 33 to 50 C (60 to 90 F) between the DTT specimen results and these compact (tension) specimen results. Based on the anticipated shift in transition temperature between the compact (tension) and the actual Charpy data, accounting for the anticipated shift between the DTT and the actual Charpy data, the transition temperature for these compact (tension) specimen tests was anticipated to be between 11 C (51 F) and -6 C (21 F). Figure E.50 is a plot of the load versus displacement records for eight compact (tension) specimen tests conducted as part of this effort. As can be seen from Figure E.50, even at a test temperature of -32 C (-26 F), there still was some evidence of ductile crack initiation for these compact (tension) specimen tests.

The last series of laboratory specimen tests was the SEN(T) specimen tests. Due to the similitude in the constraint conditions between the SEN(T) specimen geometry and the surface-cracked pipe geometry, it was thought that this specimen geometry would provide the most direct indication of the transition temperature

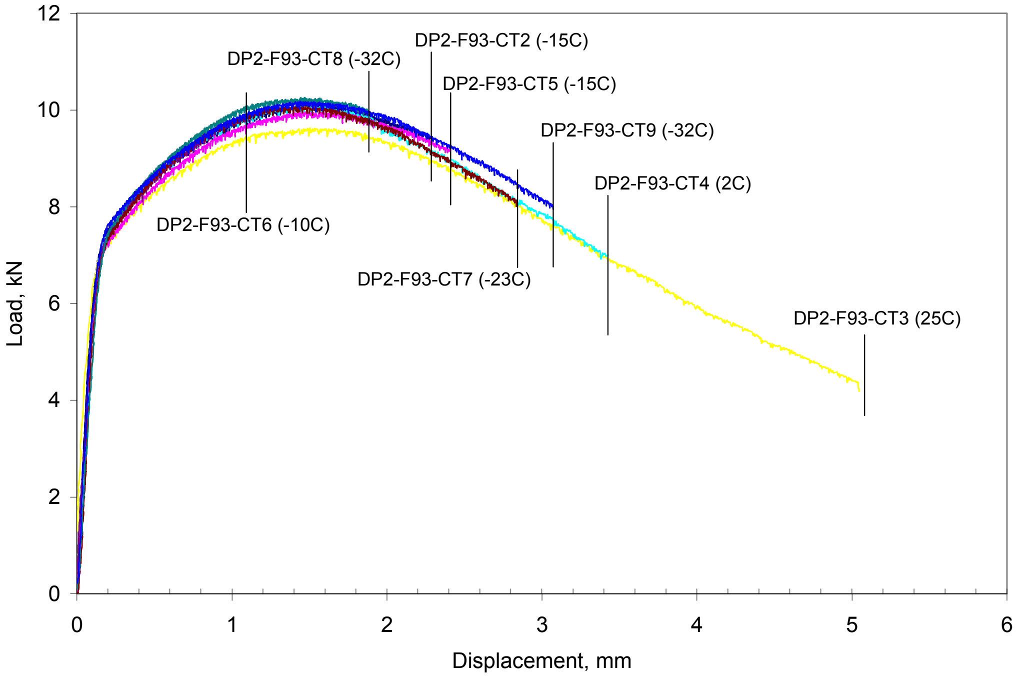

Figure E.50 Load versus displacement records for compact (tension) tests

for the actual surface-cracked pipe. For a surface crack which is 50 percent of the pipe wall thickness in depth, which is the crack depth used in both the SEN(T) and surface-cracked pipe tests, one would expect a 33 C (60 F) shift in transition temperature between the 3-point bend bar specimen geometry and the surface-cracked pipe geometry, see Figure E.40a. Since the 3-point bend bar specimen geometry is thought to provide similar constraint as a compact (tension) specimen and a through-wall-cracked pipe, one would expect a similar shift in transition temperature between those specimen geometries and a surface-cracked pipe. Thus, on the basis of the measured Charpy data alone and the analysis method developed as part of this effort, one might expect that the transition temperature for a surface-cracked pipe, or SEN(T) specimen, may be in the range of -23 C (-9 F) to -39 C (-39 F). Figure E.51 is a plot of the load versus actuator displacement data for these SEN(T) specimen tests. Each test appeared to initiate in a ductile manner followed by unstable brittle fracture. Figure E.52 is a plot of the ductile crack growth as a function of test temperature. As can be seen in Figure E.52, with the exception of one specimen, the data is fairly well grouped showing a general trend of decreasing ductile crack growth with decreasing test temperature. Based on the trends in Figure E.52 one might argue that one might reach the point of brittle fracture initiation for these SEN(T) specimens in the range of -50 to -60 C (-58 F to -76 F), which is approximately 25 C (45 F) colder than what one might have expected based on the measured Charpy specimen transition temperature and the methodology developed as part of this effort.

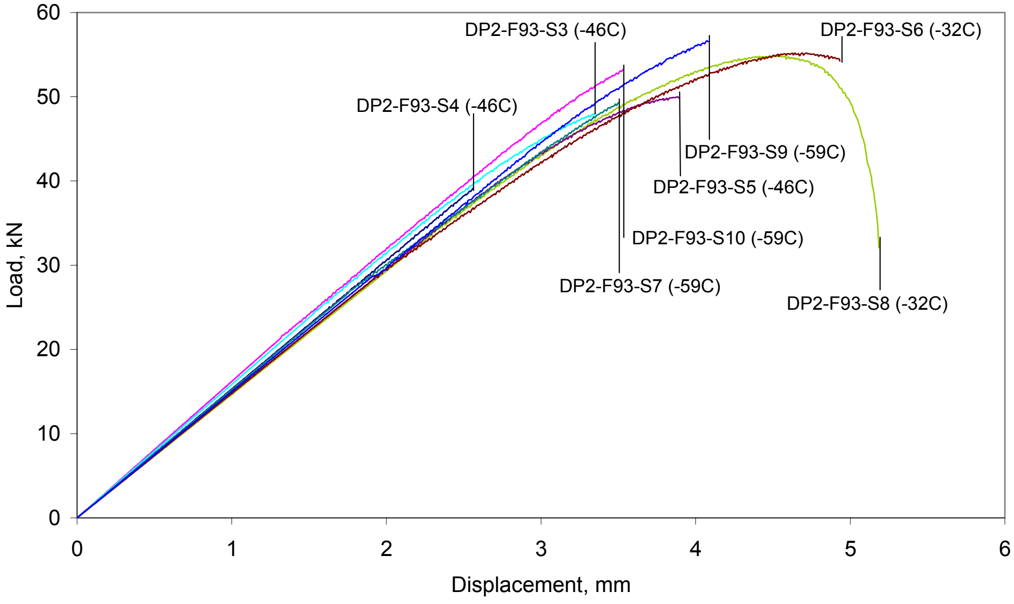

Figure E.51 Load versus actuator displacement data for the SEN(T) specimens

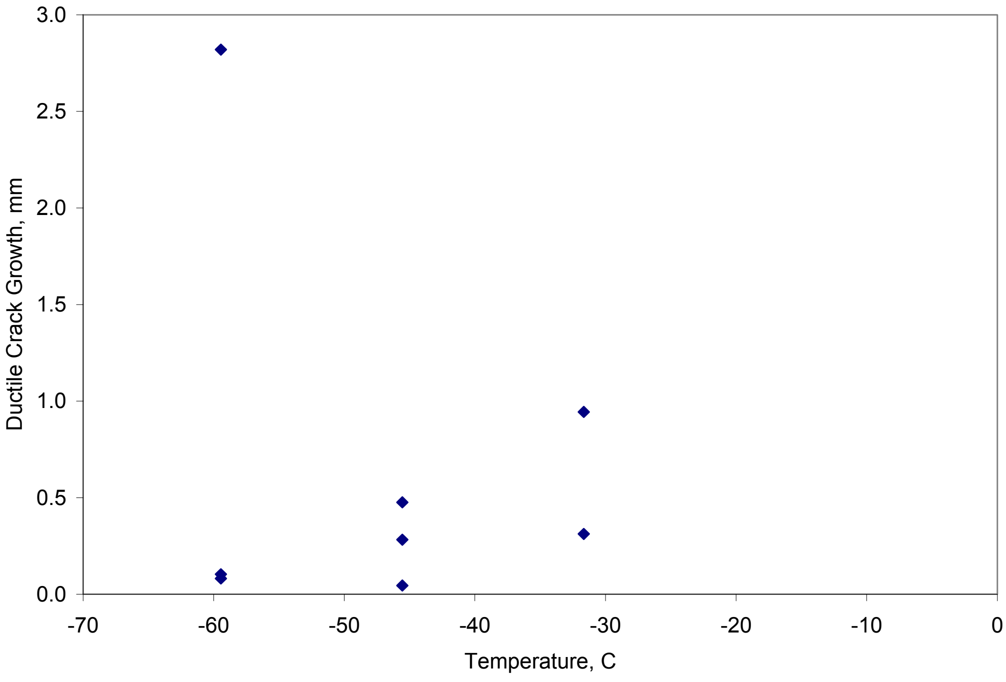

Figure E.52 Ductile crack growth as a function of temperature for the SEN(T) specimens

As a final measure of the validity of this methodology, three surface-cracked pipe experiments were conducted using this pipe material. In each case the crack was an external surface crack, approximately one-third around the pipe circumference in length and half way through the wall thickness in depth, see Figure E.53.

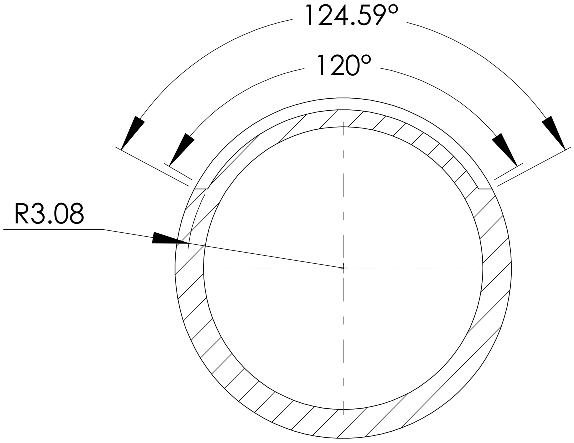

Figure E.53 Crack geometry for the surface-cracked pipe experiments

Figures E.54 and E.55 show schematics of the loading fixtures and cooling apparatus, respectively, for these three pipe experiments. The pipes were cooled by circulating Syltherm XLT, a Dow Chemicals Heat Transfer Fluid, through the pipe using a circulation pump. Copper tubes containing the fluid were coiled and submersed in a cooling bath of this same fluid with dry ice pellets added to cool the fluid.

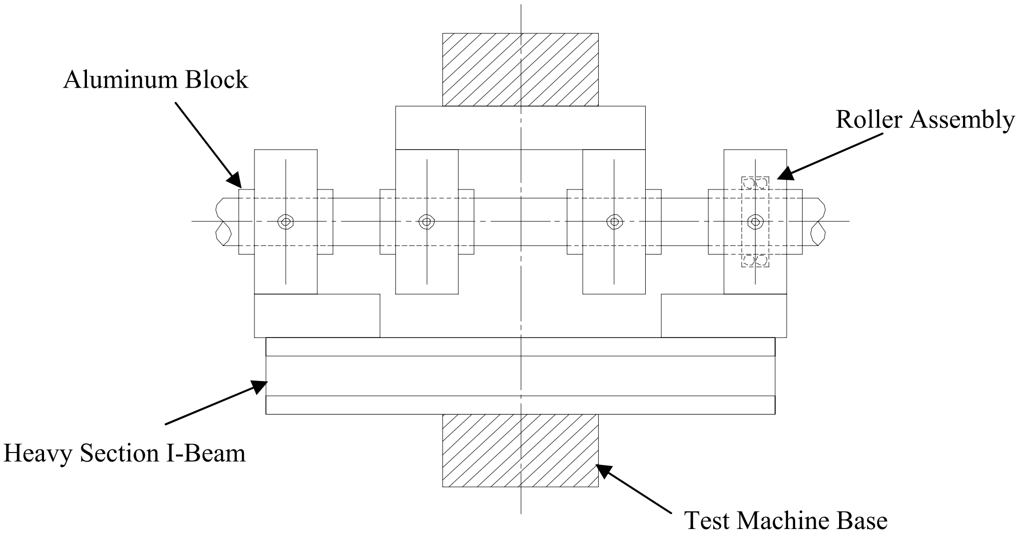

Figure E.54 Loading fixture used in the surface-cracked pipe experiments

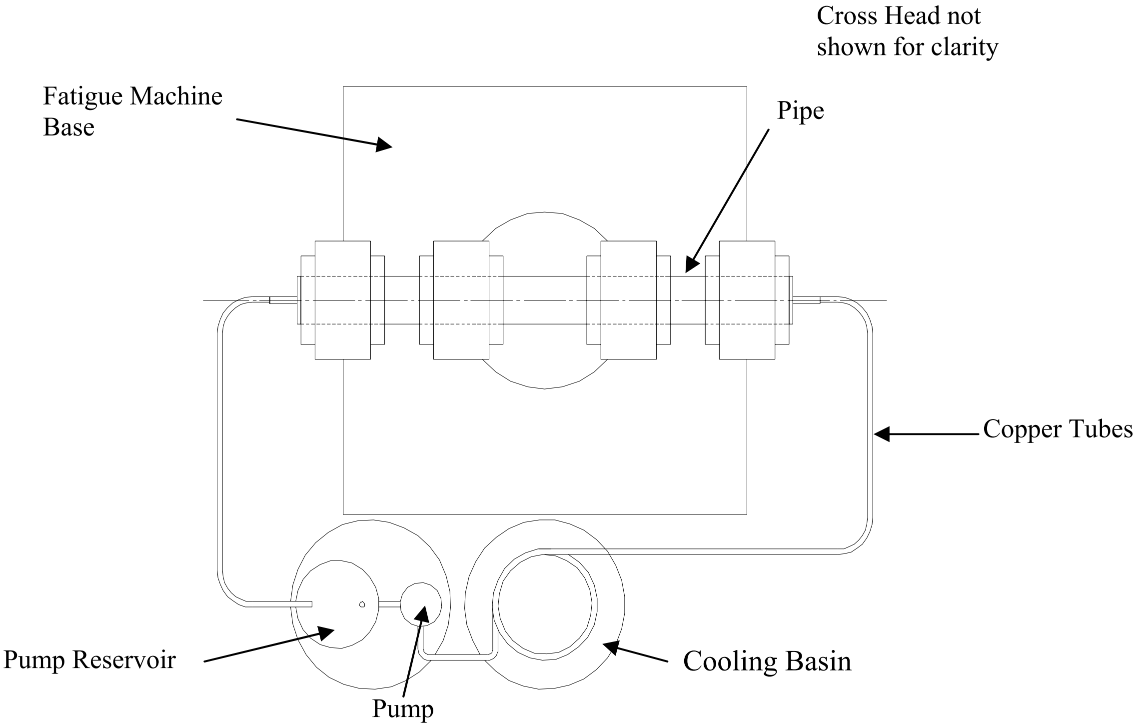

Figure E.55 Cooling apparatus used in the surface-cracked pipe experiments

Figure E.56 is plot of the load versus displacement records for the three surface-cracked pipe experiments. As can be seen, the test temperatures for these three experiments were -59 C (-75 F), -46 C (-50 F), and -32 C (-25 F). Both the load and displacement decreased as the test temperature decreased. The amount of ductile crack growth, prior to the final brittle fracture, was minimal for each of these experiments. In order to make an assessment of the transition temperature for these three surface-cracked pipe experiments, the maximum moment normalized by the calculated Net-Section-Collapse (NSC) moment was plotted against the test temperature, see Figure E.57. As can be seen in this figure the relationship between the ratio of M_{max}/M_{NSC} and the test temperature is very linear. The point on the graph where the straight line fit through the data reached a value where this ratio was equal to 1.0 was called the transition temperature. Based on this assessment, the transition temperature for these surface-cracked pipe experiments was -36 C (-33 F). This estimate of the actual surface-cracked pipe transition temperature is within the range of what one might expect the transition temperature to be based on the actual Charpy data and the analysis method developed as part of this effort, i.e., -23 C (-9 F) to -39 C (-39 F). Thus, even though some of the individual steps in the methodology (e.g., the shifts between the Charpy to the DTT transition temperatures and the DTT to the compact (tension) specimen transition temperatures) appeared to overpredict the transition temperature shift, the bottom line assessment of the transition temperature for a surface cracked pipe using only the measured Charpy 85-percent shear area transition temperature appears reasonable. In summary, Table E.7 provides a synopsis of the methodology and how the experimental data agreed with the anticipated transition temperatures for each specimen geometry.

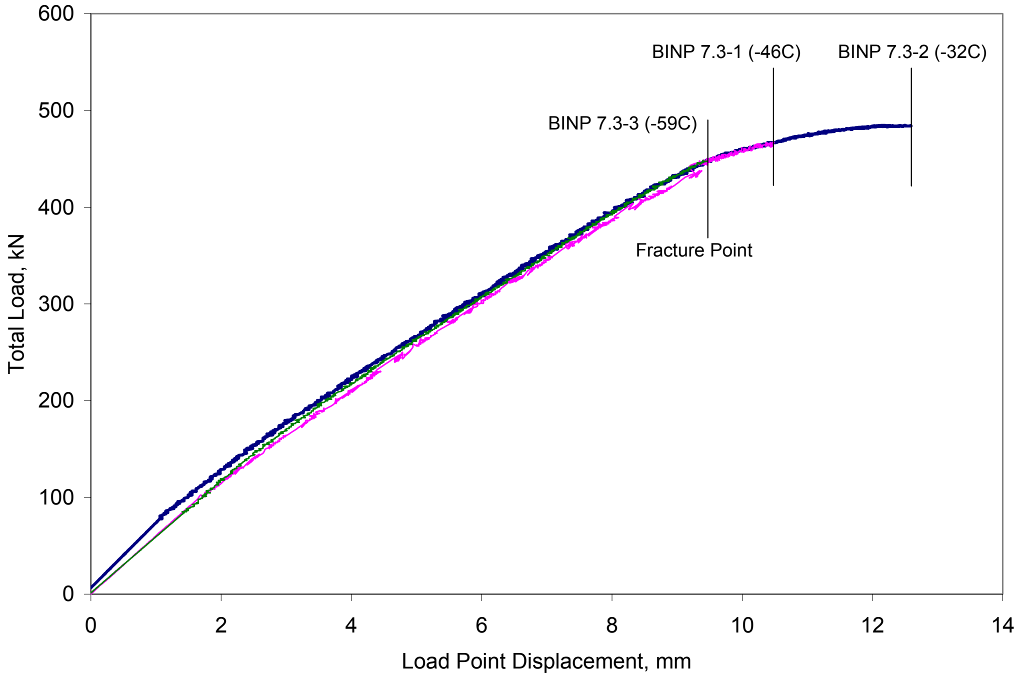

Figure E.56 Load versus displacement records for the three surface-cracked pipe experiments

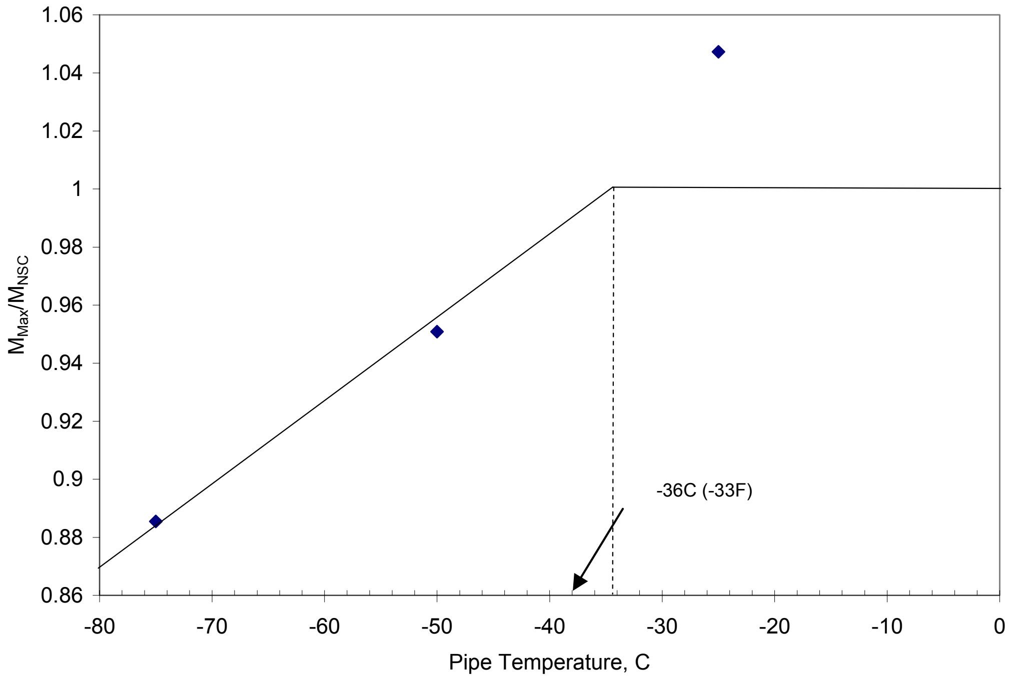

Figure E.57 Plot of the ratio of the maximum experiment moment normalized by the Net-Section-Collapse moment (M_{max}/M_{NSC}) as a function of the test temperatures for the three surface-cracked pipe experiments

Table E.7 Summary of the methodology and how the experimental data agreed with the anticipated transition temperatures for each specimen geometry

Specimen Geometry	Anticipated Transition Temperature, C (F)	Basis for Estimate of Transition Temperature	Actual Transition Temperature, C (F)
Charpy specimens			58 (136)
Dynamic Tear Tests	44 (111)	14 C (25 F) shift in transition temperature for 10 mm (0.4 inch) thick specimen	54 (130)
Compact (tension)	11 (51) to -6 (21)	33 to 50 C (60 to 90 F) shift in transition temperature between drop-weight-tear test results and 3-point bend specimen results	< -32 (-26)
SEN(T)	-23 to -39 (-9 to -39)	33 C (60 F) shift in transition temperature between 3-point bend specimen and 50% deep surface crack	-50 to -60 (-58 to -76)
Surface cracked pipe	-23 to -39 (-9 to -39)	33 C (60 F) shift in transition temperature between 3-point bend specimen and 50% deep surface crack	-36 (-33)

E.3 References

E.1 Anderson, T. L., "Stress Intensity Solutions for Surface Cracks and Buried Cracks in Cylinders, Spheres, and Flat Plates," prepared for The Materials Properties Council, Inc., March 2000.

E.2 Chapuliot, S., and Lacire, M. H., "Stress Intensity Factors for External Circumferential Cracks in Tubes Over a Wide Range of Radius Over Thickness Ratios," PVP Vol. 388, 1999.

E.3 "*NRCPIPES" Windows Version 3.0 – User's Guide*, April 30, 1996, Battelle document to 2nd IPIRG group, Contract NRC-04-91-063.

E.4 Scott, P. M., and Ahmad, J., "Experimental and Analytical Assessment of Circumferentially Surface-Cracked Pipes Under Bending," NUREG/CR-4872, April 1987.

E.5 Krishnaswamy, P., Scott, P., Mohan, R., Francini, S., Choi., Y. H., Brust, F., Kilinski, T., Ghadiali, N., Marschall, C., and Wilkowski, G., "Fracture Behavior of Circumferentially Short-Surface Cracked Pipe," NUREG/CR-6298, November 1995.

E.6 Brust, F. W., "Approximate Methods for Fracture Analyses of Through-Wall Cracked Pipes," NUREG/CR-4853, February 1987.

E.7 Brust, F., Scott, P., Rahman, S., Ghadiali, N., Kilinski, T., Francini, R., Marschall, C., Miura, N., Krishnaswamy, P., and Wilkowski, G., "Assessment of Short Through-Wall Circumferential Cracks in Pipes – Experiments and Analyses," NUREG/CR-6235, April 1995.

E.8 Kurihara, R., and others, "Estimation of the Ductile Unstable Fracture of Pipe with a Circumferential Surface Crack Subjected to Bending," *Nuclear Engineering and Design*, Vol. 106, pp. 265-273, 1988.

E.9 Mohan, R., Wilkowski, G., Bass, B., and Bloom, J., "Finite Element Analyses to Determine the R/t Limits for ASME Code Case N-494 FAD Curve Procedure," PVP Volume 350, pp. 77-88, July 1997.

E.10 Wilkowski, G. M., and others, "Degraded Piping Program – Phase II," Summary of Technical Results and Their Significance to Leak-Before-Break and In-Service Flaw Acceptance Criteria, March 1984 – January 1989, NUREG/CR-4082, Vol. 8, 1989.

E.11 Kanninen, M. F., and others, "Mechanical Fracture Predictions for Sensitized Stainless Steel Piping with Circumferential Cracks," EPRI Report NP-192, September 1976.

E.12 ASME Boiler and Pressure Vessel Code, Section XI, Rules for Inservice Inspection of Nuclear Power Plant Components, 1955 Edition, July 1995.

E.13 DWTT test procedures are given in both American Society of Testing and Materials (ASTM) Standard E436 and American Petroleum Institute (API) Recommended Practice 5L3.

E.14 DWT-NDT test procedures, ASTM E-208.

E.15 Maxey, W.A., Kiefner, J.F., and Eiber, R.J., "Brittle Fracture Arrest in Gas Pipelines", Report to Pipeline Research Committee of American Gas Association, July 1975.

E.16 Eiber, R.J., "Fracture Propagation", Symposium in Line Pipe Research, Pipeline Research Committee of American Gas Association, Section I, Dallas, Texas, November 1969.

E.17 Kiefner, J.F., "Fracture Initiation", Symposium in Line Pipe Research, Pipeline Research Committee of American Gas Association, Section G, Dallas, Texas, November 1969.

E.18 Podlasek, R. J., and others, "Predicting the Fracture Initiation Transition Temperature in High Toughness, Low Transition Temperature Line Pipe With the COD Test," ASME Journal of Engineering Materials and Technology, pp. 330-334, October 1974.

E.19 Sugie, E., Kudo, J., Kataoka, Y., Ohtani, T., "Influence of Thermal Stress Relieving on

Fracture Toughness of UOE Pipe", UTR-79019, Kawasaki Steel Corporation, Chiba, Japan, January 1979.

E.20 Wilkowski, G.M., Barnes, C.R., Scott, P.M., Ahmad, J., "Development of Analyses to Predict the Interaction of Fracture Toughness and Constraint Effects for Surface Cracked Pipe", Report to Welding Supervisory Committee of American Gas Association, April 1985.

E.21 Wilkowski, G. M., and others, "Degraded Piping Program - Phase II," Summary of Technical Results and Their Significance to Leak-Before-Break and In-Service Flaw Acceptance Criteria, March 1984 - January 1989, NUREG/CR-4082, Vol. 8, March 1989.

E.22 "PVRC Recommendations on Toughness Requirements for Ferritic Steels," WRC Bulletin 175, August 1972.

E.23 Ghadiali, N., and Wilkowski, G. M., "Fracture Mechanics Database for Nuclear Piping Materials (PIFRAC)," in Fatigue and Fracture - 1996 - Volume 2, PVP-Vol. 324, July 1996, pp 77-84. (Also on Pipe Fracture Encyclopedia CD-ROM set given to IPIRG-2 members.)